



Université
de Toulouse

THÈSE

En vue de l'obtention du

DOCTORAT DE L'UNIVERSITÉ DE TOULOUSE

Délivré par l'Universités Toulouse III Paul Sabatier

Cotutelle internationale avec :
Université des Sciences de Hanoi

Présentée et soutenue par :

Nguyet Minh NGUYEN

Le 21 Mai 2013

Titre :

Caractéristiques des marées dans le Golfe du Tonkin

Jury

Mme. Isabelle DADOU	Professeur des Universités	Université de Toulouse III
M. Bruno BLANKE	Directeur de recherche CNRS	Université de Brest
M. Kim Dan NGUYEN	Professeur des Universités	Université Paris Est
M. Thong NGUYEN	Professeur	Université Polytechnique de HCM
M. Van Uu DINH	Professeur des Universités	Université des Sciences de Hanoi
M. Patrick MARCHESIELLO	Directeur de recherche IRD	Université de Toulouse III

Ecole doctorale et discipline ou spécialité :

ED SDU2E: Océan, Atmosphère et Surfaces Continentales

Unité de recherche :

Laboratoire d'Etudes en Géophysique et Océanographie Spatiales, Toulouse, France

Directeur(s) de Thèse :

Patrick MARCHESIELLO, Sylvain OUIILLON, Van Uu DINH

Rapporteur(s):

Bruno BLANKE, Kim Dan NGUYEN, Thong NGUYEN

A word of thanks

First and foremost, I would like to sincerely thank my supervisors, Patrick Marchesiello, Sylvain Ouillon and Đinh Văn Ưu for their guidance and generous supports throughout this study. I specially thank to Patrick, who has dedicated his time and put a lot of effort toward this research. Every time we discussed, I was energized and refreshed by his astute wisdom and kind encouragement. Sylvain, you are scientist with strong social skills. Thank you for listening and your patience. Your warm smile and willingness to explain and help are so nice and valuable. The few words I can say here cannot reflect what this means to me.

Thank Gildas for supporting my Ubuntu, ROMS, etc. installation.

To Florent Lyard, I am grateful for the discussion and interpretation of some results presented in this thesis. Thank you for showing me the tools to deal with complex problems.

I would also like to thank Bruno Blanke and Kim-Dan Nguyen. Thank you for sharing passion for science. Their comments and questions were very beneficial in my completion of the manuscripts.

I have to thank my parents Nguyễn Quang Khải and Nguyễn Thuý Vân for their unconditional love and support throughout my life. I am extremely fortunate to have my husband, Nguyễn Sỹ Trung, who has given me strength to chase my dream. Thank you for spending countless hours listening to me babbling on my research with very limited understanding of it over the phone.

I would like to thank chị Yến Quách, chị Linh, chị Khoai Dím, chị Nguyễn Vĩnh Xuân Tiên, ... for your encouragement in many moments of "crisis". Your friendship makes my life a wonderful experience.

One of the benefits of having three workplaces is having a lot of nice colleagues. I really enjoyed my time working at laboratory d'Etudes en Géophysique et Océanographie Spatiales (LEGOS), in the department of Hydrology-Meteorology-Oceanography of Hanoi University of Sciences (HMO-HUS), in the department of Water-Environment-Oceanography at the University of Science and Technology of Hanoi (WEO-USTH). Thank you for creating a so warm atmosphere. Thank you all very much.

I'd like to thank the secretaries at LEGOS - Brigitte, Martine, Nadine for always helping me out all administrative things.

To my lunchtime team at LEGOS - Angela, Jérémie, Jean-Louis, Guillaume, Maria, Vincent, Léandre, Mélanie, Vanessa, Hindu, Rajesh, Kobi, Nicola..., thank you for sharing of the wonderful and the difficult moments of daily (PhD) life, and most importantly, having good laughs together. For me it is a pleasure to be surrounded by such bright minds with warm hearts.

Thank you all, I could not list all the names here, but you are always in my memory.

This thesis is a beginning of my journey...

Nguyễn Nguyệt Minh.

Toulouse June 6th 2013

Table of contents

Introduction	3
Chapter 1: Description of the Gulf of Tonkin.....	6
1.1 Geography	6
1.2 Tidal forcing.....	7
1.3 Meteorological conditions	11
1.3.1 Winds.....	11
1.3.2 Precipitation.....	12
1.3.3 Surface heat flux.....	12
1.4 Ocean Climatology	14
1.4.1 Sea Surface Temperature patterns.....	14
1.4.2 Subtidal circulation.....	15
Chapter 2: Methods	16
2.1 Description of the Regional Ocean Modeling System (ROMS).....	16
2.1.1 Equations of continuity and momentum balance	17
2.1.2 Vertical boundary conditions.....	18
2.1.3 Terrain-following coordinate systems	19
2.1.4 Horizontal curvilinear coordinates	22
2.1.5 Open boundary conditions.....	24
2.1.6 Time-stepping.....	24
2.1.7 Sigma-coordinate errors: The pressure gradient and diffusion terms ...	25
2.1.8 Turbulent closure	26
2.1.9 Nesting	26
2.2 Lagrangian modeling: Ariane	27
2.3 Data for model verification	28
2.3.1 Tide gauges.....	28
2.3.2 Altimetry data	28
2.4 Harmonic tidal analysis: Detidor	30
2.5 Tidal energy budget: COMODO-energy.....	30
Chapter 3: Model validation and sensitivity analysis in the Gulf of Tonkin....	34
3.1 Previous modeling work	34
3.2 Model setup	35
3.2.1 Grid generation	35
3.2.2 Surface fluxes.....	35
3.2.3 Initial and boundary conditions	40
3.3 Model validation.....	41

3.3.1	Tidal gauges.....	42
3.3.2	Satellite altimetry	47
3.4	Model sensitivity.....	50
3.4.1	Sensitivity to bottom stress formulation	52
3.4.2	Sensitivity to the horizontal resolution.....	54
3.4.3	Comparison of two- and three-dimensional model solutions	55
3.4.4	Sensitivity to bathymetry.....	57
3.5	Conclusion	59
	Appendix.....	60
A.1	Comparison of altimeter and tide gauge measurements.....	60
A.2	Relative errors	61
A.3	OTIS forcing.....	63
	Chapter 4: Tidal flux and resonance in the Gulf of Tonkin.....	64
4.1	Tidal energy flux.....	64
4.2	Tidal resonance	67
4.2.1	The rectangular bay model.....	67
4.2.2	Numerical simulations.....	70
	Chapter 5: Residual transports	73
5.1	Tide-induced residual current and transport	73
5.1.1	Eulerian residuals	73
5.1.2	Tide-induced Lagrangian residual current.....	75
5.2	Subtidal residual flow	77
5.2.1	Wind-driven circulation.....	78
5.2.2	Density circulation.....	79
5.3	Connectivity to Ha-Long bay.....	80
5.4	Conclusion	84
	Chapter 6: Heat budget	85
6.1	Coastal cooling in winter	85
6.2	Frontogenesis in spring-summer.....	87
	Conclusion	90
	References	92

Introduction

The Gulf of Tonkin ($16^{\circ}10' - 21^{\circ}30'N$, $105^{\circ}40' - 110^{\circ}00'E$; Figure 1.1) is a shallow, tropical, crescent-shape, semi-enclosed basin located in the northwest of the Vietnam East Sea/South China Sea (VES/SCS), which is the biggest marginal sea in the Northwest Pacific Ocean. Bounded by China and Vietnam to the north and west, the Gulf of Tonkin is 270 km wide and about 500 km long, connecting with the Vietnam East Sea/South China Sea through the south of the gulf and the Hainan Strait (also called Qiongzhou strait). This strait is about 20 km wide and 50 m deep in between the Hainan Island and the Qiongzhou Peninsula (mainland China). The southern Gulf of Tonkin is a NW-SE trending shallow embayment from 50 to 100 meters in depth. Many rivers feed the gulf, the largest being the Red River. The Red River flows from China, where it is known as the Yuan, then through Vietnam, where it mainly collects the waters of the Da and Lo rivers before emptying into the gulf through 9 distributaries in its delta. It provides the major riverine discharge into the gulf, along with some smaller rivers along the north and west coastal area. The mean annual discharge of the Red River is 3389 m³/s (Le et al., 2007). The Red River, annually transporting around 82 106 m³ of sediment (Do et al., 2007), flows into a shallow shelf sea forming a river plume that is advected southward by coastal currents.

Tides in the Vietnam East Sea/South China Sea (VES/SCS) have been studied since the 1940s. According to Wyrski (1961), the four most important tidal constituents (O1, K1, M2 and S2; Table 1.1) give a relatively complete picture of the tidal pattern of the region and are sufficient for a general description. However, the co-tidal and co-range charts (tidal phases and amplitudes of the main tidal constituents) proposed by various researchers before the 1980s revealed large uncertainties over the shelf areas. Discrepancies among the published charts were reduced after the 1980s when a number of numerical models were developed to improve the accuracy of tides and tidal current predictions. Among papers focusing on Chinese coastlines, we particularly note the two-dimensional, depth-integrated shallow water model of Fang et al. (1999) and the three-dimensional tidal models of Cai et al. (2005), Zu et al. (2008) and Chen et al. (2009). Zu et al. (2008) used data assimilation of TOPEX/POSEIDON altimeter data to improve predictions and Cai et al. (2005) explored the sensitivity of shelf dynamics to various model parameters and forcing. With a relatively coarse resolution (quarter degree) model, Fang et al. (1999) showed that tides in the Vietnam East Sea/South China Sea are essentially maintained by the energy flux of both diurnal and semidiurnal tides from the Pacific Ocean through the Luzon Strait situated between Taiwan and Luzon (Luzon is the largest island in the Philippines, located in the northernmost region of the archipelago). The major branch of energy flux is southwestward passing through the deep basin. The branch toward the Gulf of Tonkin is weak for the semidiurnal tide but rather strong for the diurnal tide. Semi-diurnal tides are generally weaker than diurnal tides in the Vietnam East Sea/South China Sea.

Other scientists (e.g., Nguyễn Ngọc Thụy, 1984; Manh and Yanagi, 2000) have studied tides in the Vietnam East Sea/South China Sea with more emphasis on the

Gulf of Tonkin, although model resolution remained low. What is known from these studies is that the tidal regime of the Gulf of Tonkin is diurnal (as in the VES/SCS), with larger amplitudes in the north at the head of the gulf. Diurnal tidal regimes are commonly microtidal, but the Gulf of Tonkin is one of the few basins with a meso-tidal, and locally even macrotidal, diurnal regime (van Maren et al., 2004). In open shelf areas, tidal amplification varies with the difference of squared frequencies between the tide and earth rotation (Clark and Battisti; 1981). The only possible configuration for large amplification of diurnal tides is thus bays and closed basins. In such small bodies of water, tides are primarily driven by the open ocean. Their propagation is much slower as they enter shallower waters but they are still influenced by earth rotation and have a similar anticlockwise propagation around the coasts (northern hemisphere) as open ocean tides. In some cases, amplification can occur by at least two processes. One is simply focusing: if the bay becomes progressively narrower along its length, the tide will be confined to a narrower channel as it propagates, thus concentrating its energy. The second process is resonance by constructive interference between the incoming tide and a component reflected from the coast. If the geometry of the bay is such that it takes one-quarter period for a wave to propagate its length, it will support a quarter-wavelength mode (zeroth or Helmholtz mode) at the forcing period, leading to large tides at the head of the bay. Tidal waves enter the Gulf of Tonkin from the adjacent Vietnam East Sea/South China Sea, and are partly reflected in the northern part of the Gulf. The geometry of the basin is believed to cause the diurnal components O1 and K1 to resonate. That would explain their pattern of amplitudes with an increase from the mouth to the head, where they reach their highest values in the whole of Vietnam East Sea/South China Sea (exceeding 90 cm for O1 and 80 cm for K1; Fang et al., 1999).

Thesis objectives

Coastal and offshore activities such as marine transportation, resource extraction, fishing and tourism are very important to economic development. Coastal areas are also home to species and habitats that provide many benefits to society and nature ecosystems. The increase of human activities causes pressure on the coastal zone off the Red River delta. It led to the degradation of waterways connected to Hai Phong Harbour due to the effect of increased turbidity and sediment buildup. Dredging has been conducted to remove large quantities of sediment from the seabed and deepen waterways. The Gulf of Tonkin also contains ecologically sensitive areas such as the Cat Ba Island national park and Ha Long bay recognized by the UNESCO as world heritage. To balance protection of the fragile ecosystem with sustainable economic growth, we need a better understanding of the entire region.

The scientific objective of this study is to quantify the dominant physical processes that characterize the dynamics of the Gulf of Tonkin with particular attention to tidal dynamics. The methodological objective is to build a robust and reliable, high-resolution hydrodynamic numerical model for the Gulf of Tonkin. The model is validated against available data from tidal gauges and coastal satellite altimetry data provided by LEGOS (CTOH service). It is based on the Regional

Ocean Modeling System (ROMS) in the AGRIF version used and developed at IRD (“Institut de Recherche pour le Développement”). Our modeling work comes with a sensitivities study of tidal solutions to model parameters and with diagnostics of tidal energy fluxes and resonance. The tidal residual flow in both the Eulerian and Lagrangian frameworks is evaluated and compared with wind-driven currents to assess their respective role in property transports. To complete our investigation, we analyze the heat budget of the gulf of Tonkin and the mechanisms involving tidal forcing as well as momentum and buoyancy forcing that may explain the formation of a cool coastal tongue commonly observed in winter and frontal formations in spring/summer.

Thesis outline

The structure of this thesis reflects the main objectives formulated above. The first chapter concentrates on the description of the characteristic elements of the Gulf of Tonkin dynamics. The bibliographic study conducted in this first part of the thesis provides a general description of the actual understanding of the system and leads to the identification of key questions relevant to the thesis. The second chapter gives a detailed presentation of the methods and tools used in this study. It describes the numerical model ROMS, the data used for validation, the tools used for tidal analysis and the Lagrangian diagnostic tool ARIANE. The computed tides are validated using an exhaustive compilation of available tidal gauges and coastal satellite altimetry data in Chapter 3. A sensitivity study of the model to key parameters such as bathymetry, coastline and bottom friction parameterization is performed. Chapter 4 is devoted to the model estimation of tidal energy flux and resonance spectrum in the gulf, which will be compared with idealized model solutions. In Chapter 5, the tidal residual currents are computed and discussed and Chapter 6 is devoted to heat budget analysis to explain observed seasonal features.

Chapter 1: Description of the Gulf of Tonkin

1.1 Geography



Figure 1.1: Geography of the Gulf of Tonkin

The Gulf of Tonkin ($16^{\circ}10' - 21^{\circ}30'N$, $105^{\circ}40' - 110^{\circ}00'E$; Figure 1.1) is a shallow, tropical, crescent-shape, semi-enclosed basin located in the northwest of the Vietnam East Sea/South China Sea (VES/SCS), which is the biggest marginal sea in the Northwestern Pacific Ocean. Bounded by China and Vietnam to the north and west, the Gulf of Tonkin is 270 km wide and about 500 km long, connecting with the Vietnam East Sea/South China Sea through the south of the gulf and the Qiongzhou Strait (Quynh Chau strait; also called Hainan strait). This strait is about 20 km wide and 100 m deep in between the Hainan Island and the Qiongzhou Peninsula (mainland China). The southern Gulf of Tonkin is a NW-SE trending shallow embayment from 50 to 100 meters in depth. Many rivers feed the gulf, the largest being the Red River. The Red River flows from China, where it is known as the Yuan, then through Vietnam, where it mainly collects the waters of the Da and Lo rivers before emptying into the gulf through 9 distributaries in its delta. It provides the major riverine discharge into the gulf, along with some smaller rivers along the north and west coastal area. The Red River, annually

transporting 100 million tons of sediment (van Maren, 2004), flows into a shallow shelf sea. The river plume is then advected to the south by coastal current.

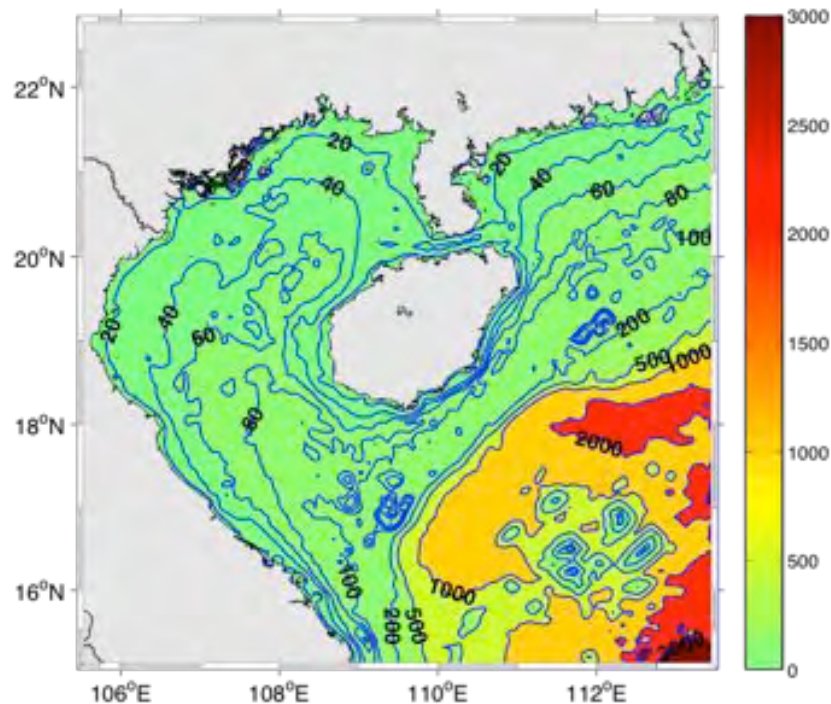


Figure 1.2: Map shows the major topographic features of the Gulf of Tonkin: Isobaths are in meters (m). Data from GEBCO_08.

There are topographic dataset available for the Gulf of Tonkin, like ETOPO2 (global digital bathymetry 2-minute resolution), DEM (digital elevation model 15-minute resolution) from Vietnamese navigation chart, GEBCO_08 (30-second resolution global bathymetry), Smith&Sandwell version 14 (1-minute resolution global bathymetry). GEBCO_08 is chosen here for our simulations because of its higher resolution and the fact that it contains data provided by the International Hydrographic Organization's (IHO) Member States for shallow water areas shallower than 300m. One of the focuses of IHO's technical assistance efforts is in the Vietnam East Sea/South China Sea. They contracted a study of shipping traffic patterns in the area and have been assessing the status of hydrographic surveying in the region (according to a report of improved global bathymetry by UNESCO, 2001).

1.2 Tidal forcing

According to Wyrтки (1961), the four most important tidal constituents in the Vietnam East Sea/South China Sea give a relatively complete picture of the tidal pattern of the region and are sufficient for a general description. These tides, with their periods T in hours are shown below in Table 1.1

Table 1.1: List of main tidal constituents

Tide	Description	Period (hrs)
M2	Semi-diurnal principal solar	12.42
S2	Semi-diurnal principal solar	12.00
K1	Diurnal solar	23.93
O1	Diurnal principal lunar	25.82

Tides in the Vietnam East Sea/South China Sea have been studied since the 1940s. The co-tidal and co-range charts (maps of tidal phase and amplitudes of the main tidal constituents) that were drawn by various researchers before the 1980s revealed large discrepancies over the shelf areas. The discrepancies among the published charts were reduced since the 1980s, when a number of numerical models were developed to improve the accuracy of tides and tidal current predictions. Recent examples are mostly Chinese: the two-dimensional, depth-integrated shallow water model of Fang et al. (1999) and the three-dimensional tidal models of Cai et al. (2005), Zu et al. (2008) and Chen et al. (2009). Zu et al. (2008) used data assimilation of TOPEX/POSEIDON altimeter data to improve predictions while Cai et al. (2005) explored the sensitivity of shelf dynamics to various model parameters and forcing. With a relatively coarse resolution (quarter degree) model, Fang et al. (1999) and Zu et al. (2008) showed that tides in the Vietnam East Sea/South China Sea are essentially maintained by the energy fluxes of both diurnal and semidiurnal tides from the Pacific Ocean through the Luzon Strait situated between Taiwan and Luzon (Luzon is the largest island in the Philippines, located in the northernmost region of the archipelago). The major branch of energy flux is southwestward passing through the deep basin. The branch toward the Gulf of Tonkin is weak for the semidiurnal tide but rather strong for the diurnal tide. The M2 tidal amplitude is reduced while the O1 amplitude is amplified after they pass through the Luzon strait. The results show that the M2 amplitude is generally small (<0.2m) at the entrance of the Gulf of Tonkin but the K1 and O1 amplitude are about 0.3m (Figure 1.3).

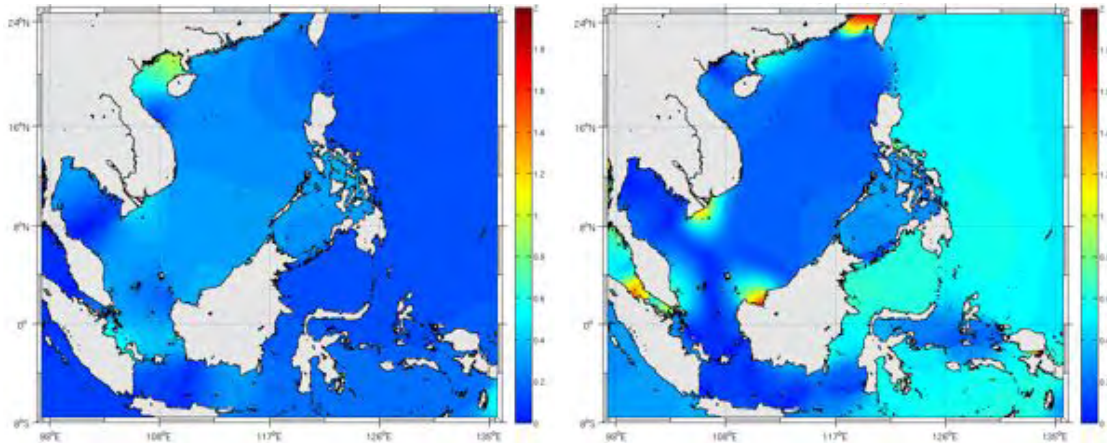


Figure 1.3: Amplitude in meter of O1 (left) and M2 (right) tides in the Vietnam East Sea/South China Sea, from the global tidal solutions FES2004 (Lyard et al., 2006)

Vietnamese scientists, e.g., Nguyễn Ngọc Thụy (1984), have also studied tides in the Vietnam East Sea/South China Sea since the 1980s, but the high-resolution dynamics of the Gulf of Tonkin remain poorly estimated. What is known is that the tidal regime of the Gulf of Tonkin is diurnal, with large amplitudes in the north decreasing in the south. Tidal currents are strong and complex. Tides in bays generally have larger amplitudes than in the open ocean but with similar anticlockwise propagation around the coasts (northern hemisphere). The propagation is also much slower consistent with the shallower water. In such small bodies of water, the effects of gravitational forcing acting directly on the water body are small compared with the indirect effects of open-ocean forcing. Therefore, tides in coastal seas and bays are driven primarily by the open ocean tide at the mouth of the bay. In some cases, this can lead to large amplitudes, by at least two processes. One is simply focusing: if the bay becomes progressively narrower along its length, the tide will be confined to a narrower channel as it propagates, thus concentrating its energy. The second process is resonance by constructive interference between the incoming tide and a component reflected from the coast. If the geometry of the bay is such that it takes one-quarter period for a wave to propagate its length, it will support a quarter-wavelength mode at the forcing period, leading to large tides at the head of the bay. Tidal waves enter the Gulf of Tonkin from the adjacent Vietnam East Sea/South China Sea, and are partly reflected in the northern part of the Gulf. The geometry of the basin causes the diurnal components O1 and K1 to resonate. Therefore, the amplitude of these components increases northward along the North Vietnamese coastline, where they reach their highest values in the whole of Vietnam East Sea/South China Sea (exceeding 90 cm for O1 and 80 cm for K1; Fang et al., 1999). The strongest diurnal tidal current occurs in the Hainan Strait.

More specifically, if we consider the Gulf of Tonkin as an ideal rectangular gulf of length L and constant water depth h , which communicates with a deep ocean at the open end, we can compute a solution for resonant modes (Taylor, 1922). For that, we assume that the gulf is sufficiently narrow for the Coriolis force to be neglected, and omit for simplicity the friction effects. In this case, the linear, non-

rotating, one-dimensional shallow water equations (under the assumption that at the closed end of the gulf the normal velocity is vanishing) take a solution in the form of a standing wave:

$$\bar{\zeta} = A_i \cos kx \cos \omega t \quad (1.1)$$

Where A_i is the amplitude at the gulf entrance ($x=L$), $\omega = ck$ is the frequency of incoming tide, $c = \sqrt{gh}$ its propagation speed. At the head of the gulf ($x=0$), the amplitude is $A = A_i/\cos(kL)$. Hence, if $\cos(kL)=0$ for $kL = \pi/2, 3\pi/2, \dots (2n-1)\pi/2$, $n=1,2,\dots$, resonance occurs. The first resonance mode (the Helmholtz mode, generally the most energetic) is associated with the non-dimensional gulf length $kL = \lambda/2$, i.e., with gulf length $L=\lambda/4$ the quarter wavelength, where λ is the length of incoming tidal wave. Thus:

$$\omega = \frac{\pi c}{2L} \quad (1.2)$$

The length of the Gulf of Tonkin is about 500 km and its average depth is 50 m. Therefore the resonance would occur for a tidal forcing period of $T = 25.1$ hours, which is close to the period of O1 (Fang et al., 1999).

However, neglecting the Coriolis force may not be appropriate (Van Maren et al., 2004). The incoming diurnal tidal waves tend to be deflected to the right by Coriolis forcing and reflect against the northern enclosure of the gulf. The reflected waves propagate southward and are partly dissipated by friction. The result is a mixture of a standing wave, a northward-propagating wave in the eastern part, and a southward-propagating wave in the western part. This suggests a wide range of phase relationships between tidal currents and high/low tides (as opposed to propagating waves, in standing waves currents are out of phase by 90° with water level). Coriolis forcing also produce a frequency shift of the resonant wave. Taylor (1922) and van Dantzig and Lauwerier (1960) proposed a general expression for this frequency shift, again for a rectangular basin. Jonsson et al. (2008) added a useful simplification for narrow bays (if the width is no more than half the length):

$$\omega = \frac{\pi c}{2L} + \frac{16Wf^2}{\pi^4 c} \quad (1.3)$$

W is the width of the basin (270 km for the Gulf of Tonkin) and f is the Coriolis frequency ($\sim 0.5 \cdot 10^{-4} \text{ s}^{-1}$ at 20°N). The period after correction for rotation is 23.4 hours, which is shorter than the period of O1 and closer to K1. However, we cannot expect the crude estimate of treating the Gulf of Tonkin as a flat-bottomed rectangular gulf to yield an accurate result. We will use our numerical model to provide a better estimate of the optimal resonant period under the influence of complex bathymetry and coastlines and of the Hainan Strait opening in the north.

1.3 Meteorological conditions

1.3.1 Winds

According to the literature, dynamical processes in the Vietnam East Sea/South China Sea are governed to a large extent by the Asian monsoon system. In this monsoon system a distinction can be made between the North East (NE) monsoon (also called winter or dry monsoon) and the South West (SW) monsoon (also called the summer or wet monsoon). This system follows the annual cycle (Wyrтки, 1961):

- From September to April the NE monsoon prevails. This monsoon is fully developed in January (8.0 - 10.7 m/s), prevails over the entire Vietnam East Sea/South China Sea. From February onwards, the NE monsoon weakens but prevails until April.
- From May to August the NE monsoon is succeeded by the SW monsoon. During May the NE winds over the Vietnam East Sea/South China Sea collapse and a SW wind succeeds. Its force increases over the following months, reaching full development in July and August (5.5 - 7.9 m/s). From September onwards, however, NE winds occur over the North East Sea and prevail over the entire Vietnam East Sea/South China Sea from October.

This annual cycle is illustrated in Figure 1.4 by monthly-mean wind stress fields for February and August (the NE and SW monsoon highs). These fields are obtained from QuikSCAT monthly climatology. They clearly show the inverted NE and SW monsoon wind directions. Also, it can be observed that during the NE monsoon the wind magnitude is essentially uniform over the entire Vietnam East Sea/South China Sea basin.

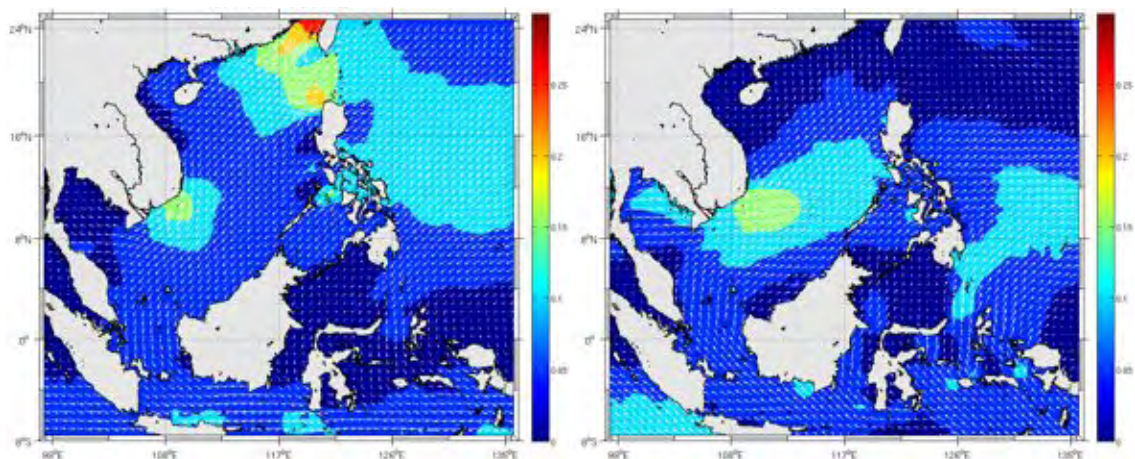


Figure 1.4: Monthly-mean surface wind stress for February (left) and August (right). Obtained from Monthly mean wind stress based on the QuikSCAT monthly climatology with magnitude in shaded [N/m²].

Figure 1.5 shows the wind-stress for the Gulf of Tonkin. This data is QuikSCAT monthly climatology and represents the area-averaged conditions over [16°10'–21°30'N, 105°40'–110°00'E]. A maximum wind stress is observed around December/January, when the NE monsoon is high. A second maximum is observed June/July, when the SW monsoon is high. April/May and August/September are periods of transition between monsoons.

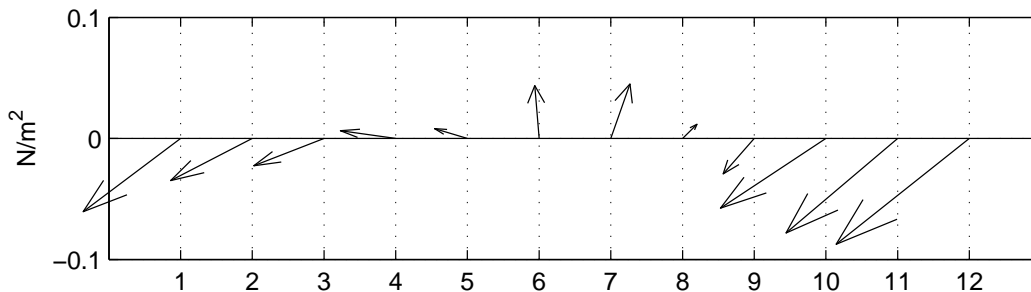


Figure 1.5: Monthly mean wind-stress in the Gulf of Tonkin [16°10'–21°30'N, 105°40'–110°00'E] from QuikSCAT monthly climatology (2000–2007).

1.3.2 Precipitation

The precipitation in the Vietnam East Sea/South China Sea is mainly controlled by the winter and summer monsoons. Most of the rainfall occurs during the summer monsoon (May–September), in the mountain areas it can reach up to more than 2000 mm (Figure 1.6).

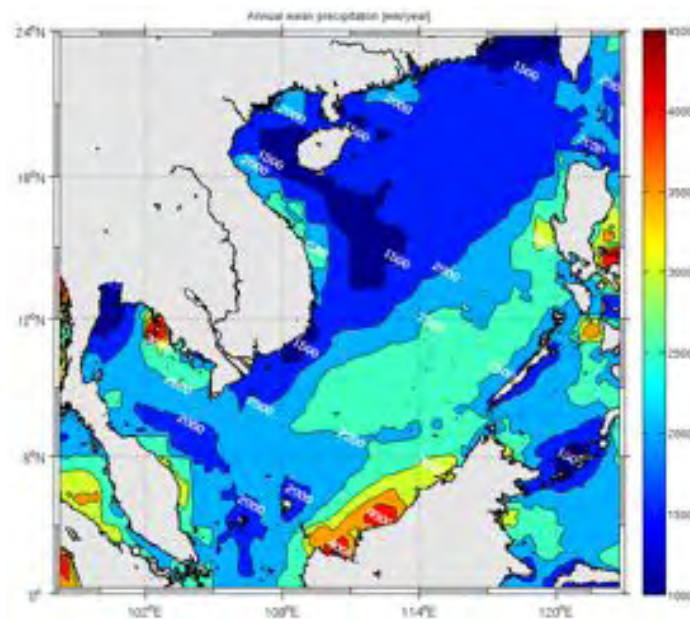


Figure 1.6: Annual mean precipitation [mm/year] from Tropical Rainfall Measuring Mission (TRMM_3B43) observations between 1998 and 2011.

1.3.3 Surface heat flux

The surface net heat flux Q_{net} is defined as:

$$Q_{\text{net}} = Q_{\text{sw}} - Q_{\text{lw}} - Q_{\text{lat}} - Q_{\text{sen}} \quad (1.4)$$

Q_{sw} and Q_{lw} are the heat fluxes due to solar short wave and long wave radiation respectively, Q_{lat} is the latent and Q_{sen} the sensible heat flux. The Vietnam East Sea/South China Sea lies between the equator and the Tropic of Cancer where the incident sunlight is practically vertical to the sea surface. The solar short wave radiation reaches its maximum in April because of the least cloud cover and the vertical incidence of sunlight. In winter Q_{sw} is lowest but due to the tropical position of the VES/SCS the annual range of values is mild. The latent heat transport Q_{lat} reaches its maximum in winter, due to the strong northeast monsoon with its cold, dry air. The latent heat flux has minimal during the transition periods between monsoons. As a result, the oceanic net heat gain Q_{net} reaches a maximum in April, drops quickly in May and is negative from October to February. The VES/SCS can store a large amount of heat energy and would exert a large influence on the atmospheric circulation and synoptic systems in eastern Asia. The sudden changes of Q_{sw} , Q_{lat} , Q_{net} in April-May reflect the quick adjustment of atmospheric circulation before the onset of summer SW monsoon. The VES/SCS acts as a source of heat and vapour to maintain the monsoon. It is the water evaporation and convective heating caused by the strong air-sea interactions that influence the local synoptic systems over the VES/SCS. There is also considerable spatial variability. The Gulf of Tonkin in particular is less affected by the summer monsoon winds than southern Vietnam (Figure 1.4).

The annual variation of SST in the VES/SCS is lowest in winter and rises swiftly after February (Figure 1.7). SST maximum does not appear in April while the surface net heat flux in the ocean is maximum, but lags by about one to two months. Then the SST drops with the decrease of Q_{net} . This implies that it is the surface net heat gain Q_{net} (not oceanic transport) that drives seasonal SST variations at regional scale (Yang, 1999).

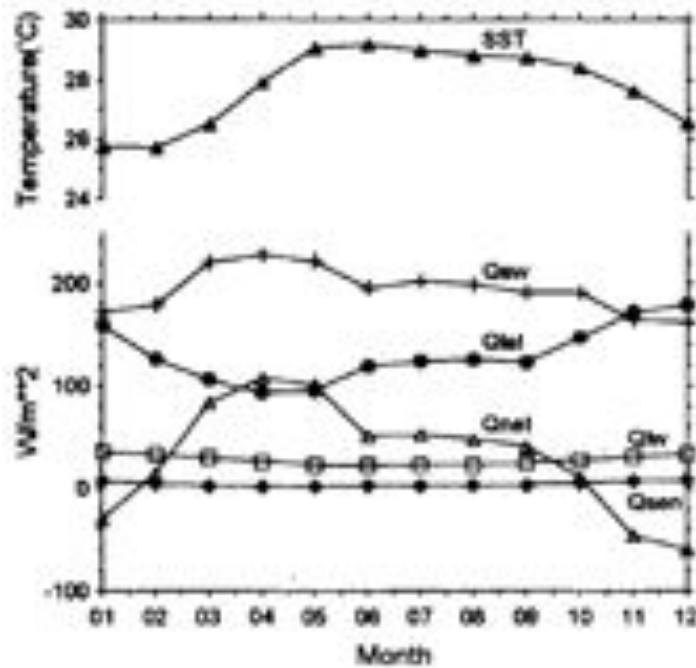


Figure 1.7: Annual variations of oceanic heat budget components ($\text{W}\cdot\text{m}^{-2}$) and sea surface temperature ($^{\circ}\text{C}$) averaged over the Vietnam East Sea/South China Sea. (Yang, 1999)

1.4 Ocean Climatology

1.4.1 Sea Surface Temperature patterns

During the NE monsoon (winter), the combined effect of surface heat flux and wind-driven basin-scale circulation contributes to the formation of a tongue of cold water along the northwest coast of the gulf. These processes contribute to seasonal amplitudes of over 6°C in the northwest gulf.

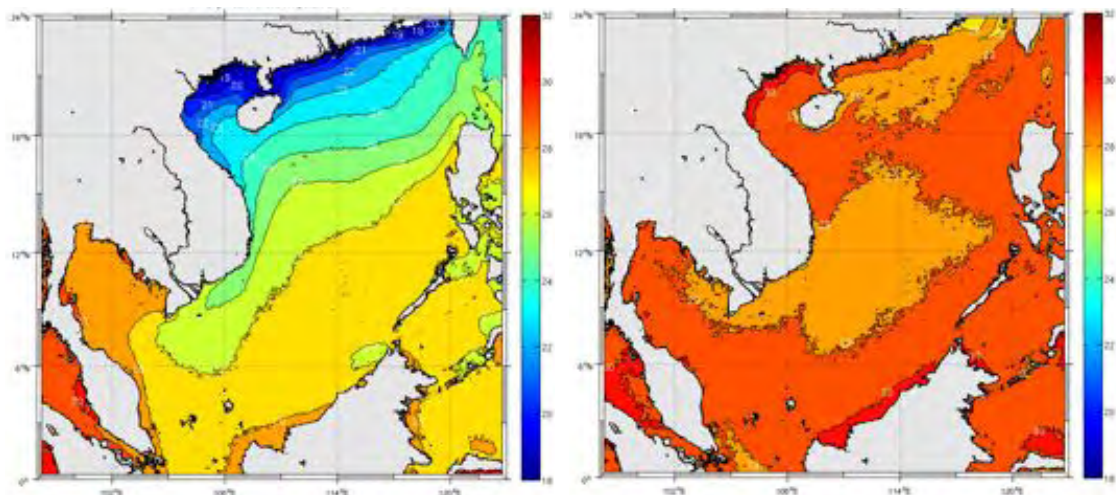


Figure 1.8: Monthly-mean sea surface temperature climatology for February (left) and August (right) from AVHRR Pathfinder Version 5.0/5.1 SST data for 1982-2008.

Figure 1.8 shows monthly-mean Sea Surface Temperature (SST) fields for February and August, these months were identified as the maximum of the NE and SW monsoons, respectively. They show that the largest seasonal amplitudes are located in the coastal zones, particularly in the Gulf of Tonkin.

1.4.2 Subtidal circulation

The Gulf of Tonkin is connected to the Vietnam East Sea/South China Sea and has a tropical climate with monsoon winds. It is semi-enclosed with an average water depth of 50 m. During the winter monsoon, the wind blows from the northeast generating a southward flow. During the dry season the southward flow dominates and is described by an anticlockwise rotating cell. During the wet season, the southern monsoon winds are weak in the gulf and become minimal in August. Then, there are two circulation cells, which diverge near the coastline of the Red River Delta.

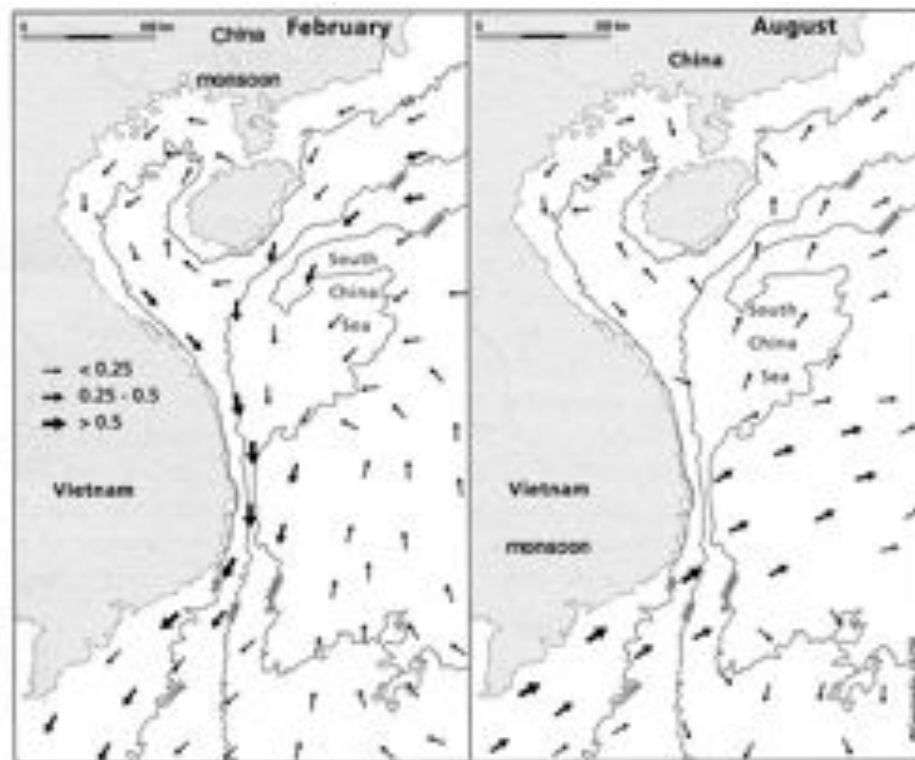


Figure 1.9: Residual flow in the Gulf of Tonkin during the dry season (February) and the wet season (August), based on the Vietnam National Atlas (1996). The 50, 200, and 2000 m depth contours are shown for reference.

Chapter 2: Methods

2.1 Description of the Regional Ocean Modeling System (ROMS)

ROMS (Shchepetkin and McWilliams, 2005) is an evolutionary descendent from the S-Coordinate Rutgers University Model (SCRUM: Song and Haidvogel, 1994), which started as a joint venture between UCLA and Rutgers University oceanographers. From this partnership, two branches of ROMS have emerged. A third version branched from UCLA: ROMS_AGRIF. This version is maintained jointly by IRD (P. Marchesiello, P. Penven and G. Cambon) and INRIA (L. Debreu), which are French institutes working on environmental sciences and applied mathematics. The main originality of this version is its 2 way nesting capability but is otherwise close to the UCLA version regarding the numerical kernel. The model evolution still benefit from frequent exchanges with UCLA (J. McWilliams, A. Shchepetkin, F. Lemarié, J. Molemaker and others) and with a growing body of developers and users of the model. ROMS is briefly presented here with references for further details on numerical schemes and physical parameterizations. Additional information can be found in a series of papers and documents available on the ROMS_AGRIF web site: <http://www.romsagrif.org> (in the documentation section).

ROMS solves the primitive equations in an Earth-centered rotating environment, based on the Boussinesq approximation and hydrostatic vertical momentum balance. It is discretized in coastline- and terrain-following curvilinear coordinates using high-order numerical methods. ROMS is a split-explicit, free-surface ocean model, where short time steps are used to advance the surface elevation and barotropic momentum, with a much larger time step used for temperature, salinity, and baroclinic momentum. The model has a 2-way, time-averaging procedure for the barotropic mode, which satisfies the 3D continuity equation. The specially designed 3rd-order predictor-corrector time step algorithm allows a substantial increase in the permissible time-step size and a reduction of small-scale numerical dispersion and diffusion. The complete time stepping algorithm is described in Shchepetkin and McWilliams (2005). Associated with the 3rd-order time stepping, a 3rd-order, upstream-biased advection scheme allows the generation of steep gradients, enhancing the effective resolution of the solution for a given grid size (Shchepetkin and McWilliams, 1998). Because of the implicit diffusion in the upstream-biased advection scheme, explicit lateral viscosity is not needed in ROMS, except in sponge layers near the open boundaries where it increases smoothly close to the lateral open boundaries. For tracers, a 3rd-order upstream-biased advection scheme is also implemented for tracers but the diffusion part of this scheme is rotated along isopycnal surfaces to avoid spurious diapycnal mixing and loss of water masses (Marchesiello et al., 2009; Lemarié et al., 2012). A non-local, K-profile planetary (KPP) boundary layer scheme (Large et al., 1994) parameterizes the unresolved physical vertical subgrid-scale processes at the surface, bottom and interior of the ocean. If a lateral boundary faces the open ocean, an active, implicit, upstream biased, radiation condition connects the model solution to the surroundings (Marchesiello et al., 2001). ROMS also include an

accurate pressure gradient algorithm (Shchepetkin and McWilliams, 2003) and a variety of features including air-sea bulk formulae, surface and benthic boundary layers. The model was therefore developed to simulate both coastal and oceanic regions and their interactions. Its computational methods allow for realistic, long-term integrations in a fine-mesh regional domain.

ROMSTOOLS (Penven et al., 2008) is a collection of global data sets and a series of Matlab programs collected in an integrated toolbox, developed for generating the grid, the surface forcing, initial conditions, open boundary conditions and tides for climatologically and inter-annual ROMS ocean simulation.

2.1.1 Equations of continuity and momentum balance

ROMS is a member of a general class of three-dimensional, free surface, terrain-following numerical models that solve the Reynolds-averaged Navier-Stokes equations using the hydrostatic and Boussinesq assumptions. The governing equations can be written in Cartesian coordinates:

$$\frac{\partial u}{\partial t} + u \frac{\partial u}{\partial x} + v \frac{\partial u}{\partial y} + w \frac{\partial u}{\partial w} - fv = -\frac{1}{\rho} \frac{\partial p}{\partial x} + A_x \frac{\partial^2 u}{\partial x^2} + A_y \frac{\partial^2 u}{\partial y^2} + A_z \frac{\partial^2 u}{\partial z^2} \quad (2.1)$$

$$\frac{\partial v}{\partial t} + u \frac{\partial v}{\partial x} + v \frac{\partial v}{\partial y} + w \frac{\partial v}{\partial w} + fu = -\frac{1}{\rho} \frac{\partial p}{\partial y} + A_x \frac{\partial^2 v}{\partial x^2} + A_y \frac{\partial^2 v}{\partial y^2} + A_z \frac{\partial^2 v}{\partial z^2} \quad (2.2)$$

$$\frac{1}{\rho} \frac{\partial p}{\partial z} = -g \quad (2.3)$$

with the continuity equation:

$$\frac{\partial u}{\partial x} + \frac{\partial v}{\partial y} + \frac{\partial w}{\partial z} = 0 \quad (2.4)$$

The equation of scalar transport is given by:

$$\frac{\partial T}{\partial t} + u \frac{\partial T}{\partial x} + v \frac{\partial T}{\partial y} + w \frac{\partial T}{\partial z} = K_H \left(\frac{\partial^2 T}{\partial x^2} + \frac{\partial^2 T}{\partial y^2} \right) + K_z \frac{\partial^2 T}{\partial z^2} + Q_T \quad (2.5)$$

$$\frac{\partial S}{\partial t} + u \frac{\partial S}{\partial x} + v \frac{\partial S}{\partial y} + w \frac{\partial S}{\partial z} = K_H \left(\frac{\partial^2 S}{\partial x^2} + \frac{\partial^2 S}{\partial y^2} \right) + K_z \frac{\partial^2 S}{\partial z^2} + Q_S \quad (2.6)$$

The equation of state provides the density fields:

$$\rho = \rho(T, S, P) \quad (2.7)$$

Equation (2.1) and (2.2) express the momentum balance in the x- and y- direction, respectively. Equation (2.5) and (2.6) are called the advection-diffusion equations. (u, v, w) are the velocity components in x, y, z-directions (in unit of m/s); t is time (in unit of s), (x, y, z) are rectangular position coordinates in the east-west, north-south and vertical directions (in unit of m); f is the Coriolis parameter, $f = 2\Omega \sin \phi$, with Ω is angular speed of rotation of earth about its axis and ϕ is geographic latitude; P is dynamic pressure (in unit of Pa), g is acceleration of gravity (in unit of m/s^2), T is potential temperature (in unit of $^{\circ}C$), S is salinity (in ‰: parts of thousands), A_x, A_y, A_z are kinematic eddy viscosity for x, y, z-directions (in unit of m^2/s); K_x, K_y, K_z are kinematic eddy diffusivity for x, y, z-directions (in unit of m^2/s); Q_T is temperature (heat) source function (in unit of $^{\circ}C/s$); Q_S is the contribution of evaporation minus precipitation and river discharge to salt flux (in ‰/s).

2.1.2 Vertical boundary conditions.

The vertical boundary conditions can be prescribed as follows, at the top ($z = \zeta(x, y, t)$):

$$\left(A_z \frac{\partial u}{\partial z} \right)_{z=\zeta} = \frac{\tau_x^{wind}}{\rho_o} \quad (2.8)$$

$$\left(A_z \frac{\partial v}{\partial z} \right)_{z=\zeta} = \frac{\tau_y^{wind}}{\rho_o} \quad (2.9)$$

$$w_s = \frac{\partial \zeta}{\partial t} - u_s \frac{\partial \zeta}{\partial x} + v_s \frac{\partial \zeta}{\partial y} \quad (2.10)$$

where ζ is surface elevation . The components of the wind-stress vector are given by: $\tau_x^{wind} = \rho_{air} C_d U \sqrt{U^2 + V^2}$ and $\tau_y^{wind} = \rho_{air} C_d V \sqrt{U^2 + V^2}$

where ρ_{air} is air density, C_d is nondimensional wind-drag coefficient with values of the order of $1.1-1.5 \times 10^{-3}$, and U, V are horizontal components of the wind vector measured at a height of 10m above sea level.

The surface boundary condition for heat:

$$\left(\rho_o C_p K_z \frac{\partial T}{\partial z} \right)_{z=\zeta} = Q_t \quad (2.11)$$

where ρ_o is surface density; C_p is specific heat capacity at constant pressure; Q_t is surface total heat flux, the total heat flux consists of the short wave flux (Q_{sw}) minus the net long-wave radiation (Q_{lw}) and the latent (Q_{lat}) and the sensible heat fluxes (Q_{sen}): $Q_t = Q_{sw} - Q_{lw} - Q_{lat} - Q_{sen}$. We usually choose to compute Q_t using the surface temperature and the atmospheric fields in an atmospheric bulk flux parameterization (Fairall et al., 2003). This bulk flux routine also computes the wind stress from the wind velocity.

For the salinity flux we consider:

$$\left(K_z \frac{\partial S}{\partial z} \right)_{z=\zeta} = (E - P)S \quad (2.12)$$

Where K_H is kinematic eddy diffusivity for horizontal direction (x, y); E is evaporation rate, P is precipitation

And at the bottom ($z = -H(x, y)$)

$$\left(A_z \frac{\partial u}{\partial z} \right)_{z=-H} = \frac{\tau_x^{bottom}}{\rho_o} \quad (2.13)$$

$$\left(A_z \frac{\partial v}{\partial z} \right)_{z=-H} = \frac{\tau_y^{bottom}}{\rho_o} \quad (2.14)$$

$$\left(K_z \frac{\partial T}{\partial z} \right)_{z=-H} = 0 \quad (2.15)$$

$$\left(K_z \frac{\partial S}{\partial z} \right)_{z=-H} = 0 \quad (2.16)$$

$$-w_b + u_b \frac{\partial H}{\partial x} + v_b \frac{\partial H}{\partial y} = 0 \quad (2.17)$$

At the bottom, $z = -H(x, y)$, the horizontal velocity has a prescribed bottom stress which is a choice between linear, quadratic, or logarithmic terms.

$u_s, v_s, w_s, u_b, v_b, w_b$ are the velocity components at the free surface ($z = \zeta$) and at the bottom ($z = -H$) assuming a slip condition is applied at the base of the water column.

2.1.3 Terrain-following coordinate systems

The advantage of terrain-following vertical coordinates is a natural handling of surface and bottom boundary conditions, which is essential for a proper

representation of flow-topography interactions in regions with complex topography; it also provides greater vertical resolution in shallow water. Following Song and Haidvogel (1994) modified by Shchepetkin and McWilliams (2005), the vertical coordinate is defined as:

$$z = \zeta(1 + \sigma) + h\sigma + (h - h_o)C(\sigma), -1 \leq \sigma \leq 0 \quad (2.18)$$

where h_o is either the minimum depth or a shallower depth above which we wish to have more resolution. $C(\sigma)$ is defined as:

$$C(\sigma) = (1 - b) \frac{\sinh(\theta\sigma)}{\sinh\theta} + b \frac{\tanh\left[\theta\left(\sigma + \frac{1}{2}\right)\right] - \tanh\left(\frac{1}{2}\theta\right)}{2 \tanh\left(\frac{1}{2}\theta\right)} \quad (2.19)$$

where θ and b are surface and bottom control parameters. Their ranges are $0 < \theta \leq 20$ and $0 \leq b \leq 1$, respectively. Equation leads to $z = \zeta$ for $\sigma = -1$.

Here are some features of this coordinate system:

-It is a generalizations of the traditional σ -coordinate system when θ goes to zero

$$z = (\zeta + h)(1 + \sigma) - h \quad (2.20)$$

-The larger the value of θ , the more resolution is given above h_o .

-For $b=0$, refinement is only provides to the surface as θ is increased.

-For $b=1$, refinement is given both to the surface and bottom equally as θ is increased.

Figure 2.1 shows σ -surfaces for several values of θ and b for the same domain.

The vertical cell size is:

$$H_z = \frac{\partial z}{\partial \sigma} = (\zeta + h) + (h - h_o) \frac{\partial C(\sigma)}{\partial \sigma} \quad (2.21)$$

The derivative of $C(\sigma)$ can be computed analytically:

$$\frac{\partial C(\sigma)}{\partial \sigma} = (1 - b) \frac{\cosh(\theta\sigma)}{\sinh(\theta)} \theta + b \frac{\cosh\left(\frac{1}{2}\theta\right)}{2 \cosh^2\left[\theta\left(\sigma + \frac{1}{2}\right)\right]} \theta \quad (2.22)$$

However, H_z is computed discretely as $\Delta z / \Delta \sigma$ since this leads to the vertical sum of H_z being exactly the total water depth D .

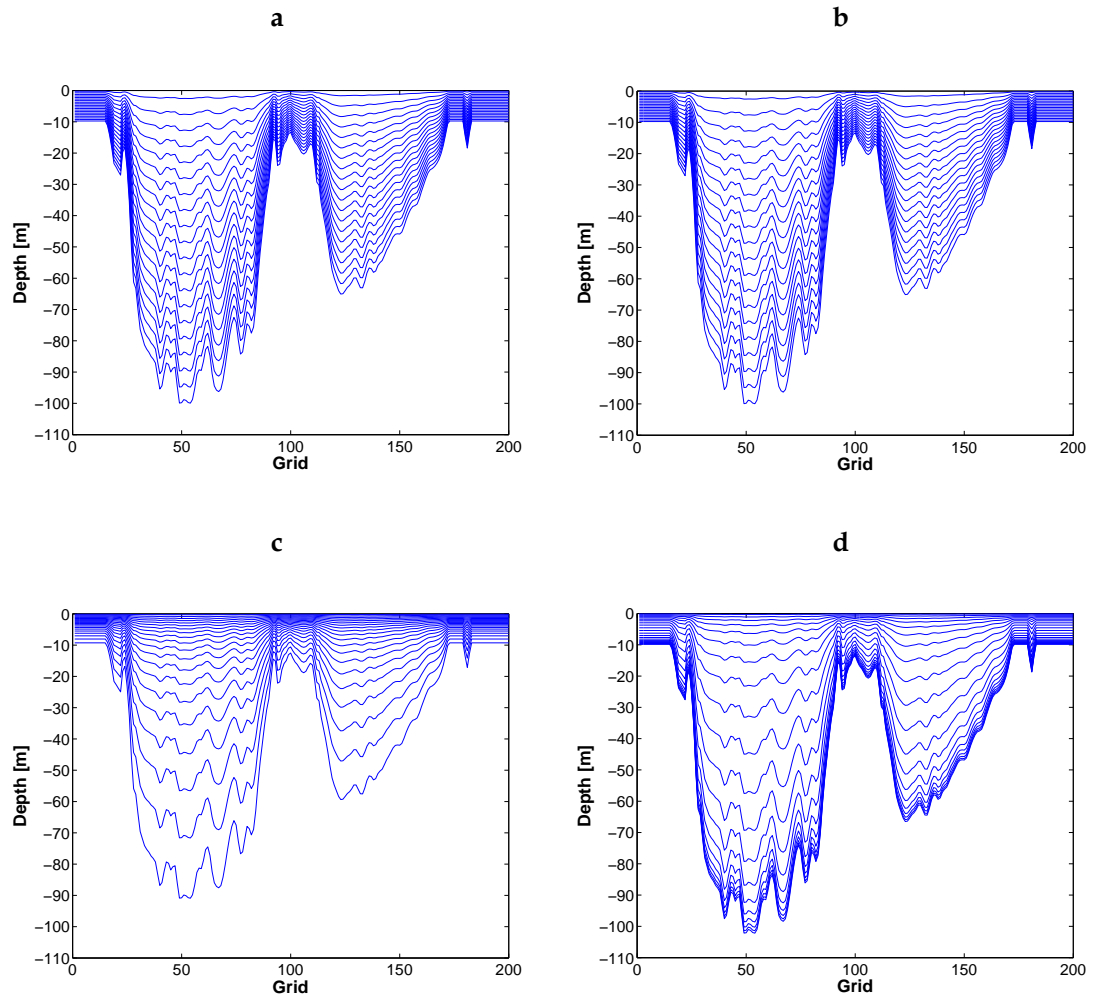


Figure 2.1: Examples of σ -surfaces for the study domain with (a) $\theta = 0.0001$ and $b = 0$, (b) $\theta = 0.0001$ and $b = 1$, (c) $\theta = 5$ and $b = 0$. (d) $\theta = 5$ and $b = 1$.

The vertical discretization also uses a staggered finite-difference approximation as shown in Figure 2.2.

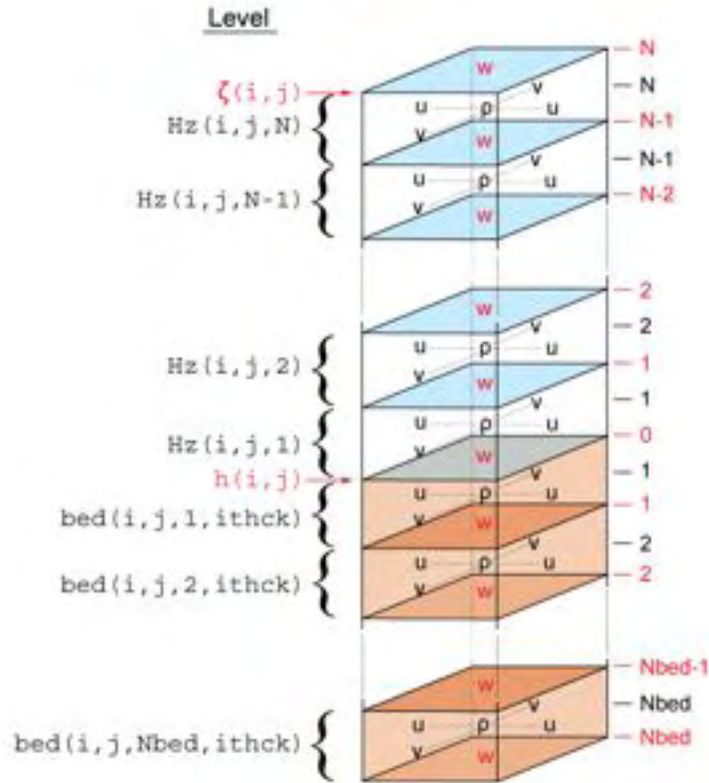


Figure 2.2: Placement of variables on staggered vertical grid.

2.1.4 Horizontal curvilinear coordinates

Orthogonal curvilinear coordinates are used in the horizontal allowing for spherical grids or increased horizontal resolution in regions characterized by irregular coastal geometry. Let the new coordinates be $\xi(x,y)$ and $\eta(x,y)$, where the relationships of horizontal length to the differential distances is given by:

$$(ds)_{\xi} = \left(\frac{1}{m}\right) d\xi \quad (2.23)$$

$$(ds)_{\eta} = \left(\frac{1}{n}\right) d\eta \quad (2.24)$$

Here $m(\xi,\eta)$ and $n(\xi,\eta)$ are the scale factors which relate the differential distances $(\Delta\xi, \Delta\eta)$ to actual (physical) lengths.

In the horizontal (ξ,η) , a staggered grid for finite-difference approximate is adopted with arrangement of variables as shown is Figure 2.3. This is equivalent to the well know Arakawa "C" grid, which is well suited for problems with high horizontal resolution.

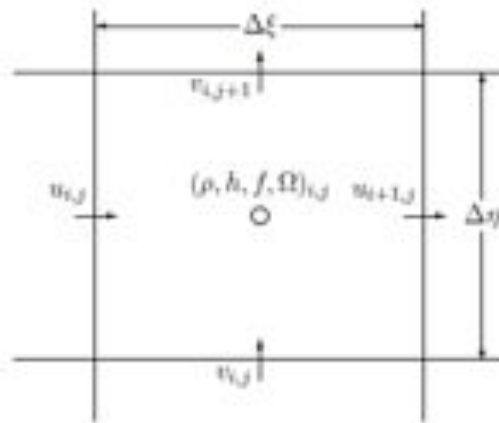


Figure 2.3: Placement of variables on an Arakawa C grid

The practice of coastline-following grids was often used in the past in coastal modeling (e.g., the Princeton Ocean Model, POM, applications) in order to improve the accuracy of coastal boundary conditions and limit land masking as much as possible; in the same time, an increase of resolution in coastal areas was possible. However, a major drawback of this technique is the loss of numerical accuracy when cell sizes are uneven and sometimes imperfectly orthogonal. For this reason, ROMS configurations are generally rectangular. In this case, masking out land areas, providing straightforward boundary conditions, represents the coastal boundary (Figure 2.4). Note that these coastal boundary conditions have a limited impact on the solution because in sigma coordinates the coastal areas are very shallow and dominated by bottom rather than lateral friction, i.e., more akin to a natural boundary condition.

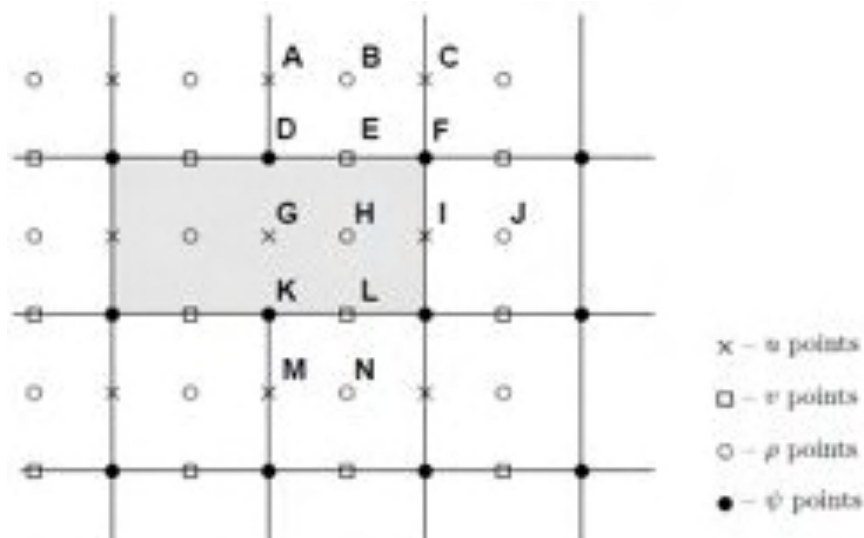


Figure 2.4: Masked region within the domain

2.1.5 Open boundary conditions

Open boundary conditions are more problematic because they constitute an artificial procedure destined to confine the computational domain within the region of interest. It saves computational resources but must be used with care to limit the propagation of boundary condition errors to the interior domain (Marchesiello et al., 2001; Blayo and Debreu, 2005). In ROMS, a combined set of passive (radiative) and active (relaxation to forcing data) open boundary conditions are provided for u , v , T , S and ξ , following the method of Marchesiello et al. (2001).

Coastal modeling requires well-behaved, long-term solutions for configurations with open boundaries. A numerical boundary scheme should allow the inner solutions to radiate through the boundary without reflection and information from the surrounding ocean to enter the model. The active open boundary scheme implemented in ROMS estimates the two dimensional horizontal phase velocities in the vicinity of the boundary. For each model variable ϕ , the normal (c_x) and tangential (c_y) phase velocities are:

$$c_x = - \frac{\frac{\partial \phi}{\partial t} \frac{\partial \phi}{\partial x}}{\left(\frac{\partial \phi}{\partial x}\right)^2 + \left(\frac{\partial \phi}{\partial y}\right)^2} \quad (2.25)$$

$$c_y = - \frac{\frac{\partial \phi}{\partial t} \frac{\partial \phi}{\partial y}}{\left(\frac{\partial \phi}{\partial x}\right)^2 + \left(\frac{\partial \phi}{\partial y}\right)^2} \quad (2.26)$$

Radiation conditions are used on all 3D model fields; while open boundary conditions for the free-surface and depth-averaged momentum are given by a Flather-type formulation (Flather, 1976) based on characteristic equations for shallow water models. These barotropic conditions are particularly well suited for tidal modeling as they smoothly allow both tidal forcing and propagation through the boundaries at the same time.

2.1.6 Time-stepping

The model time stepping involves three time levels: current time t , past time $t-dt$ (dt is the time-step), and future time $t+dt$ at which the model fields need to be estimated. For computational economy, the hydrostatic primitive equations for momentum are solved using a split-explicit time-stepping scheme, which requires special treatment and coupling between barotropic (fast/2D) and baroclinic (slow/3D) modes. A finite number of barotropic time steps, within each baroclinic step, are carried out to evolve the free-surface and vertically integrated momentum equations. Fast moving gravity waves such as tides are solved by the

barotropic equations. In order to avoid the errors associated with the aliasing of frequencies resolved by the barotropic steps but unresolved by the baroclinic step, the barotropic fields are time averaged before they replace those values obtained with a longer baroclinic step. The 3D equations are time-discretized using a third-order accurate predictor (Leap-Frog) and corrector (Adams-Moulton) time-stepping algorithm, which is robust and accurate. The enhanced stability of the scheme allows larger time steps, which more than offsets the increased cost of the predictor-corrector algorithm. The 2D mode is advanced using a forward-backward algorithm with also very good numerical properties.

2.1.7 Sigma-coordinate errors: The pressure gradient and diffusion terms

The major advantage of sigma coordinate models is the transformation of the surface and sea bottom to coordinate surfaces. Unfortunately, this is also the source of their major disadvantage: the well-known pressure gradient error that is most acute on steep continental slopes.

In sigma-coordinate, the x-component of the pressure gradient force is determined by:

$$\left. \frac{\partial p}{\partial x} \right|_{z=cst} = \left. \frac{\partial p}{\partial x} \right|_{\sigma=cst} - \frac{\sigma}{h} \frac{\partial p}{\partial \sigma} \frac{\partial h}{\partial x} \quad (2.27)$$

The first term of the right hand side involves the variation of pressure along a constant σ -surface and the second is the hydrostatic correction. Near steep topography, these 2 terms are large, comparable in magnitude and tend to cancel each other. A small error in computing either term can result in a relatively large error in the resulting horizontal pressure gradient. Beckman and Haidvogel (1993) show that this error is proportional to the slope number: the ratio of topographic variation and topographic depth. They found empirically that this ratio must be lower than a certain threshold ($|(h(i+1)-h(i))/(h(i+1)+h(i))| < 0.2$; i is the x grid index) to yield acceptable errors (erroneous currents lower than about 1 cm/s). Another source of pressure-gradient error is associated with vertical resolution and is called hydrostatic inconsistency (Haney, 1991). Consistency requires a limit to vertical resolution (given a certain horizontal resolution) but this limit depends on the pressure gradient scheme (Barnier et al., 1998).

The scheme implemented in ROMS is the formulation proposed by Shchepetkin and McWilliams (2003), based on high order density profile reconstruction and re-writing of the equation of state to reduce spurious water compressibility effects on the pressure gradient. This formulation has been designed to minimize truncation errors and is one of the most successful among the large list of schemes proposed in the literature.

Another related problem is that of spurious diapycnal mixing of tracers due to numerical diffusion naturally orientated along sigma surfaces. Spurious mixing produces errors on water masses and currents (due to the geostrophic balance) that can be even more dramatic than pressure gradient errors but much less

attention has been given to the former in the literature. A solution to this problem is to rotate the diffusion tensor (similarly to the pressure gradient but multiple derivatives can be involved) along geopotential surfaces or even better along isopycnal surfaces. Barnier et al. (1998) proposed the first rotated scheme for Laplacian diffusion. Recently, Marchesiello et al. (2009) proposed a new scheme for rotated biharmonic diffusion along geopotential surfaces and Lemarié et al. (2012) completed this scheme for isopycnal surfaces. It is based on a semi-implicit treatment of vertical fluxes, which removes the CFL stability condition, a well know problem for isopycnal diffusion even in climate models.

With robust and accurate corrections to both pressure gradient and diffusion errors ROMS is thus particularly well suited to represent both the continental shelf and ocean dynamics and exchanges across the continental slope

2.1.8 Turbulent closure

The parameterization of unresolved vertical mixing processes in ROMS follows the formulation of Large et al. (1994). It consists of two distinct parameterizations, a non-local, K-profile parameterization (KPP) for surface and bottom boundary layers and an ocean interior scheme. The depth of surface or bottom boundary layers (HBL and HBBL) is determined by equating a bulk Richardson number relative to the surface (or bottom) to a critical value. They thus are strongly dependent on buoyancy and momentum forcing as well as stratification and velocity profiles. In the ocean interior, vertical mixing is regarded as the superposition of 3 processes: vertical shear, internal wave breaking and double diffusion. In addition convective adjustment in case of static instability is provided by a large mixing coefficient. At the interface between boundary layers and the ocean interior, both diffusivity/viscosity and its gradient are forced to match the interior values.

In addition, and this is specific to ROMS_AGRIF, if the surface boundary layer extends to the bottom, we assume that the neutral boundary layer similarity theory holds at the bottom. The bottom boundary condition $A_z \partial u / \partial z = \tau / \rho_0$ then translates into $A_z = \kappa u_* z$ (κ is the von Karman constant, u_* the friction velocity and z is height above the bottom) which serves as a boundary condition for A_z . This gives large improvement to tidal mixing representation in shallow water.

2.1.9 Nesting

ROMS is discretized on a structured grid, so local refinement can be performed via nested grids (i.e., fixed high-resolution local grid embedded in a larger coarse grid). The interactions between the two components are twofold (2-way nesting): the lateral boundary conditions for the fine grid are supplied by the coarse grid solution, while the latter is updated from the fine grid solution in the area covered by both grids (Blayo & Debreu, 1999). The method for embedded gridding takes advantage of AGRIF (Adaptive Grid Refinement in Fortran), a generic coupler with the ability to manage an arbitrary number of embedding levels (as well as adaptive grid refinement, but this feature has not been extensively used).

A recursive integration procedure manages the time evolution for the child grids during the time step of the parent grids. In order to preserve the CFL criterion, for each parent time step the child must be advanced using a time step divided by the coefficient of refinement (e.g., a refinement of 3 for a 5 km grid embedded in a 15 km grid) as many times necessary to match the time of the parent.

2.2 Lagrangian modeling: Ariane

ARIANE (Blanke et al., 1997) is developed in the “Laboratoire de Physique des Océans” (LPO) in Brest by Bruno Blanke and Nicolas Grima. It is a code that temporally integrates the velocity field to compute trajectories. The package contains the FORTRAN 95 code and Matlab tools for graphic outputs and streamfunction calculation. ARIANE computes trajectories from the 3-dimensional Eulerian velocity field. For that, the velocity field must be interpolated at each particle location along their trajectory. The algorithm is detailed in Blanke and Arhan (1999). It takes advantage of the C-grid used to discretize ROMS equations and provides trajectories for a given velocity field through the computation of 3-dimensional streamlines. The 3 components of the velocity field are known over the six faces of each cell. The non-divergence of the velocity field ensures continuous trajectories within the cell.

ARIANE can be used in two different modes, qualitative and quantitative:

- The qualitative mode uses individual particles to display realistic trajectories. This mode is useful to simulate the trajectory of individual Lagrangian drifters or buoys and assesses the connectivity between various locations. The maximum duration of the particle drift corresponds to the duration of stored data. To initialize the particles in the domain, ARIANE uses five parameters, three spatial ones, a temporal one and a last parameter read but not used in qualitative mode (it is present for consistency with the quantitative mode inputs). The spatial parameters are given in number of cell grid, i.e. we do not indicate longitude, latitude and depth but the corresponding grid cell number.
- The quantitative mode uses thousands or more particles to compute a Lagrangian streamfunction and determine Lagrangian transports. The streamfunction is computed on the horizontal plan of a non-divergent flow, diagnosed by the movement of particles each associated with a weight (volume of water in m^3). In this mode, particles are initialized on a section defined by longitude, latitude and depth limits and intercepted by the same section or different ones. The ensemble of sections must form a closed domain to ensure that a quantitative diagnostic is possible.

2.3 Data for model verification

2.3.1 Tide gauges

The sea surface elevation was recorded at tidal stations along the coast in the Gulf of Tonkin. Data were collected from 30 tidal stations for model verification. The position of these stations is indicated in Figure 2.5. The harmonic constants are taken from the archives of the Institute of Oceanology, Chinese Academy of Sciences, from the British Admiralty Tide and Tidal Stream Tables (Chen et al., 2009). They are generally based on at least one-year observation.

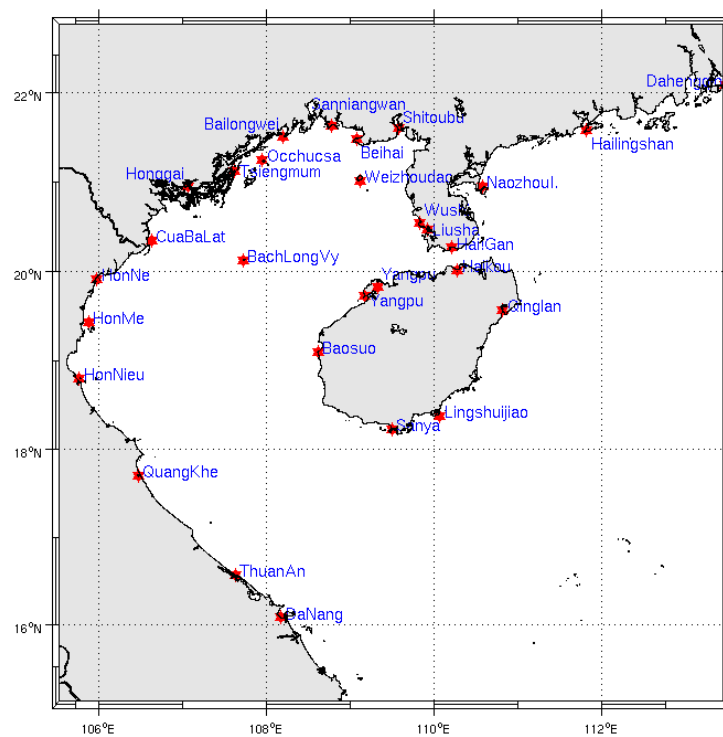


Figure 2.5: The position of the tidal stations for model verification

2.3.2 Altimetry data

Tide gauge measurements have some limitations due to their coastal locations: they describe very shallow water dynamics often biased by local coastal features. In contrast, satellite altimetry provides a global coverage and appears as an efficient way to monitor tidal elevations. With sufficient sampling (5 years and more), estimations of tidal amplitudes are given with an accuracy of a few centimeters.

However, some limitations are associated with the coastal zone, where altimeter observations are often of lower quality. Technically, satellite altimetry is a measure of the travel time taken by a radar pulse to travel from the satellite antenna to the surface and back to the satellite receiver. The use of satellite altimetry observations in coastal regions is limited due to coastal contamination and a discrepancy

between the satellite repeat period and the time scale of sea surface height variability. The treatment of coastal altimetry data used in this study was developed, validated, and distributed by the Centre for Topographic studies of the Oceans and Hydrosphere (CTOH/LEGOS, France). The CTOH is a French Observation Service dedicated to satellite altimetry studies. CTOH developed a processing toolbox, X-TRACK (Roblou et al., 2007) for improved altimeter treatment dedicated for coastal applications. The objective of this processor is to improve both the quantity and quality of altimeter sea surface measurements in coastal regions by applying standard corrections adapted to marginal seas. X-TRACK uses all accurate altimeter missions: Topex/Poseidon (2/11/1992-12/8/2002), Jason-1 (16/1/2002-27/1/2009), Jason-2 (13/7/2008-30/5/2011), Geosat Follow on (8/1/2000-8/9/2008) and Envisat (01/10/2002-14/9/2010). Amplitude and phase lag for each tidal constituent can be locally recovered with CTOH specific harmonic analysis software. In this thesis, apart from 16-year-long continuous record of TOPEX/Poseidon and Jason-1, we used also 5 years of TOPEX-Jason-1 interleaved mission. Interleaved mission means the satellite was shifted on a new orbit (moved longitudinally but keeping the same inclination and cycle length).

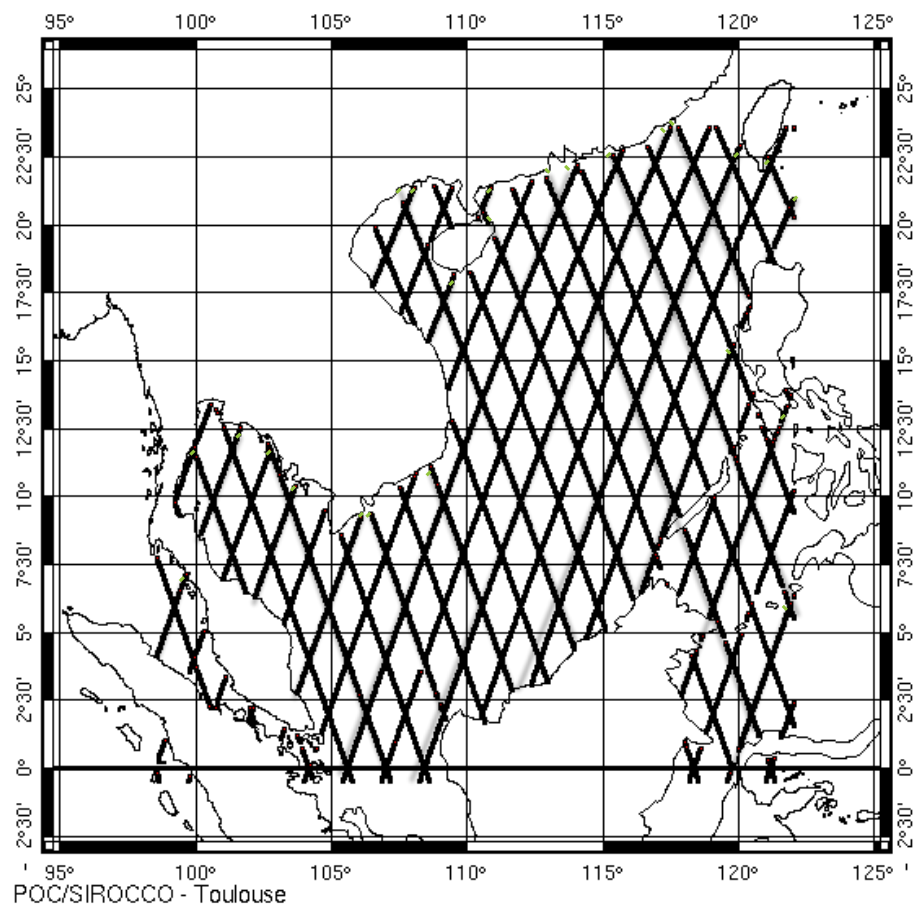


Figure 2.6: Joint TOPEX, Jason 1 and Jason 2 track of primary mission (green lines) and interleaved mission (black lines) in the Vietnam East Sea/South China Sea.

2.4 Harmonic tidal analysis: Detidor

Detidor is a post-processing tool developed at LEGOS for treatment of tidal signals in time series of model and observational data. One of the primary uses of Detidor calculations is to separate out the tidal from the non-tidal components by performing a harmonic tidal analysis. Harmonic analysis is most useful for the analysis and prediction of tidal elevations and currents. The use of this technique for tides appears to have originated with Lord Kelvin (1824-1907) around 1867. A discussion of tidal harmonic analysis can be found in Admiralty manual of Tides (Doodson and Warburf, 1941) and Godin (1972). The harmonic method of analysis treats every tidal record as consisting of a sum of harmonic constituents of known frequency. At time t , the harmonic expression of the ocean tidal height at location (λ, ϕ) can be written as:

$$\xi(\lambda, \phi, t) = \sum_k H_k(\lambda, \phi) \cos[\theta_k(t) + \chi_k - G(\lambda, \phi)] \quad (2.28)$$

where $H_k(\lambda, \phi)$, $G_k(\lambda, \phi)$ are the unknown amplitude and Greenwich phase lag of tide k at location (λ, ϕ) , and θ_k and χ_k are the amplitude and phase corrections. To avoid the singularities of the amplitude at the amphidromes, it is more common to give equation 2.28 the following form with cosine and sine functions:

$$\xi(\lambda, \phi, t) = \sum_k [C_k(\lambda, \phi) \cos(\theta_k(t) + \chi_k) + S_k(\lambda, \phi) \sin(\theta_k(t) + \chi_k)] \quad (2.29)$$

where $C_k = H_k \cos(G_k)$ and $S_k = H_k \sin(G_k)$.

To account for the nodal correction on the lunar tide, lunar nodal modulation factors are introduced to the harmonic expression of the tidal height (Munk and Cartwright, 1966; Schureman, 1971; Schwiderski, 1980):

$$\xi(\lambda, \phi, t) = \sum_k [f_k C_k(\lambda, \phi) \cos(\theta_k(t) + \chi_k + \mu_k) + f_k S_k(\lambda, \phi) \sin(\theta_k(t) + \chi_k + \mu_k)] \quad (2.30)$$

where f_k is the nodal factor, μ_k is the nodal angle. Both of them depend on the position of the lunar node and hence vary slowly with time in the 18.6-year nodal period. For the purpose of solving the unknown amplitude H_k and phase lag G_k through the least squares estimation procedure.

2.5 Tidal energy budget: COMODO-energy

COMODO-energy is a diagnosis tool developed at LEGOS for calculating the energy budget of the barotropic tides. The energy budget is calculated from tidal atlases (harmonic constant of sea surface elevation and barotropic currents). Here

we reintroduce a brief description of the equations. More detailed derivation can be found in Pairaud et al. (2008).

The derivation of the barotropic energy equations are based on the three-dimensional Reynolds-averaged Navier-Stokes equations under the Boussinesq approximation, along with the density transport equation and the continuity equation:

$$\frac{\partial u}{\partial t} + u \cdot \nabla u = -2\Omega \times u - g\nabla\eta + F + D \quad (2.31)$$

Where F and D are the astronomical forcing and the dissipation:

$$F = (1 + k_2 - h_2)g\nabla\Pi_a + g\nabla\Pi_{LSA} \quad (2.32)$$

$$D = \nabla \cdot (A\nabla u) - \frac{C}{H} \|u\| u - c(\nabla h \cdot u)\nabla h \quad (2.33)$$

and the continuity equation:

$$\frac{\partial \eta}{\partial t} + \nabla \cdot (Hu) = 0 \quad (2.34)$$

with u the total barotropic current, η is the sea surface elevation, H is the total water depth, h is the mean water depth ($H = \eta + h$), g is the gravitational acceleration, Ω is the Coriolis and metrics contribution, k_2 , l_2 are the potential and deformation Love numbers, Π_a is the astronomical potential, Π_{LSA} is the LSA potential, A is the horizontal momentum diffusion coefficient, C is the quadratic friction coefficient, c is the internal wave drag coefficient.

We can derive the kinetic energy equation by multiplying Equation (2.31) by ρHu and using Equation (2.34):

$$\frac{\partial e_k}{\partial t} + \nabla \cdot e_k u = -\rho g Hu \cdot \nabla \eta + \rho Hu \cdot F + \rho Hu \cdot D \quad (2.35)$$

where e_k is the kinetic energy per surface unit

$$e_k = \frac{1}{2} \rho Hu \cdot u \quad (2.36)$$

The time-averaged energy budget is given by

$$\lim_{T \rightarrow \infty} \frac{1}{T} \int_0^T \nabla(e_k u) dt = \bar{w}_p + \bar{w}_F + \bar{w}_D \quad (2.37)$$

With contributions from pressure gradient, astronomical forcing and dissipation:

$$\begin{aligned} \bar{w}_p &= -\lim_{T \rightarrow \infty} \frac{1}{T} \rho g \int_0^T Hu \cdot \nabla \eta dt \\ \bar{w}_F &= \lim_{T \rightarrow \infty} \frac{1}{T} \rho \int_0^T Hu \cdot F dt \\ \bar{w}_D &= \lim_{T \rightarrow \infty} \frac{1}{T} \rho \int_0^T Hu \cdot D dt \end{aligned} \quad (2.38)$$

Using Green's formula

$$\begin{aligned} Hu \cdot \nabla \eta &= \nabla \cdot (\eta Hu) - \eta \nabla \cdot (Hu) \\ &= \nabla \cdot (\eta Hu) + \eta \frac{\partial \eta}{\partial t} \\ &= \nabla \cdot (\eta Hu) + \frac{1}{2} \frac{\partial^2 \eta}{\partial t} \end{aligned} \quad (2.39)$$

When integrating Equation (2.39) over a given domain, it is transformed into a flux integral:

$$-\rho g \int_{\Omega} Hu \cdot \nabla \eta ds = -\rho g \left(\frac{1}{2} \int_{\Omega} \frac{\partial \eta^2}{\partial t} ds + \int_{\Gamma} \eta Hu \cdot n dl \right) \quad (2.40)$$

where $\rho g \eta Hu \cdot n$ is called **energy flux**.

The time-averaged domain-integrated energy equation can be expressed as follows:

$$\lim_{T \rightarrow \infty} \frac{1}{T} \int_0^T \int_{\Gamma} (e_k + \rho g \eta H) u \cdot n dl = \int_{\Omega} \bar{w}_F ds + \int_{\Omega} \bar{w}_D ds \quad (2.41)$$

The mean kinetic energy per surface unit is defined as

$$\bar{e}_k = \lim_{T \rightarrow \infty} \frac{1}{T} \int_0^T e_k dt = \lim_{T \rightarrow \infty} \rho h \frac{1}{T} \int_0^T (u \cdot u) dt + \lim_{T \rightarrow \infty} \rho \frac{1}{T} \int_0^T (\eta u \cdot u) dt \quad (2.42)$$

Assuming that the model elevation and both velocity components take the following form:

$$\alpha(\lambda, \phi, t) = \sum_i \hat{\alpha}_i(\lambda, \phi) \cos(\omega_i t + V_o - G_{\alpha,i}(\lambda, \phi)) \quad (2.43)$$

where the subscript i stands for the tidal component index. Equation (2.42) becomes:

$$\bar{e}_k \approx \rho h \frac{1}{4} \sum (\hat{u}_i \cdot \hat{u}_i) \quad (2.44)$$

where \hat{u}_i is the amplitude of the complex velocity.

The total mean kinetic energy can be approximated by the summation of the mean kinetic energy specific to each tidal constituent. Similar considerations can be applied to the various contributions to the mean energy budget. Multiply Equation (2.31) by $\rho g h u_i$, averaging in time lead to the spectral energy equation:

$$\rho h \lim_{T \rightarrow \infty} \frac{1}{T} \int_0^T (u \cdot \nabla u) \cdot u_i dt = \rho h \frac{1}{T_i} \int_0^{T_i} (u \cdot \nabla u)_i u_i dt = \bar{w}_{P,i} + \bar{w}_{F,i} + \bar{w}_{D,i} \quad (2.45)$$

where

$$\bar{w}_{P,i} = \underbrace{-\rho g h \frac{1}{T_i} \int_0^{T_i} u_i \cdot \nabla \eta_i dt}_{\text{surface pressure}} \quad (2.46)$$

$$\bar{w}_{F,i} = \underbrace{\rho g h \frac{1}{T_i} \int_0^{T_i} u_i \cdot \nabla \Pi_i dt}_{\text{tidal forcing}} \quad (2.47)$$

$$\bar{w}_{D,i} = \underbrace{-\rho c h \frac{1}{T_i} \int_0^{T_i} (\nabla h \cdot u_i)^2 dt}_{\text{wave drag}} + \underbrace{\rho h \frac{1}{T_i} \int_0^{T_i} u_i \cdot (A \nabla u)_i dt}_{\text{horizontal diffusivity}} - \underbrace{\rho C h \frac{1}{T_i} \int_0^{T_i} u_i \cdot \left(\frac{\|u\| u}{H} \right)_i dt}_{\text{bottom friction}} \quad (2.48)$$

The spectral mean energy flux of a given tidal constituent is defined as:

$$\bar{\phi}_i = \rho g \frac{1}{T_i} \int_0^{T_i} \int_{\Gamma} \eta_i h u_i \cdot n dl \quad (2.49)$$

Integrating over the domain the spectral mean energy flux is:

$$\sum_i \bar{\phi}_i = \sum_i \left(\rho g h \frac{1}{T_i} \int_0^{T_i} \int_{\Omega} \eta_i \nabla \cdot (\eta_j u_k) ds dt \right) - \rho g \sum_{i,j,k} \lim_{T \rightarrow \infty} \frac{1}{T} \int_0^T \int_{\Omega} \eta_i \nabla \cdot (\eta_j u_k) ds dt \quad (2.50)$$

Chapter 3: Model validation and sensitivity analysis in the Gulf of Tonkin

To improve our understanding of the mechanisms that cause the transport of sediments in the Gulf of Tonkin, it is essential to better understand the role of tides in the Gulf. The aim of this chapter is to validate and calibrate the application of ROMS to the Gulf of Tonkin. Validation is a continuous process during the entire course of a modeling project. It involves the verification of model results with measurements, explanation of the differences and conclusions on the model performances. Validation also includes sensitivity analysis, which consists of systematic variation of model parameters and comparison of model simulations. During calibration the comparison between measurements and model results are used to improve the model solution for optimal results. There is more than one round of interaction between the processes of validation, sensitivity analysis and calibration but we choose here to present these processes in a linear manner for clarity.

3.1 Previous modeling work

Barotropic tides in the Vietnam East Sea/South China Sea and the Gulf of Tonkin have been studied since the 1940s. A number of numerical models were developed to improve the prediction of tides and tidal currents because we cannot predict any local tides based on rare in-situ observations. Some of the numerical tidal models are two-dimensional. Of particular interest, Fang et al. (1999) successfully simulated M2, S2, K1 and O1 simultaneously using a two-dimensional (depth-integrated) shallow water model and applied prescribed boundary conditions to the elevation field from limited tidal observations. He used the frictional parameter value $C_D=0.002$ (quadratic bottom friction formulation). More recently, three-dimensional tidal models were applied (e.g., Cai et al., 2005; Zu et al., 2008; Chen et al., 2009). Cai et al. (2005) used a three-dimensional approach to evaluate the accuracy of predicted tidal harmonic constants under various conditions. He used several numerical experiments involving two- or three-dimensional simulations, astronomical tidal forcing and surface winds. The horizontal resolution was about 10 km and the water column was divided into 13 levels. A quadratic law was used for computation of bottom friction ($C_D=0.002$ again). Relatively short 30-day time series of hourly surface elevation were used to yield harmonic constants by conventional tidal harmonic analysis (a process known as “de-tiding”). The results show that the tidal predictions of the three-dimensional model are more realistic than those of the two-dimensional model. In addition, wind-driven currents are shown to be strong in the Gulf of Tonkin and should be included when addressing transport properties. Our model configuration therefore combines all realistic forcing but with higher resolution and longer time integration for more accurate de-tiding. A particular attention is also given here to cross-examination of tidal harmonic constants between model and data.

3.2 Model setup

The domain should be larger than the region of interest (within the geographical boundaries of Vietnam) to avoid setting open boundaries in sensitive areas such as Hainan Strait. The model is implemented in a domain that extends in longitudes from 105.5°E to 113.5°E and in latitudes from 15°N to 23°N. The open boundaries lie almost entirely in deep water well away from the continental shelf and slope. It is highly advantageous to specify boundary conditions in deep water as nonlinear constituents are small and global tidal models tend to be more accurate. The model was run for one year starting on January 1st 2004, with a baroclinic time step of 120s. Output files were written into every model hour.

3.2.1 Grid generation

We use ROMSTOOLS for creating grids (Penven et al., 2008). ROMSTOOLS generates rectangular Mercator grids with bathymetry and land masking fields. Bathymetry data was derived from the GEBCO_08 (30 arc-second) gridded dataset (General Bathymetric Chart of the Oceans). GEBCO operates under the joint auspices of the Intergovernmental Oceanographic Commission (IOC) (of UNESCO) and the International Hydrographic Organization (IHO). GEBCO_08 bathymetry (released in October 2010) is a combination of Smith and Sandwell global topographic grid (version 11.1, September, 2008) with a database of over 290 million bathymetric soundings (User Guide to the GEBCO_08 Grid). We chose for ROMS grid a horizontal resolution of $1/25^\circ \times 1/25^\circ$ (4.5x4.5km) with 20 terrain-following sigma coordinate levels. The bathymetric data was linearly interpolated on this grid and a minimum depth was set to 10 m. An iterative averaging procedure is applied to prevent under-sampling. To prevent pressure gradient errors, h (depth) is smoothed selectively so as to reduce the “slope parameter” $r = |h_{+1/2} - h_{-1/2}| / |h_{+1/2} + h_{-1/2}| \sim \Delta h / 2h$. A modified Shapiro smoother is applied iteratively on $\log(h)$ until r is below the required value, generally 0.25 (Penven et al., 2008). This selective filtering, added to preliminary grid averaging (to avoid aliasing), has its largest effect on the continental slope (deep and steep) but also has some effect on the bathymetry of Paracel Islands, the Southeast Hainan Island and the Hainan strait, which may vary by a few meters after smoothing.

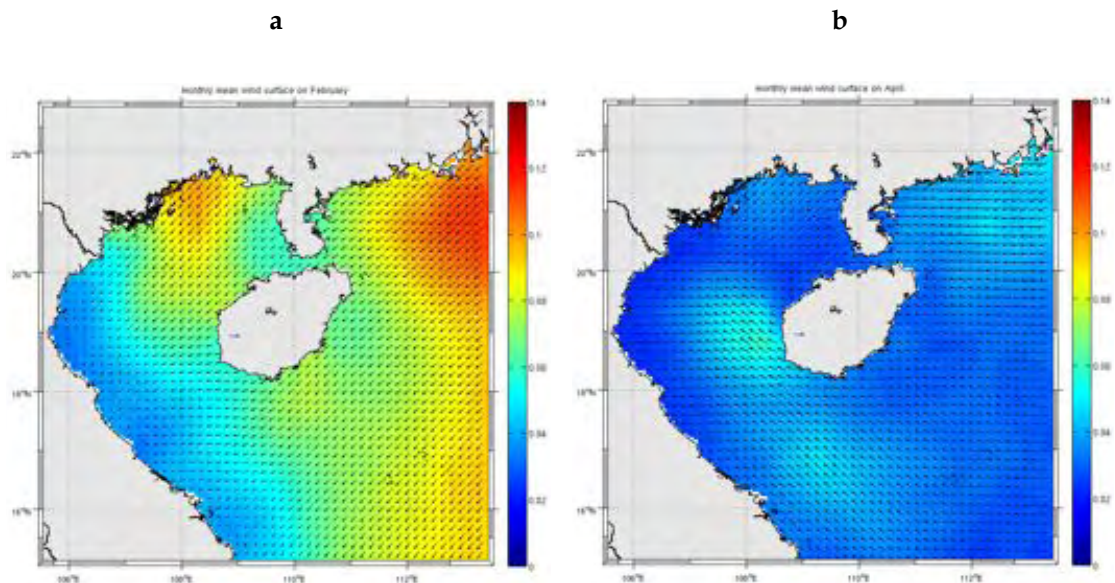
3.2.2 Surface fluxes

We only use climatological surface fluxes in this study, neglecting the effect of interannual and intra-seasonal forcing. We did not include river runoff either, relying instead on surface temperature/salinity relaxation to climatology to maintain the mean properties. The use of climatological forcing is justified here because of our focus on tidal dynamics. It is included to provide a simple mean of comparison between wind- and density-driven currents and tidal residuals.

The atmospheric buoyancy forcing fields, heat and freshwater fluxes, are based on monthly climatology of the Comprehensive Ocean Atmosphere Data Set (COADS; Da Silva et al., 1994). This 0.5°-resolution gridded climatology is composed of air-sea parameters derived from individual observations. Missing values are replaced

by objective analysis. The resulting matrices are interpolated using a cubic method. The model sea surface temperature (SST) feedback on the heat flux is represented as a correction towards SST climatology (Barnier et al., 1995). We used for SST the Pathfinder monthly climatology at ~ 10 km resolution derived from AVHRR observations from 1985 to 1997 (Casey and Cornillon, 1999). A similar correction is used for the fresh water flux.

Wind forcing in the model is interpolated from climatology of QuikSCAT satellite scatterometer. The QuikSCAT monthly climatology was computed from the CERSAT gridded data (0.5° resolution) provided from Oct 1999 to Aug 2006. The wind stress derived from QuikSCAT is presented in Figure 3.1 for a brief characterization of wind conditions in the Gulf of Tonkin. The year-mean wind stress is about 0.03 N/m^2 except in winter, where the average wind stress is about 0.09 N/m^2 with a main northeast direction. The wind is from East/Southeast in spring and South/Southwest in summer.



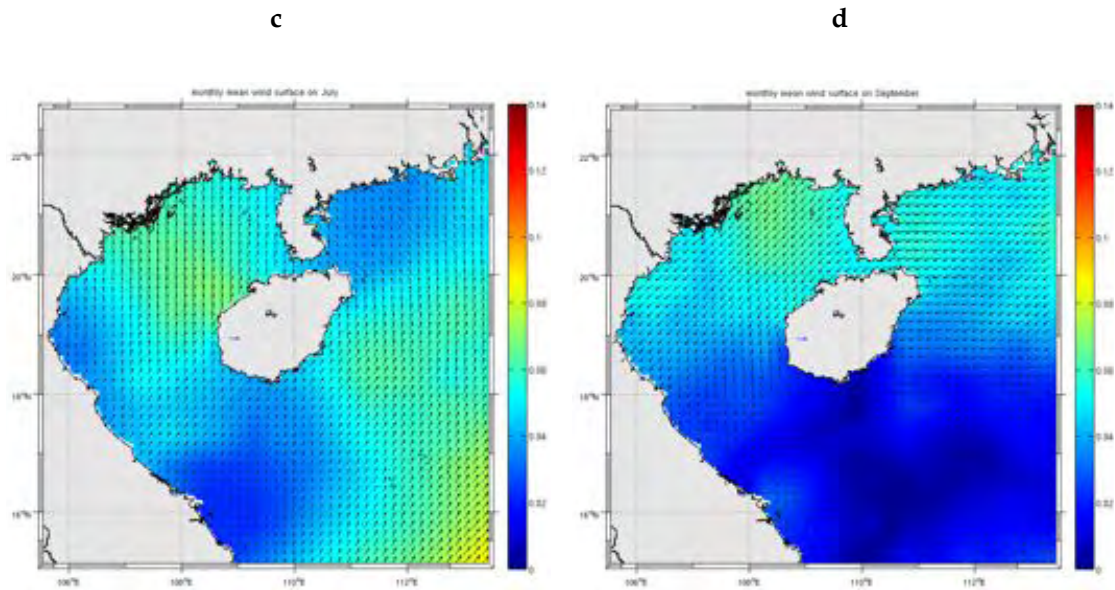


Figure 3.1: Monthly mean wind stress based on the QuikSCAT monthly climatology with magnitude in shaded background for (a) February: northeast monsoon, (b) April, (c) August, and (d) September. (1 vector is portrayed every 4 model grid points). The color range represents the wind stress in N/m^2 . Vector reference: 0.1 N/m^2 .

Heat fluxes are large in the tropical region. The net heat flux at the surface of the ocean is the sum of shortwave radiation (direct solar radiation), long wave radiation (radiated upward by the ocean surface and downward by air and clouds), sensible heat flux (due to turbulent exchange at the interface) and latent heat flux (due to evaporation). Negative values represent heat lost by the ocean surface (cooling), positive values represent heat gain (warming). Figure 3.2 shows the monthly mean net surface heat flux during the four seasons. In winter, the Gulf of Tonkin loses heat into the atmosphere (negative values). The largest latent heat loss occurs during this season with a cooling rate of about -170 W/m^2 in December and January. It is largely due to weaker solar heating and also to evaporative cooling due to strong cold and dry northeast winds. The largest heat gain occurs during June and July. The months of September-October appear as a transitional period in the Gulf of Tonkin. The general pattern of net heat flux over the study area shows that the Gulf of Tonkin gains heat during 7 months (from March to September).

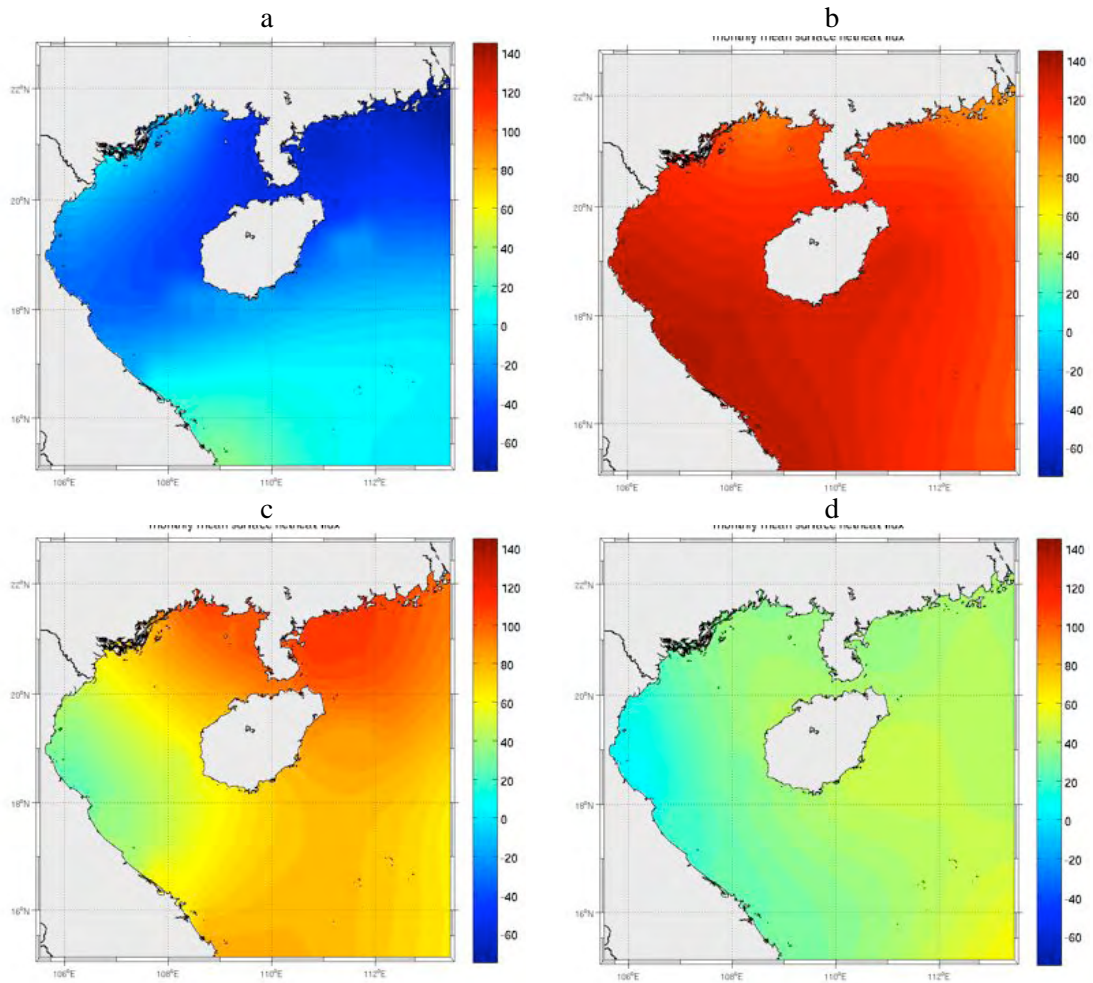


Figure 3.2: Monthly mean net surface heat flux based on COADS monthly climatology in $W.m^{-2}$ for (a) February, (b) April, (c) August, and (d) September.

Surface temperature in summer (August – Figure 3.3c) is nearly homogeneous (about $29^{\circ}C$) in most part of the Gulf. In winter, surface temperatures are between $23^{\circ}C$ and $25^{\circ}C$ with a meridional gradient.

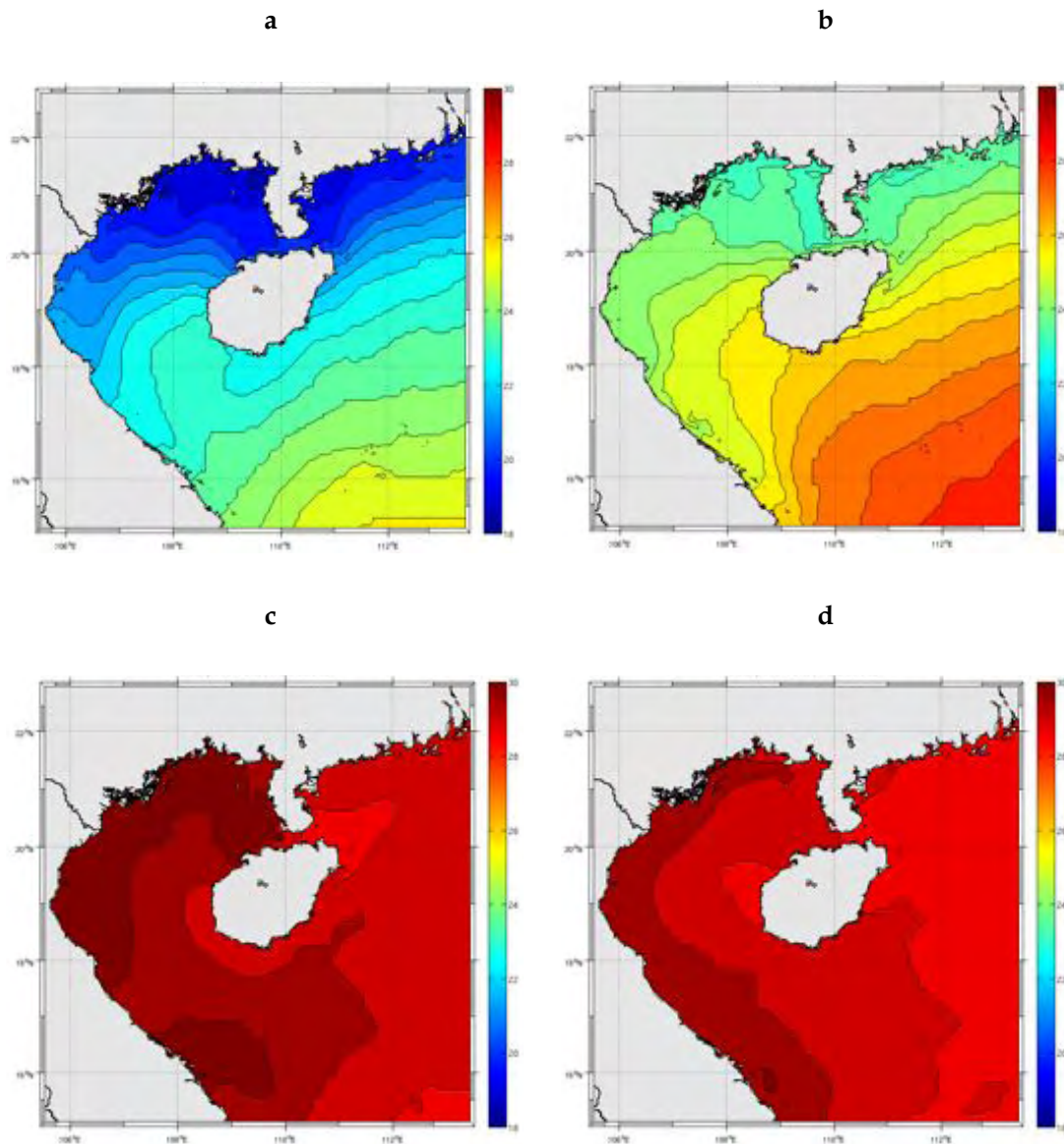


Figure 3.3: Monthly mean surface temperature (°C) based on AVHRR monthly climatology for (a) February, (b) April, (c) August, and (d) September.

Seasonal patterns of freshwater fluxes are presented in Figure 3.4. Fall has the lowest evaporation rate and negative freshwater fluxes due to strong precipitation that occurs in the western part of the Gulf, around latitude 18°N (Figure 3.4d). In summer, the coastal regions show higher evaporation (Figure 3.4c) while the other seasons are intermediate.

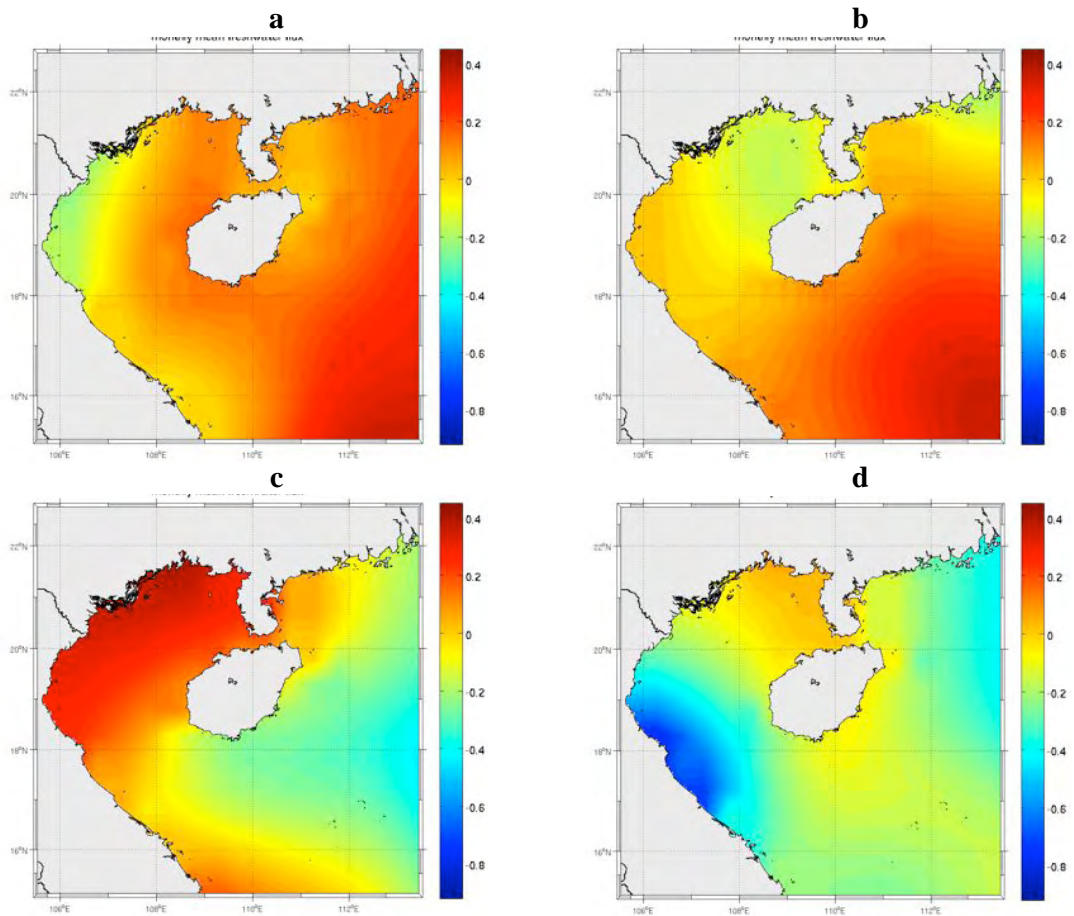


Figure 3.4: Monthly mean evaporation minus precipitation ($\text{cm}\cdot\text{day}^{-1}$) of the COADS monthly climatology for (a) February, (b) April, (c) August, and (d) September.

3.2.3 Initial and boundary conditions

The model was initialized with zero velocity and a flat free surface (the variables u , v , \bar{u} , \bar{v} , ζ are set to zero at $t=0$). The temperature and salinity are from the World Ocean Atlas 2005 (WOA). WOA provides a monthly climatology (1° resolution, 33 vertical levels) of in situ ocean parameters derived from individual observations (Conkright et al., 2002). The resulting matrices are horizontally and, subsequently, vertically interpolated on ROMS terrain-following grid. From temperature and salinity fields, geostrophic currents with a level of no motion defined at 1000 m were computed and used as subtidal oceanic forcing in ROMS open boundary conditions.

8 tidal constituents (O1, K1, M2, S2, N2, K2, P1, Q1; ordered by their amplitudes in the Gulf of Tonkin) for elevation and barotropic flow were interpolated from a global inverse barotropic tidal model (TPXO.7). TPXO.7 has a horizontal resolution of 0.25 degrees and uses an inverse modeling technique to assimilate satellite altimetry cross-over observation (Egbert and Erofeeva, 2002). Tidal phases are adjusted to the chosen period of simulation (year 2004) and both phases and amplitudes are corrected for nodal variations (caused by the 18.6-year cycle of

lunar orbital tilt). High frequency (tidal) barotropic currents and elevations are added to the low frequency (subtidal) boundary forcing using a Flather-type condition (for barotropic flow and elevation) and radiative conditions (for tracers and total flow) on the eastern and southern boundaries (Marchesiello et al., 2001).

3.3 Model validation

Various statistical parameters (metrics) are calculated for data analysis, such as Mean Error (ME), Mean Absolute Error (MAE), Root Mean Square Error (RMSE), which reflect the degree that observations agree with model results. The definitions are given by:

$$\begin{aligned}
 ME &= \frac{1}{N} \sum_{i=1}^N (M_i - O_i) \\
 MAE &= \frac{1}{N} \sum_{i=1}^N |M_i - O_i| \\
 RMSE &= \sqrt{\frac{1}{N} \sum_{i=1}^N (M_i - O_i)^2}
 \end{aligned} \tag{3.1}$$

O_i is the observational data while M_i is the model solution. We also quantify the errors of each tidal constituent by its distance D in the complex plane, following Foreman and Henry (1993). At each station (for each constituent) the error is defined as the magnitude of the observed constituent minus the modeled constituent evaluated in the complex plane:

$$D = \sqrt{(A_o \cos P_o - A_m \cos P_m)^2 + (A_o \sin P_o - A_m \sin P_m)^2} \tag{3.2}$$

A_o , A_m , P_o , P_m are the observed and modeled amplitudes and phases, respectively. D is calculated as vectorial differences. This metric combines both amplitude and phase error into a single error measure. To evaluate the solutions for one constituent over a given area the root-mean-square values over multiple stations were calculated.

To compare the model results with observations, a harmonic analysis using Detidor (see Chapter 2) is applied. The model time series are processed through a least squares analysis to decompose its signal into tidal constituent frequencies. Harmonic analyses of short-term simulations (e.g., 30-days is quite common in the literature) are unsuccessful, largely because of the inability of the method to distinguish between K_2 and S_2 frequencies in the abbreviated time signal. Godin (1972) recommends a time series length greater than 183 days to accurately extract K_2 and S_2 tidal constituents. Table 3.1 presents the model RMS errors versus altimetry data of the amplitude and phase of K_1 , O_1 , M_2 , S_2 averaged over the entire Gulf and retrieved from 1 month, 6 months, and one year of simulation, respectively. It confirms that 6 months of simulation are needed at least for the S_2 signal. This is most obvious in the phase error (divided by 2 when the analysis is

performed over at least 6 months). In the following, we retain the 1-year sampling period for all comparisons with data.

Table 3.1: Model RMS errors (versus altimetry data) of amplitude and phase of 4 tidal constituents: K1, O1, M2, S2. RMSE are averaged over the entire Gulf of Tonkin and presented for different cases of model simulation length.

Tidal component	K1			O1			M2			S2		
	1month	6month	1year	1month	6month	1year	1month	6month	1year	1month	6month	1year
RMSE-amplitude (cm)	3.06	2.88	2.84	1.94	2.41	2.37	6.45	7.93	8.05	4.6	2.48	2.43
RMSE-phase (degree)	10.52	10.15	10.42	8.61	8.46	8.37	6.83	7.71	7.89	33	17.79	17.7

3.3.1 Tidal gauges

A verification of modeled circulation patterns occurring within the Gulf is necessary to investigate the physical processes apparent within the water body. The purpose of this chapter is to test the capability of ROMS in simulating the tides of the Gulf of Tonkin using the best available estimates of tidal harmonic constants. That involves both tidal gauges and satellite altimetry for coastal regions. In this thesis, considerable effort has been devoted to the estimation of model sensitivity in representing the tides. Our reference simulation is performed using configuration E3 (Table 3.4) with a logarithmic evaluation of the quadratic drag coefficient and roughness value $z_0=0.1$ mm. This choice was made from a set of model experiments varying bottom stress formulation and values, two- or three-dimensionality, and spatial resolution, which are presented below.

The analysis is the process of reducing the amount of data to a comprehensible quantity – a harmonic tidal analysis in most cases reduces a long-term, hourly time series (from observation or simulation) to a set of pairs of numbers, the amplitudes and phases of the constituents. This tidal information can be rendered comprehensible by presenting it in co-tidal charts that are contour maps of phase and amplitude of each constituent.

The amplitudes and phases of tidal constituents at 30 stations along the gulf coast, obtained from harmonic analysis of simulated tides, were compared with those of tidal gauge stations reported in Chen et al. (2009). The positions of these stations are shown in Figure 3.5. The mean absolute difference of amplitude (in centimeter) and phase (in degree) of K1, O1, M2, S2 between our reference ROMS simulation and tide gauge data are given in Table 3.2. Our results show a general improvement compared with the errors given in Chen et al. (2009), apart from the amplitude of M2.

Table 3.2: Mean absolute differences of amplitude (in centimeter) and phase (in degree) of K1, O1, M2, S2 constituents between our reference ROMS simulation and tidal gauge data

Tides	K1		O1		M2		S2	
	Amplitude	Phase	Amplitude	Phase	Amplitude	Phase	Amplitude	Phase
ROMS	2.0	2.0	3.7	3.0	8.4	1.0	2.0	11.0
Chen et al. (2009)	5.4	8.9	3.0	9.0	2.3	6.7	2.8	22.0

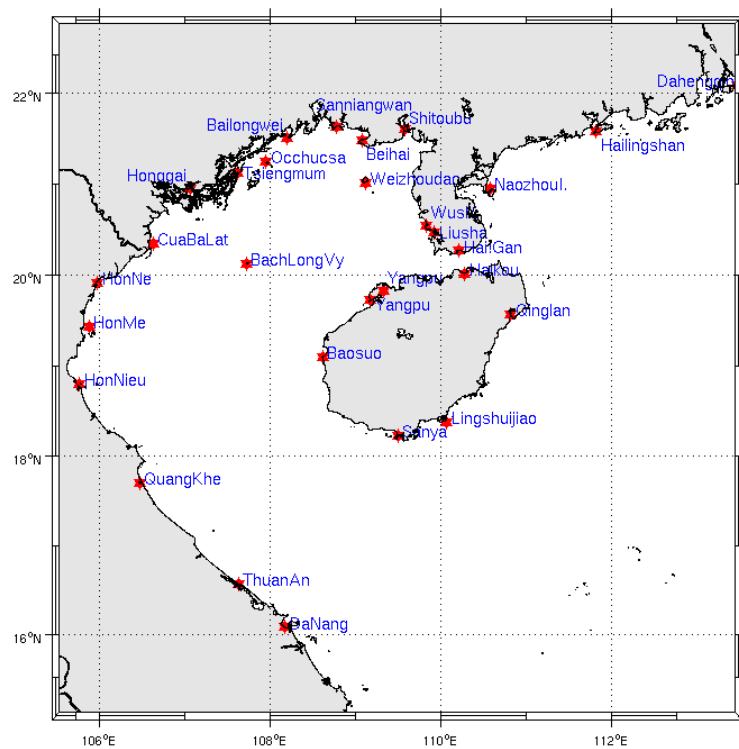
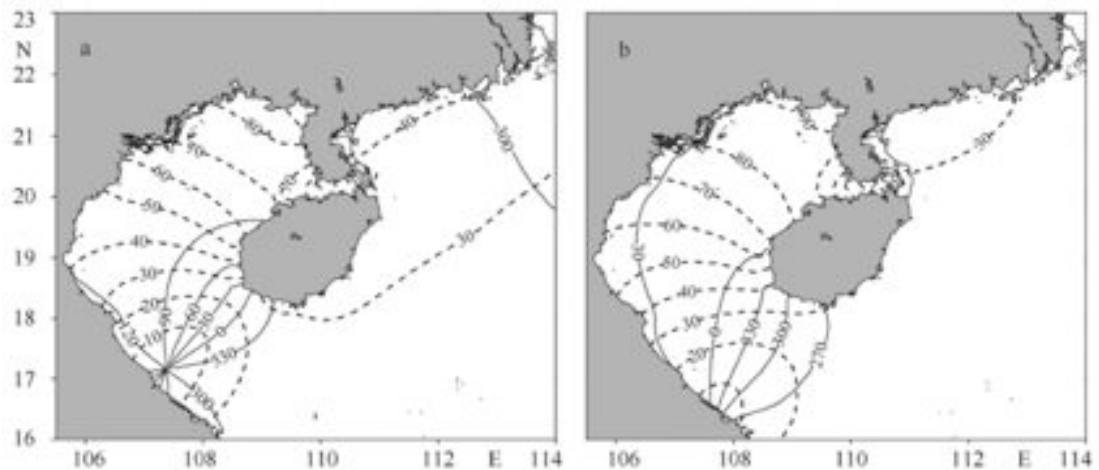


Figure 3.5: Location of the tide gauges

The general spatial patterns of tidal amplitudes simulated by ROMS agree also visually with earlier results by Chen et al. (2009). The amphidromic systems of K1, O1, M2 and S2 as calculated by the model (reference simulation) are shown in Figure 3.6 and 3.7. The term amphidrome refers to elevation nodal points where the amplitude tends to zero. In each amphidromic system, co-tidal lines can be defined which link all the points where the tide is at the same phase of its cycle. The co-tidal lines thus radiate outwards from the amphidromic point. Cutting across co-tidal lines are co-range lines, which join places having an equal tidal range. Co-range lines form more or less concentric circles around the amphidromic point, representing larger tidal ranges further away. The co-tidal

charts for the constituents within each species: diurnal, semidiurnal, etc. are similar because within the species the frequencies are closely spaced, leading to similar ocean responses if the processes governing them are the same. The detailed differences between the charts for constituents within a species contain further information on the fine-tuning of the responses and of the tidal processes. Tides of the diurnal type are predominant in the Gulf of Tonkin. The largest amplitudes, both in the gulf and on the shelf, are in the diurnal species. There is a similarity between the diurnal constituents K1 and O1 in the gulf (Figure 3.6). The significant differences between them occur near amphidromes. At the entrance of the gulf each of K1 and O1 tides has a degenerate amphidromic system centered at the middle Vietnam coast. Degenerate amphidromes are virtual amphidromes located inland (the convergence of co-phase lines is toward an inland point). This can result from frictional losses by the reflected tide in the bay. Here, the O1 system is definitely degenerate but the K1 system is only marginally so, consistent with larger amplitudes and frictional losses for O1. O1 and K1 maximum amplitudes (in excess of 90 and 80 cm respectively) is located at the head of the gulf. The qualitative comparison between ROMS and Chen et al.'s (2009) model results indicates good agreement.



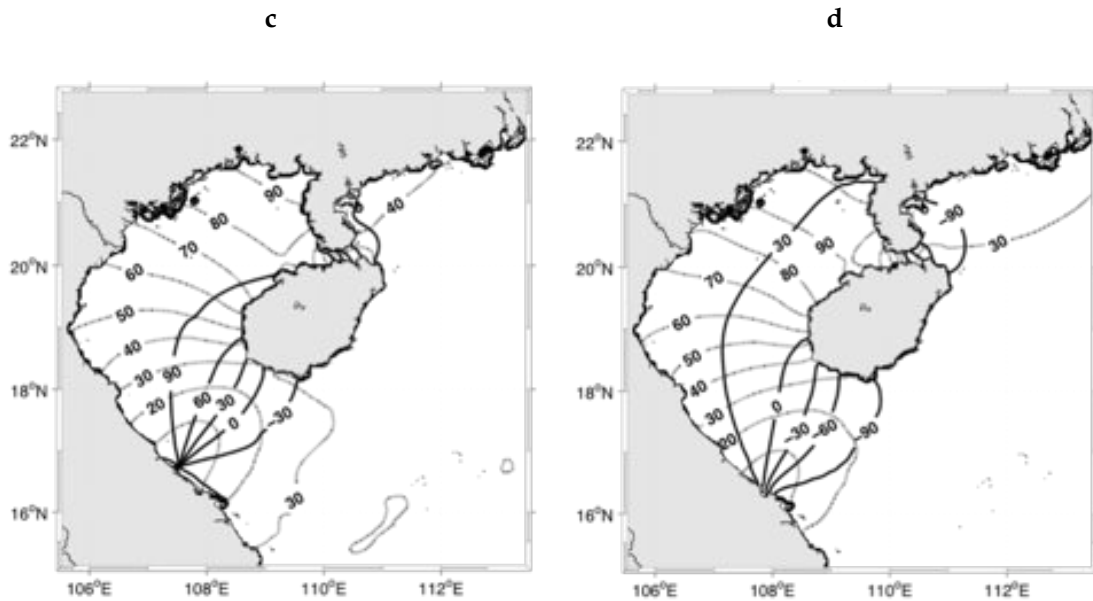
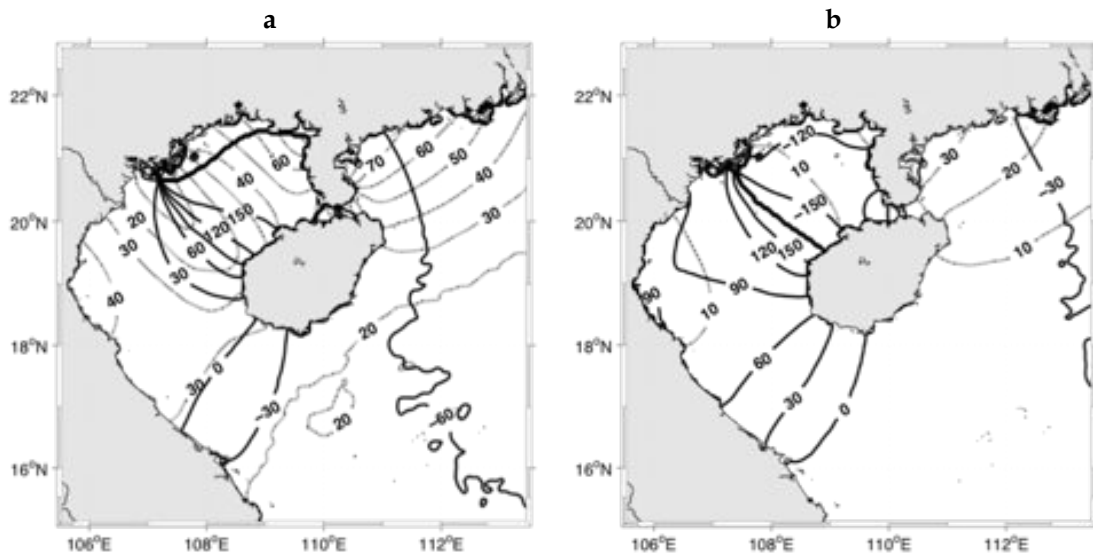


Figure 3.6: ROMS co-tidal charts for the constituent of (c) K1, (d) O1 and their comparison to Chen et al (2009) (a,b) referred to GMT+8. (Solid line: phase-lag in degree, dashed line: amplitude in cm).

In Figure 3.7, the co-tidal lines of M2 and S2 constituents are represented. The large M2 amplitudes occur along the east coast of China (north of Hainan island). In the gulf, the amplitude of this wave is about 40-50 cm, significantly smaller than the amplitude of K1 and O1. A nodal band can be observed in the west coast of Vietnam. The co-tidal lines converge to a degenerate amphidrome near the zone of Ha-Long Bay. The pattern of S2 component is rather similar to that of M2 but the amplitude is less than 10 cm in the Gulf.



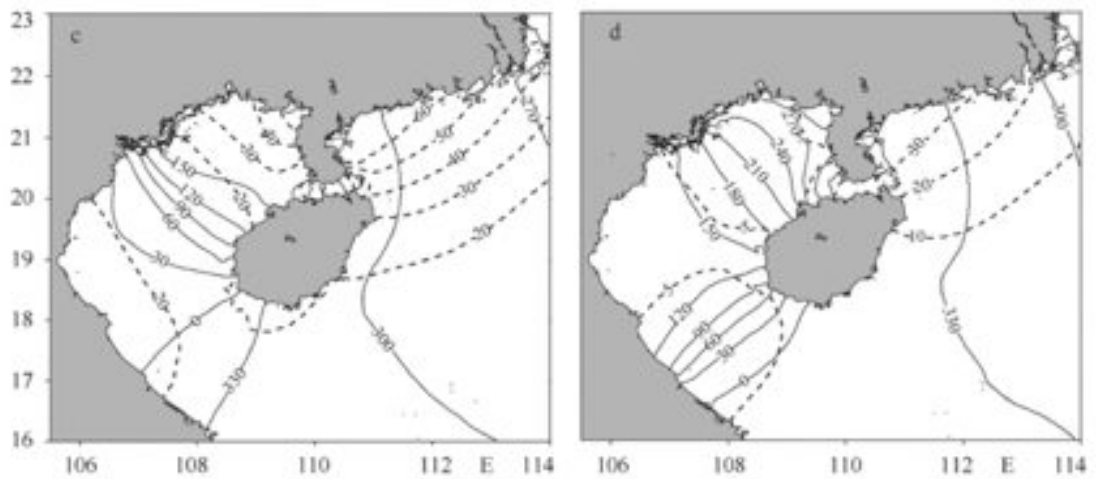


Figure 3.7: ROMS co-tidal charts for the constituent of (a) M2, (b) S2 and their comparison to Chen et al (2009) (c, d) referred to GMT+8. (Solid line: phase-lag in degree, dashed line: amplitude in cm)

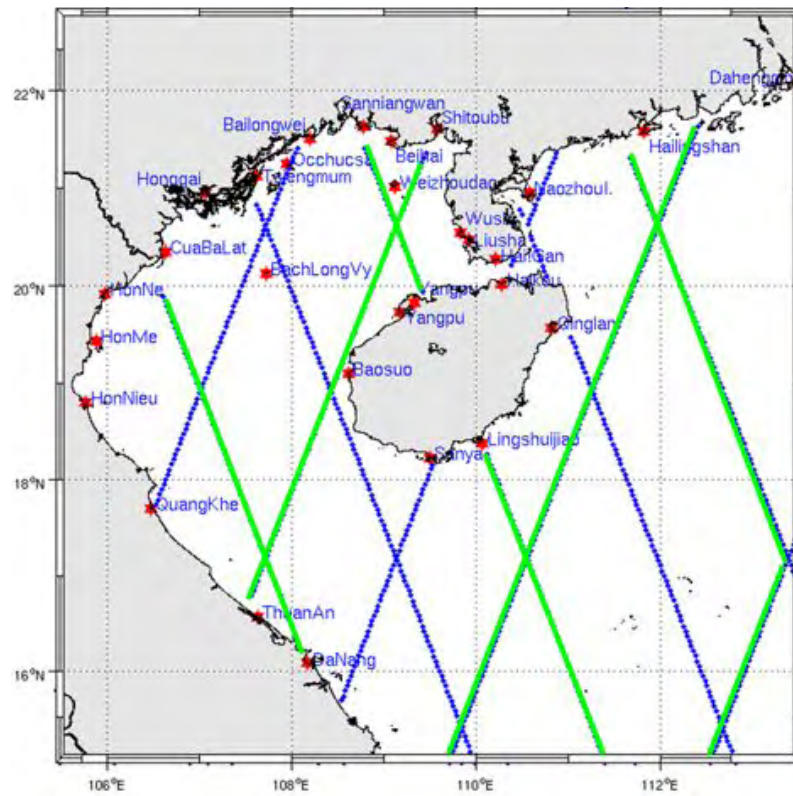


Figure 3.8: Location of tide gauges (red hexagram) and altimeter data (blue dot), the green lines represent interleaved orbit.

3.3.2 Satellite altimetry

Satellite altimetry missions have resulted in great advances in marine research and operational oceanography, providing accurate sea level data (at centimeter error level) and high-value information products (including ocean waves and winds). However, the space-time sampling of current altimeter missions is generally too low to capture the complexity of coastal dynamics. Therefore, while preparing for next generation altimeter missions, researchers have made a substantial effort to optimize for the coastal area the post-processing of current altimeter data.

In this thesis, we applied the product of X-TRACK altimeter data processor developed at CTOH/LEGOS, France (Roblou et al., 2007, Roblou et al., 2011). Tidal harmonic constants (phase and amplitude) for about 5000 locations in the Gulf of Tonkin were computed by the CTOH, in which about 1700 points using coastal altimetry from 16-year-long continuous record of TOPEX/Poseidon and Jason-1 (blue dots in Figure 3.8) (from November 1992 through June 2009) and the rest from TOPEX/Poseidon and Jason-1 interleaved (green lines in Figure 3.8). Topex/Poseidon was launched in 1992 on a referenced orbit, which was assumed by Jason-1 on December 2001. At the end of Jason-1 calibration phase (September 2002), Topex/Poseidon was shifted on a new orbit (same inclination and cycle length, but moved longitudinally), called interleaved orbit midway between its old ground tracks. TOPEX/Poseidon stopped providing science data in October 2005. Similarly, on February 2009, Jason-1 was also shifted on the same Topex/Poseidon interleaved orbit. Therefore, this interleaved mission provides a large number of measurements of the ocean's surface by introducing 5 years of TOPEX-Jason-1 interleaved mission into existing 16 years of primary joint TOPEX and Jason-1 mission time series. The spatial distribution of observation is tripled, particularly in shallow waters.

For the analysis, the study area was divided into 4 zones based on geographical and tidal characteristics: inside (mouth and head area) and outside (coastal and offshore area) of the Gulf of the Tonkin (Figure 3.10). In general, the model comparison with the combined satellite data shows lower RMS errors (i.e., K1 and O1 tidal components; Table 3.3). However, in some instances, larger errors occur (i.e., for M2 amplitude and S2 phase) when using the interleaved data. This can be explained by the expected lower accuracy of interleaved data analysis as shorter time-series are less efficiently separated into tidal constituents. Nevertheless, the combined interleaved altimetry data will be used in the following as it provides unprecedented spatial distribution of observations in the Gulf of Tonkin.

Table 3.3: Model RMS errors (versus altimetry data) of amplitude (in centimeter) and phase (in degree) of 4 tidal constituents: K1, O1, M2, S2. RMSE are averaged over the entire Gulf of Tonkin, Zone 1, 2, 3 & 4. Data 1: 16-year continuous data; Data 2: Data 1 + 5-year interleaved data. Yellow cells highlight cases where Data 2 give lower error values than Data 1 while light blue cells present the opposite.

Tides		K1		O1		M2		S2	
		Amplitude	Phase	Amplitude	Phase	Amplitude	Phase	Amplitude	Phase
Entire	Data 2	2.84	10.42	2.37	8.37	8.06	7.83	2.44	17.74
	Data 1	3.23	10	3	11.5	6.84	10.52	2.88	16.34
Zone 1	Data 2	4.42	3.16	4.27	2.44	15.23	13.38	3.79	41.4
	Data 1	4.85	3.64	4.53	1.68	6.36	18.39	2.24	38.5
Zone 2	Data 2	5.47	17.72	3.89	21.2	13.38	11.44	5.27	17.2
	Data 1	7.38	26.4	6.12	32	13.18	17.44	7.25	25.3
Zone 3	Data 2	1.84	4	1.17	2.90	9.11	8.94	1.14	10.17
	Data 1	0.62	3.13	1.11	2.13	2.05	4.75	0.64	5
Zone 4	Data 2	2.15	12.32	1.77	6.03	4.4	2.09	1.54	11.34
	Data 1	1.59	4.68	2.19	2.74	6.82	9.7	1.7	7.33

The RMS errors of amplitude and phase between model and observations are represented in Figure 3.9 by the radius of black circles drawn at each measurement point and for each tidal constituent K1, O1, M2 and S2. These results indicate a tendency for larger errors in shallow regions. High error values are particularly visible at the eastern Hainan strait, and in the northeast of Ha-Long bay. In deep water, there is good agreement with altimeter data (RMSE for depth > 100m: [2 cm, 4°] for K1; [1 cm, 3°] for O1). Small RMS errors and relative errors (see detail in Appendix) along oceanic boundaries suggest that open boundary conditions are properly set in the model. The increase of error near the coast may be due to either erroneous altimeter data (land contamination in the altimeter footprint) or/and to model errors associated with coastal bathymetry whose accuracy is crucial to shallow water tidal waves (subject to nonlinear interactions). The same remark is true for bottom friction (see sensitivity tests below). Note that in areas where tidal features are complex, with densely distributed co-tidal lines and variable co-range lines, the model's performances are weaker than in other areas. Insufficient model resolution over these areas is thus another cause of error.

The differences are larger for semi-diurnal components M2 and S2. According to Lyard (personal communication), a compound tide may result from the interaction of diurnal components K1 and O1 with a frequency close to the semi-diurnal tides. It would take at least 18 years of sea level data to separate accurately these components. One-year analysis would be too short and that may be one reason for the discrepancies between model and data on these semi-diurnal constituents.

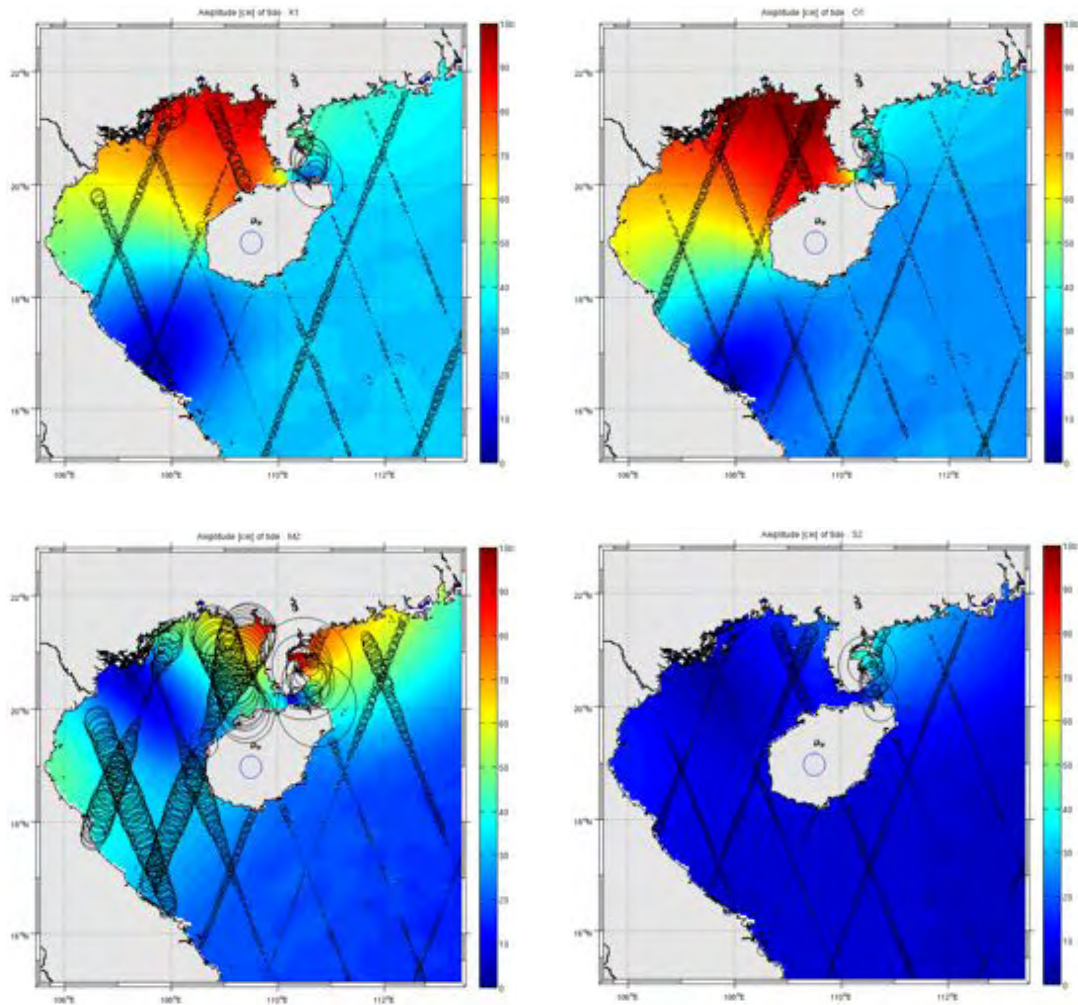
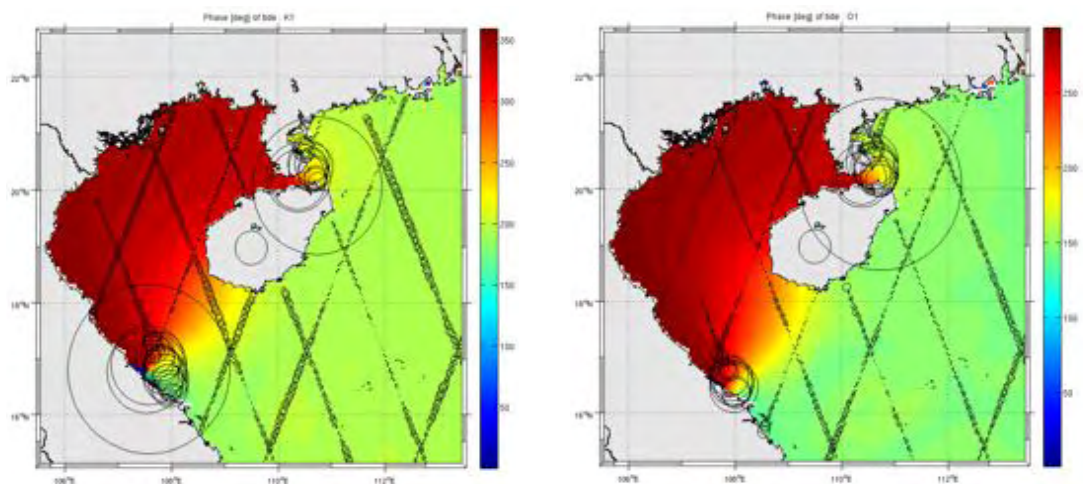


Figure 3.9 -1st part- Tidal misfits in the Gulf of Tonkin for K1, O1, M2, and S2 constituents: background charts represent the model tidal amplitude in centimeter. The size of black circles is proportional to the RMS error of amplitude between ROMS solution and altimeter data. Reference: 10 cm.



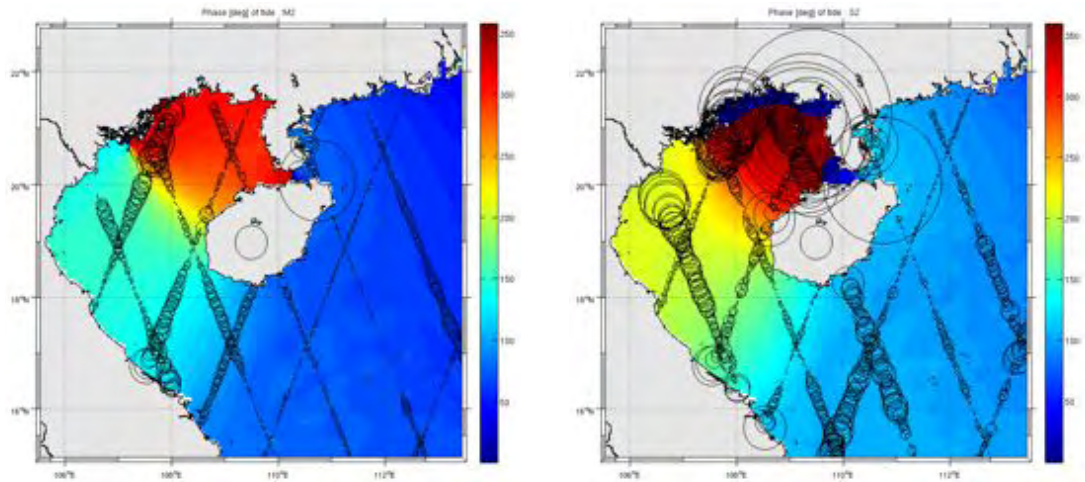


Figure 3.9 -2nd part- Tidal misfits in the Gulf of Tonkin for K1, O1, M2, and S2 constituents: background charts represent the model tidal phase in degree. The size of black circles is proportional to the RMS error of phase between ROMS solution and the altimeter data. Reference: 30 degrees.

3.4 Model sensitivity

The Gulf of Tonkin is a shallow-water body with a strong, resonant tidal signal. It is of interest to check the sensitivity of our results, particularly with respect to resolution and to various bottom stress formulations: linear and quadratic drag laws, with constant drag coefficient or derived from the logarithmic law of the wall. The model configuration is the same for all experiments (parameters, forcing...) unless specified otherwise so that comparisons between simulations are possible. The harmonic constants of K1 and O1 constituents from these simulations are compared with altimetry data.

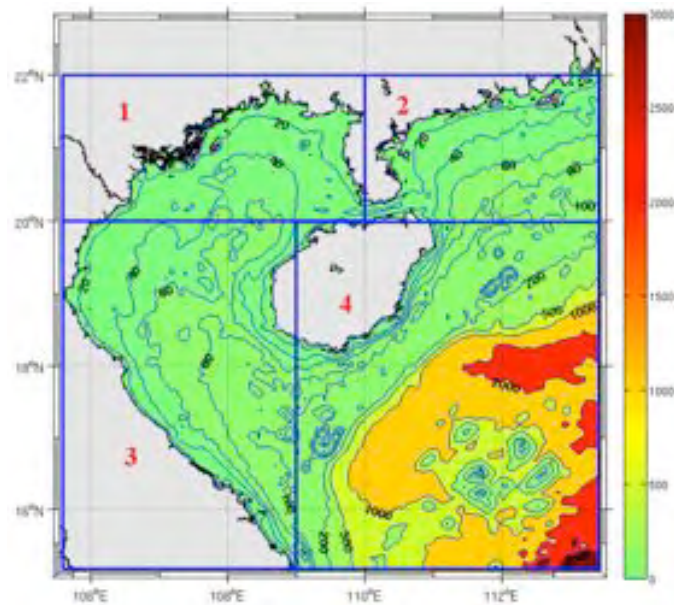


Figure 3.10: The study area is divided into 4 zones; the background chart represents the isobaths in meter from GEBCO_08.

Table 3.4 presents the model RMS errors of K1 and O1 in complex plane when compared with satellite altimetry or with the 30 tidal gauges reported earlier. 3 types of bottom friction formulation are tested: linear or quadratic bottom drag coefficient, with constant or logarithmic formulation via bottom roughness. For testing vertical dimensions (2D or 3D modes) and horizontal resolution ($1/25^\circ$ or $1/30^\circ$), the optimal value of each drag formulation is retained: $r=0.8$ mm/s for linear law, $C_D=0.001$ for quadratic law and $z_o=0.1$ mm for logarithmic profile.

Table 3.4. List of the numerical experiments

N°	Resolution	Dimension	Formulation	Coefficient / z_{ob}	Constituent	RMS errors (cm)	
						Altimetry	Tide gauges
E1	1/25 degree	2	Linear	0.8 mm/s	K1	4.17	5.91
					O1	5.29	8.87
E2	1/25 degree	2	Quadratic	0.001	K1	3.49	5.14
					O1	4.20	7.38
E3	1/25 degree	3	Logarithmic	0.1 mm	K1	2.81	3.83
					O1	3.26	4.64
E4	1/25 degree	3	Linear	0.8 mm/s	K1	4.60	7.10
					O1	5.45	9.80
E5	1/25 degree	3	Quadratic	0.001	K1	4.57	6.93
					O1	5.29	9.44
E6	1/30 degree	2	Linear	0.8 mm/s	K1	4.06	6.38
					O1	5.29	8.95
E7	1/30 degree	2	Quadratic	0.001	K1	4.23	7.79
					O1	4.06	6.72
E8	1/30 degree	3	Logarithmic	0.1 mm	K1	2.58	4.36
					O1	3.30	5.06

3.4.1 Sensitivity to bottom stress formulation

The mean (wave-averaged) bottom stress is an important component of nearshore circulation and sediment transport dynamics. In circulation models, the mean alongshore bottom stress is written as:

$$\tau_b = \rho u_*^2 = \rho C_D u_b^2 \quad (3.3)$$

where ρ is the water density and u_* is the friction velocity, u_b is the near-bottom current. C_D is a non-dimensional bottom drag coefficient. For depth-averaged models, bottom stress can also be formulated as:

$$\tau_b = \rho u_*^2 = \rho r \bar{u} \quad (3.4)$$

where \bar{u} is the depth-averaged current and r is a resistance coefficient with velocity units. The same linear drag law can be used in 3D models, replacing \bar{u} with u_b . C_D depends on the turbulence, and for constant near bottom velocity, C_D increases with increased turbulence levels (due to shear flow or surface wave breaking in very shallow waters). For simplicity, many nearshore circulation models have assumed a spatially constant drag coefficient with the value of C_D usually determined by fitting to observations. This is also the choice we made here, using as a complement the law of the wall (for 3D simulations) to infer C_D from a roughness length-scale z_o :

$$C_D = (\kappa / \ln(z_b / z_o))^2 \quad (3.5)$$

Here, $\kappa = 0.41$ is the Von Karman constant and z_b is the reference height in the logarithmic layer above the bottom, where u_b is computed. This law ensures that

the bottom drag estimation is independent of z_b (in the logarithmic law assumption), which is useful in 3D models with terrain-following coordinates that have variable vertical grids.

Depth-averaged (2D) equations with quadratic bottom stress represent the most common assumptions in global tidal models. These models are easy to implement and can predict the tidal surface elevation accurately at low computational cost. However, these advantages are potentially overshadowed by an oversimplification of the physics. For example, in a shear flow with zero depth-averaged flow, the quadratic drag law would predict no bottom friction even though there should be one (associated with the bottom current). In addition, the direction of bottom stress is not that of the depth-averaged flow since Coriolis acceleration causes the flow to rotate with depth. Note that linear formulations are often considered less physically meaningful than quadratic laws but there are instances where a linear law can be realistic (e.g., slippery bottom flow due to the presence of very fine sediments). We will investigate the linear and quadratic drag law in 3D configurations in section 3.4.3.

In this section, an evaluation of various bottom friction parameterizations is presented. For simplicity and saving computational time, only K1 and O1 tidal constituents are considered since they are the dominant contributors to the Gulf of Tonkin tidal surface elevation. To determine the model's performance and response to the various bottom friction parameters, some simulations were made with the most widely used parameter settings (default values in ROMS): $r=1 \text{ mm}\cdot\text{s}^{-1}$ for linear drag, $C_D=0.0025$ for constant quadratic coefficient and $z_o=1 \text{ mm}$ for logarithmic law.

Influence of the linear bottom friction coefficient

Seven numerical experiments were conducted to explore the effect of the linear bottom friction coefficient, this parameter varying from 0.4 to 2 mm/s. The model is highly sensitive to the linear bottom friction coefficient. The use of a relative small drag coefficient $r = 0.8 \text{ mm/s}$ gave the smallest errors (Figure 3.11a). This is consistent with the presence of fine sediments yielding small bed roughness and thus favoring a deep viscous sublayer with linear velocity profile below the logarithmic profile.

Influence of the quadratic bottom friction coefficient

To investigate the sensitivity of bottom friction coefficient using quadratic bottom drag formula, six numerical simulations were made with C_D varying from 0.0005 to 0.0025. The maximum value here corresponds to what is generally considered a typical value in the world coastal ocean (Arbic et al, 2008). A similar value: $C_D=0.002$ is commonly used in tidal modeling of the Vietnam East Sea/South China Sea that includes the Gulf of Tonkin (Fang et al., 1999; Cai et al., 2005). Figure 3.11b shows the effect of varying C_D on model RMS error for the two major tidal constituents of the Gulf of Tonkin. These errors reach a minimum when the bottom friction coefficient is in the range of 0.001-0.0015, i.e. lower than those chosen for the wider Vietnam East Sea/South China Sea.

Influence of the bottom roughness length

Eleven simulations with z_0 between 0.005 mm and 2.5 mm were carried out to investigate the model sensitivity to bottom roughness length. The RMS errors are less sensitive in the parameter range between 0.05 and 0.2 mm (Figure 3.11c). The value $z_0 = 0.1$ mm appears to yield the minimum errors and is chosen for all later simulations. Again, this is a small roughness length indicating a relatively smooth and firm bed. However, this is a statistical result that can be locally wrong and does not reflect the heterogeneity of the basin.

Comparison between friction laws

We obtain the best model-data fit using a small quadratic drag coefficient obeying the logarithmic law. In the constant coefficient case, the optimal value $C_D=0.001$ has 8% larger error (6.5 cm for the sum of errors) than the logarithmic profile case with $z_0=0.1$ mm (6.1 cm). The logarithmic law takes slightly more computational time but ensures that bottom friction be independent of vertical resolution near the bottom and thus offers more robust results. It is retained in the following.

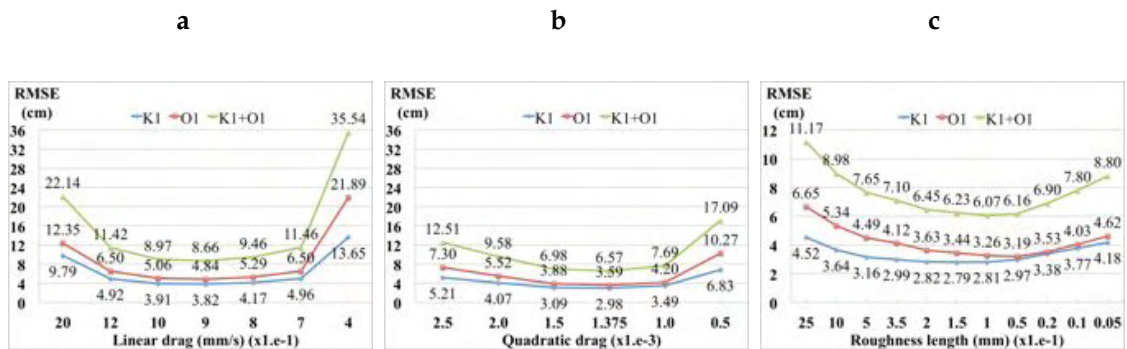


Figure 3.11: RMS errors of D (in the complex plan) for K1 (blue line), O1 (red line) and their sum (green line) for various bottom drag coefficients: (a) linear formulation: r in m/s; (b) quadratic formulation: C_D non-dimensional parameter; (c) logarithmic law: z_0 in mm. Notice that the logarithmic graph is in a different scale.

3.4.2 Sensitivity to the horizontal resolution

The model RMS errors for two different resolutions ($1/30^\circ$ and $1/25^\circ$) for K1 and O1 are given with respect to satellite altimetry and tidal gauges. In general, the higher-resolution solution is slightly more realistic. It tends to improve K1 and O1 components with all bottom stress formulations: linear, quadratic or logarithmic, particularly in zone 2 (Figure 3.12). Increasing horizontal resolution leads to improvements in areas with densely distributed co-tidal lines and variable co-range lines, confirming our previous suggestions. For completeness, this experiment should be continued with much higher resolution in future work.

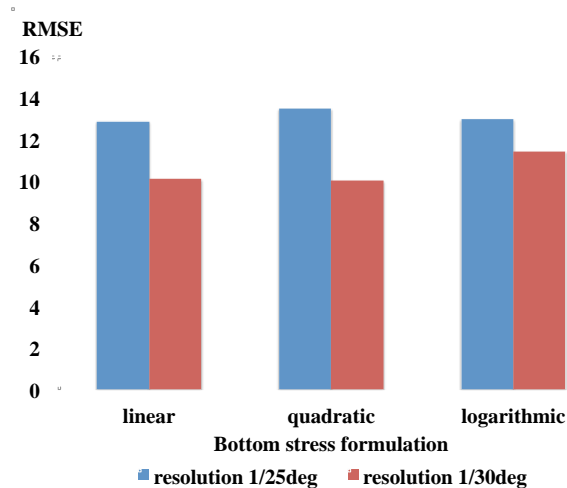


Figure 3.12: RMS errors of D for sum of K1 and O1 solutions at resolutions $1/25^\circ$ (blue column), and $1/30^\circ$ (red column) for various bottom drag coefficients: linear formulation, quadratic formulation and logarithmic law.

3.4.3 Comparison of two- and three-dimensional model solutions

The primary goal of this section is to determine whether differences in the specification of bottom friction in two- or three-dimensional solutions would affect the model results. Bottom friction for the two-dimensional model is parameterized as a function of the vertically averaged velocity, while for the three-dimensional model bottom stress is a function of velocity in the first point above bottom level (assumed in the logarithmic layer). A two-dimensional model is a cheaper option and may be suitable for specific objectives. However, observed sea surface elevation time series from altimeter and tide gauges, which are used to extract harmonic constants, are generally affected by three-dimensionality (as well as atmospheric forcing whose effects we hope to filter out in the data processing). Near-bottom tidal velocity may differ from the depth-averaged velocity in both magnitude and direction.

To test whether tri-dimensionality is critical to modeling tidal elevations in the Gulf of Tonkin, the best bottom friction coefficient for each formulation (linear or constant quadratic) in two-dimensional simulations was used in three-dimensional simulations (Figure 3.13). Interestingly, the errors in 3D solutions are higher than in 2D solutions, the largest difference occurring in Zone 1 (shallow water). This result is in apparent contradiction with our previous comparisons (see sensitivity to drag coefficient), which showed the least model errors obtained using the 3D model with logarithmic drag coefficient. It suggests that the logarithmic profile of C_D has a crucial role as it guarantees that bottom friction is independent of vertical resolution. Decreasing the constant friction coefficient in 3D simulations tends to lower amplitude errors but on the other hand it tends to increase phase errors for both K1 and O1. We could not find an optimal linear or quadratic drag coefficient for 3D solutions that outperform 2D solutions.

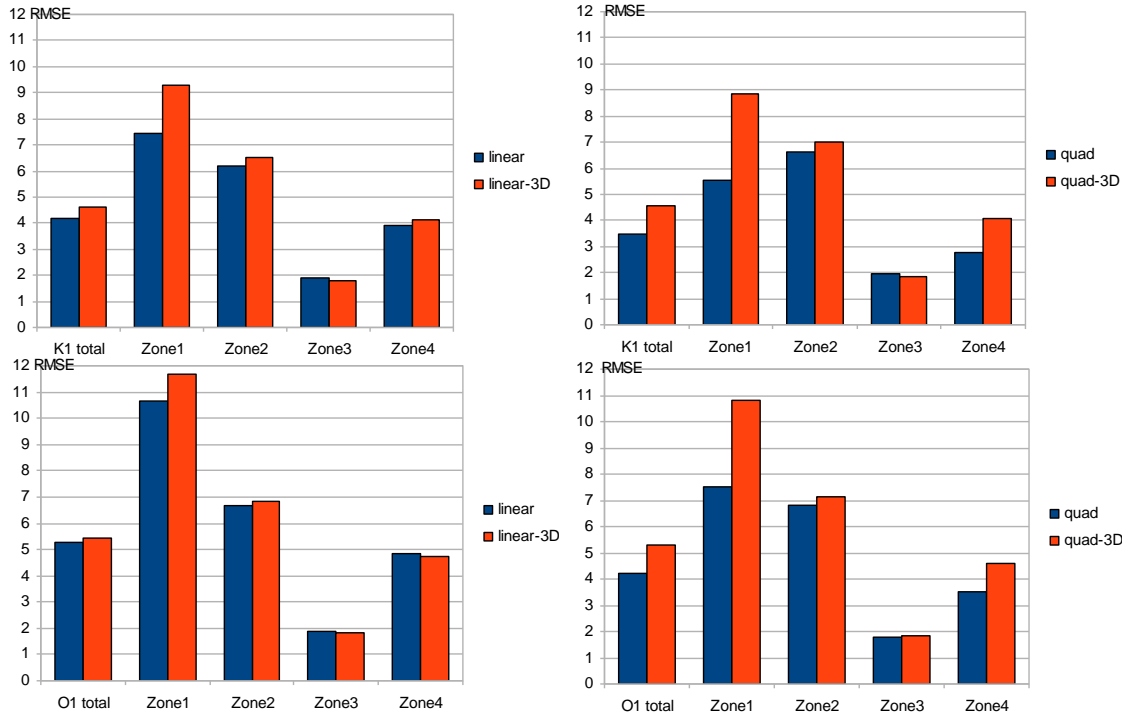


Figure 3.13: RMS Errors of D in 2-dimensional simulations (blue column), and 3-dimensional simulations (red column) for K1 and O1 tidal constituents for two bottom drag coefficients: (a) linear formulation, (b) quadratic formulation.

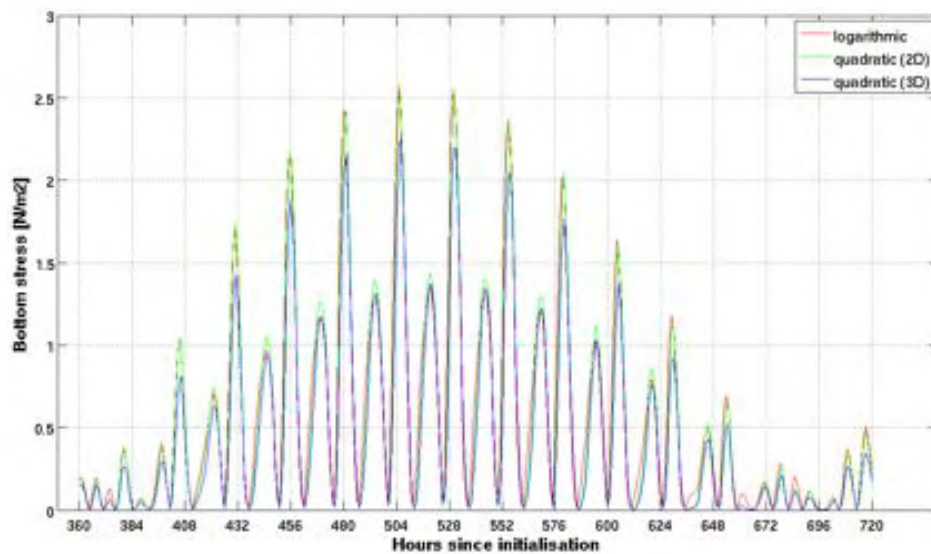


Figure 3.14: Time series of tidal bottom frictional stress $[\text{N/m}^2]$ in 3D simulation using logarithmic drag via bottom roughness $z_0=0.1$ mm (red line), and using quadratic drag law ($C_D=0.001$) in 2D simulation (green line) and 3D simulation (blue line) at a location near Hainan island (latitude= 18.9°N , longitude= 108.53°E , depth= 17m)

Figure 3.14 illustrates details of the temporally varying bottom stresses that are induced in the western Hainan Island (the regions of maximum bottom stress throughout the domain) using logarithmic drag coefficient (via bottom roughness), and constant coefficient used in both 3D and 2D configurations. The

logarithmic-drag/3D case and constant-drag/2D case shows similar bottom friction values, but both are larger than in the constant-drag/3D case.

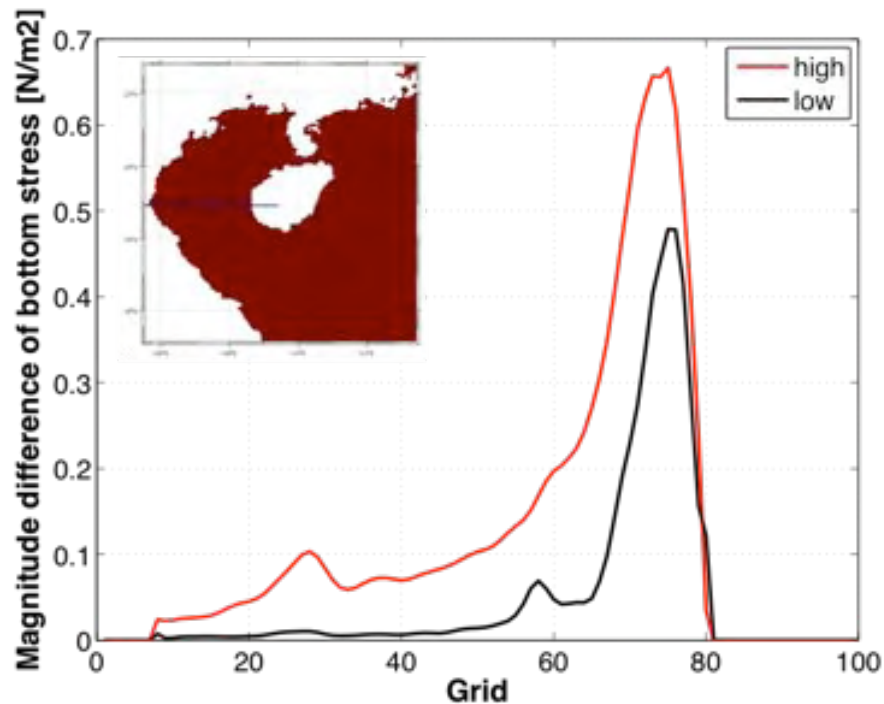


Figure 3.15: Cross section along latitude 18.9°N of bottom frictional stress difference [N/m²] between 3D simulation using logarithmic drag formulation via bottom roughness $z_0=0.1$ mm and 3D simulation using quadratic drag law with $C_D=0.001$. The position of cross section is indicated in the inset panel.

Another perspective is given by a cross section at latitude 18.9°N of bottom stress differences in the 3D simulation between the cases with logarithmic or constant C_D (Figure 3.15). The red curve presents the bottom stress difference for strong tidal flow (505th hour of simulation) and the black curve shows the difference for weak tidal flow (11 hours later). The maximum difference is found in the shallow area off Hainan islands where the tidal currents are also the strongest.

This is an interesting example of how a 3D configuration can degrade the quality of model results. In shallow water, the location of near-bottom velocity (u_b) is closer to the bottom and u_b is therefore weaker than in deeper water (for a similar barotropic flow). In this case the constant drag coefficient yields underestimated bottom friction. Increasing bottom drag would reduce the error in shallow water but increase it elsewhere so that no clear compromise could be found to improve upon 2D simulations. The Logarithmic profile drag formulation is thus clearly at an advantage.

3.4.4 Sensitivity to bathymetry

Here we compare harmonic constants of K1, O1, M2 and S2 components from one year simulation using topographic fields derived from GEBCO_08 and

alternatively from Smith and Sandwell v.14 (Smith & Sandwell, 1997). The Gulf of Tonkin being a shallow basin, the accuracy of water depth may have a great influence on the model solution. The “Smith & Sandwell” database (v.14) is a worldwide set of 1-minute (~2 km) gridded ocean bathymetry recovered from satellite altimetry and ship depth soundings. The difference in the topographic features of the two data sets (GEBCO_08 and Smith & Sandwell v.14) is shown in Figure 3.16. Deep blue shading areas show deeper bathymetry in Smith & Sandwell by 40 m or more. Yellow shading areas show shallower Smith & Sandwell bathymetry by 10m or more. The Figure 3.16 also shows a lot of red areas along the shelf margin indicating that the Smith & Sandwell data is shallower in these areas.

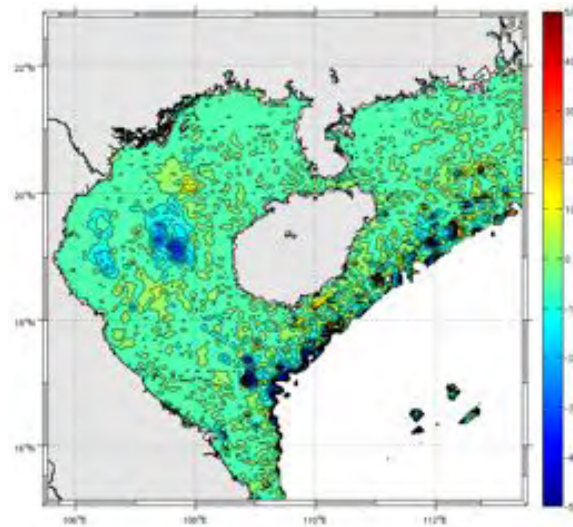


Figure 3.16: Differences in meter between bathymetry derived from GEBCO_08 and from Smith & Sandwell v.14 (isobaths greater than 200 m depth are not shown)

Table 3.5: RMS error of amplitude and phase for 4 components K1, O1, M2, S2 from the simulation using Smith&Sandwell v.14 and GEBCO_08.

Tidal component	K1		O1		M2		S2	
	Smith	Gebco	Smith	Gebco	Smith	Gebco	Smith	Gebco
Topography data								
RMSE-amplitude (cm)	4	3.2	3.8	3	8.5	6.8	3.5	2.9
RMSE-phase (degree)	7.8	9.9	8.1	11.4	11.4	10.5	15	16.3

In general, Smith&Sandwell version 14 yields lower tidal phase error but slightly larger amplitude errors than GEBCO_08 for K1, O1, M2 and S2 components over the Gulf of Tonkin (Table 3.5). However in Zone 2, Smith & Sandwell bathymetry appears to improve a little the tidal elevation and highly improve the phase for all components (Figure 3.17). This may be surprising considering the only small differences of bathymetric depth in this particular region (Figure 3.16) but reveals the high sensitivity of the strait area to details of local or remote topographic representation.

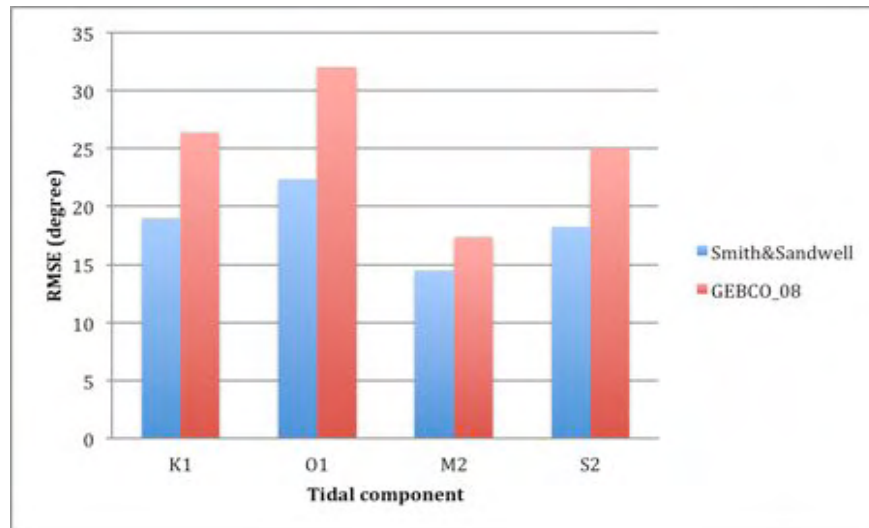


Figure 3.17: RMS errors of the phase of K1, O1, M2 and S2 tidal constituents with difference topography in zone 2.

3.5 Conclusion

ROMS solutions were found to improve tidal predictions in the Gulf of Tonkin compared with previous studies. A careful error analysis is provided by comparison to an unprecedented compilation of observations from tide gauge stations and satellite altimeters.

The addition of 5 years interleaved data increases the number of validated locations, this brings significant improvements for the area of Hainan Strait. On the other hand, it reduces the reliability of M2 amplitude and S2 phase constituents due to the limited time series. Nevertheless, because the Gulf of Tonkin, which is dominated by diurnal tides, the 16 years primary data plus 5 years interleaved data appear as the best data set available. The comparisons between ROMS and the coastal altimetry data show good results in the deep ocean and uncertainties increase significantly near coastal regions or over shallow seas. There are two reasons for this. First, model errors may be higher near the coast due to bathymetric and frictional errors in sensitive shallow water areas. Secondly, the satellite altimetry is limited near the coastlines due to a loss of quality in the measurements. These errors are caused by the land contamination but also by inaccurate geophysical corrections.

The lowest RMS errors were obtained with low values of drag coefficient and bottom roughness, consistent with the fine bottom sediment found in the Gulf of Tonkin (Ma et al., 2010). The use of logarithmic drag coefficient appears crucial for 3D simulations as it accounts for variable vertical grids.

Appendix

A.1 Comparison of altimeter and tide gauge measurements

In order to compare differences between tidal gauge measurements (collected by Chen et al., 2009) and altimeter observations, the tidal harmonic constants at 12 stations (or 17 stations when using interleaved tracks) were compared with those from altimetry observations. The harmonic constants at tidal gauge stations are taken from the archives of the Institute of Oceanography, Chinese Academy of Sciences. Two factors are critical to accurately estimate harmonic tidal constants and avoid aliasing problems: the length and sampling interval of the time series analyzed. We have little knowledge of the time-series except that the tidal analyses are generally based on at least one-year observation (Chen et al., 2009). The four major tidal constituents (K1, O1, M2 and S2) are compared and shown in Table A.1. The highest errors occur for the S2 phase, except at stations around Hainan Island (Nao zhouI, Qinglan, Baosuo, Saya and Bach Long Vy). There is good agreement in amplitude between tidal gauge data and altimetry data for K1 and O1 (smaller than 5 cm at most stations). The rate of **5 cm** accuracy in amplitude is reached in about 76 % cases for K1 and 65 % for O1 among the 17 stations. The phase difference is smaller than 15° at most stations, the rate of 15° accuracy in phase is reached in about 94% cases for K1, 82% for O1. The rate of **10 cm** accuracy in amplitude and 15° in phase is reached in about 52 % cases for amplitude and 58.8 % for phase of M2, 88.2% for amplitude and only 41.2% for phase of S2. This comparison provides an error estimate of measurements, which appear to fall within model-data differences. Measurement errors for M2 and S2 are particularly large without possibility for now to point to any of the data set for better realism.

Table A.1: Differences in amplitude (centimeter) and in phase-lag (degree) of tidal gauges (collected from Chen et al., 2009) and satellite altimetry for 4 components: K1, O1, M2 and S2.

No	Station	K1		O1		M2		S2	
		Amp-diff	Phase-diff	Amp-diff	Phase-diff	Amp-diff	Phase-diff	Amp-diff	Phase-diff
1	Dahengqin	3.55	22.16	2.97	24.78	12.63	26.86	7.53	39.74
2	Bailongwei	5.27	-5.26	1.05	-6.05	-7.81	-15.61	0.62	-59.63
3	Occhucsa	3.93	12.29	-6.17	2.36	-12.47	-17.72	4.96	-44.07
4	NaozhouI.	4.81	12.69	6.25	16.98	18.04	5.26	11.61	11.68
5	Hai'an	3.95	0.40	2.44	2.92	-8.00	32.94	-0.57	18.19
6	BachLongVy	-0.01	1.10	-4.26	7.05	-0.11	-21.69	-1.92	-1.41
7	Haikou	9.75	-20.96	9.40	-15.87	-9.37	25.34	-1.43	10.38
8	Qinglan	0.51	20.63	-2.89	19.08	1.39	16.63	0.45	-22.06
9	Baosuo	7.79	0.80	5.61	0.85	-0.76	-25.35	-1.18	-21.91
10	Lingshuijiao	-0.83	3.61	-4.05	18.68	-3.50	2.65	0.89	16.06
11	Sanya	-2.42	1.77	-0.81	4.00	0.38	1.18	0.85	1.73
12	QuangKhe	-29.34	-95.69	-26.79	-2.50	-0.35	53.83	-1.42	48.47

No	Station	K1		O1		M2		S2	
		Amp-diff	Phase-diff	Amp-diff	Phase-diff	Amp-diff	Phase-diff	Amp-diff	Phase-diff
1	Dahengqin	0.08	6.65	-1.94	8.40	0.85	2.31	-1.51	90.14
2	Bailongwei	4.44	-3.17	-0.23	-4.00	-7.05	-11.73	0.59	-53.13
3	Occhucsa	3.68	12.57	-6.73	2.62	-13.01	-17.04	5.08	-44.62
4	Tsiengmum	12.88	-6.15	7.53	-4.08	-6.91	-115.09	-2.10	-83.49
5	Weizhoudao	-0.39	0.15	-0.66	0.48	1.48	-3.00	0.41	-144.64
6	Naozhou.	2.73	12.67	3.38	15.71	15.62	8.79	10.14	3.78
7	Hai'an	0.36	-2.15	-0.92	4.74	-6.58	60.08	-0.21	51.90
8	BachLongVy	-0.01	1.10	-4.26	7.05	-0.11	-21.69	-1.92	-1.41
9	Haikou	-3.20	-33.26	-2.38	-29.16	-6.39	86.04	-0.16	62.31
10	Yangpu	-2.34	-0.94	-2.65	2.67	3.49	1.42	-2.14	-36.42
11	Yangpu	-1.86	3.54	-6.60	6.98	6.62	-5.71	-1.32	-39.87
12	Qinglan	-6.20	13.39	-8.87	11.25	3.03	15.22	1.21	5.59
13	Baosuo	-3.10	-1.98	-2.08	-3.22	2.00	-1.16	-0.32	-6.69
14	Lingshuijiao	-5.41	6.67	-8.62	23.00	-0.73	2.57	-0.98	46.86
15	Sanya	-3.60	2.40	-1.68	3.28	1.05	4.93	0.78	2.39
16	QuangKhe	-5.58	-7.24	-8.18	-10.15	-7.84	-22.83	-1.68	-11.51
17	DaNang	-1.57	6.76	1.05	2.57	-3.15	0.63	1.98	1.10

A.2 Relative errors

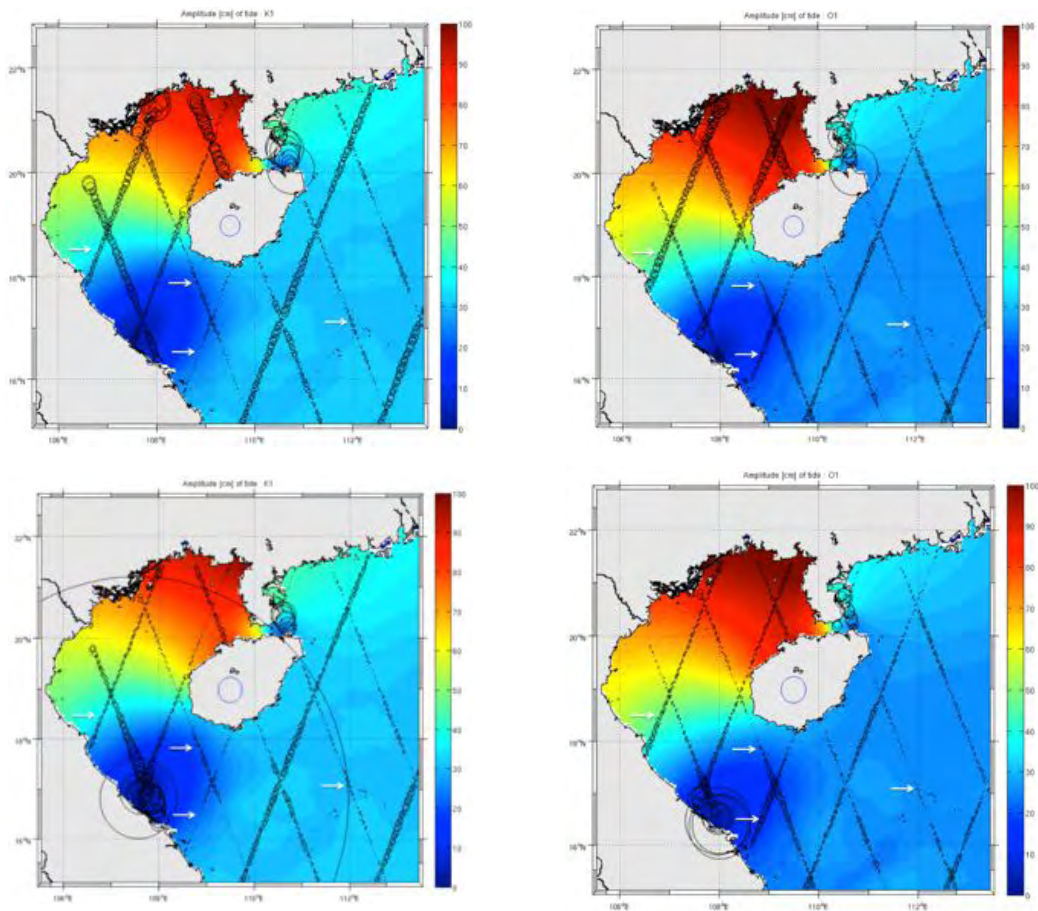


Figure A.1 -1st part- Tidal misfits in the Gulf of Tonkin for K1 and O1 constituent: background chart represents the tidal amplitude in centimeter from ROMS model. The size of the black circles is proportional to the RMS error (top) and relative error (bottom) of amplitude between ROMS model solution and the altimeter-derived. Reference: 10 cm (top) & 0.5 (bottom). The white arrows indicate the primary tracks

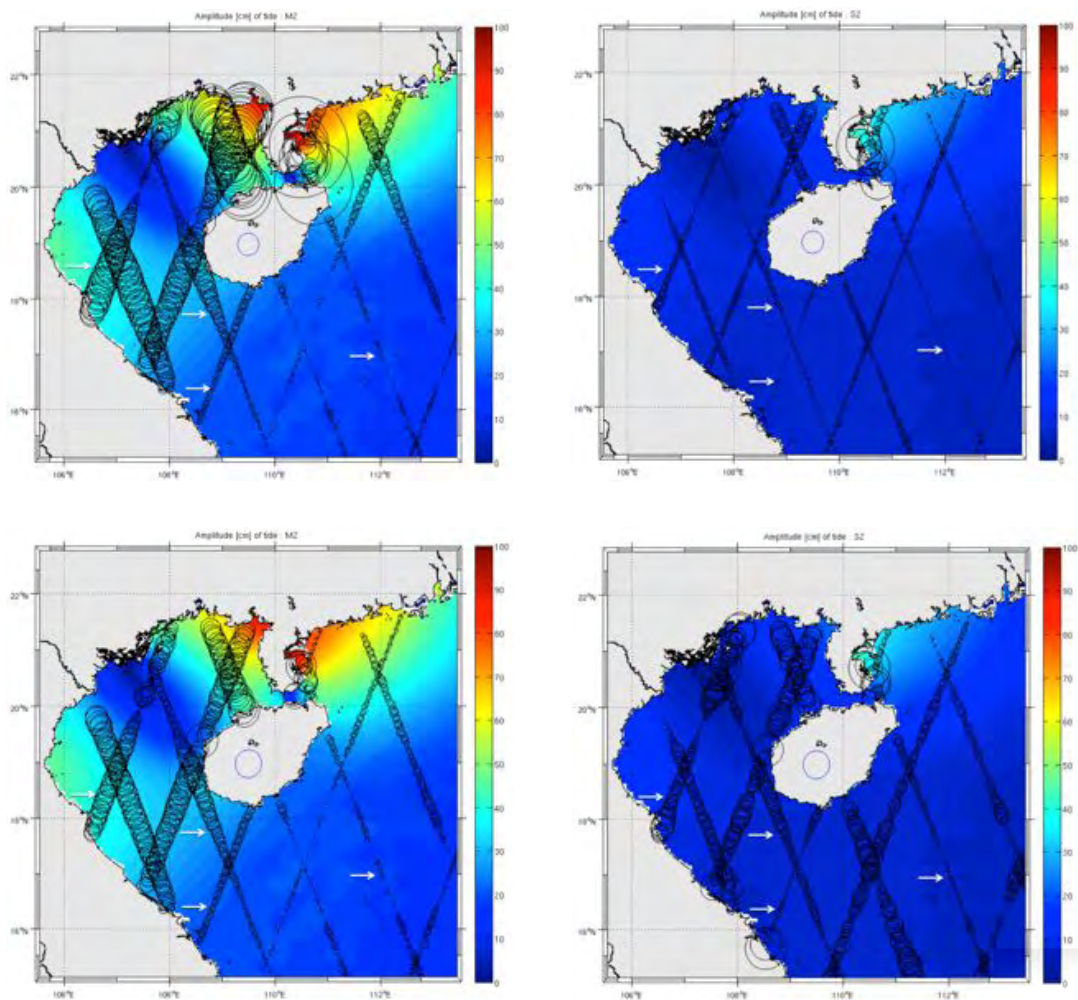


Figure A.1 -2st part- Tidal misfits in the Gulf of Tonkin for M2 and S2 constituent: background chart represents the tidal amplitude in centimeter from ROMS model. The size of the black circles is proportional to the RMS error (top) and relative error (bottom) of amplitude between ROMS model solution and the altimeter-derived. Reference 10cm (top) & 0.5 (bottom). The white arrows indicate the primary tracks.

It is of no surprise that the relative errors show larger values around amphidromic points of K1 and O1 because the tides there are very small (Figure A.1 -1st part). The relative errors for K1, O1 are mostly less than 5% along the southern boundary and the largest errors (~10%) occur in the interleaved ground tracks. For M2, the largest errors (~10%) occur in primary ground tracks. The relative errors for S2 are about 10% and less than 30% in the interleaved ground tracks.

A.3 OTIS forcing

The model M2 and S2 tidal errors evaluated from the coastal tide-gauge and satellite altimeters are high (averaged RMS error of M2 amplitude in the gulf is 8 cm; RMS error of S2 phase: 18 degrees). These errors may be partly due to errors in the open boundary condition. The Oregon State University (OSU) Tidal Inversion Software (OTIS) was used to provide alternative tidal boundary conditions for ROMS in the Gulf of Tonkin. OTIS is a set of programs designed to generate optimal tidal solutions within an ocean domain by 4D variational assimilation of tidal data from various sources, including satellite altimetry and coastal tide gauges (<http://volkov.oce.orst.edu/tides/region.html>). OTIS provides a number of improvements: (1) increased grid resolution (2 minutes); (2) more accurate bathymetry; (3) assimilation of International Hydrographic Office (IH) tide station data (as well as tidal data derived from the TOPEX altimeter data); (4) increased number of representers used for data assimilation. The tides generated by ROMS with boundary conditions from OTIS and from TPXO7 are compared in Tables A.2. As presented in Section 3.2.3, TPXO7 is a global model of ocean tides, which has a horizontal resolution of 0.25 degrees. Using tidal boundary conditions from OTIS gives only a small improvement for S2 compared to TPXO7. It confirms that our model errors do not originate from the boundaries for the most part.

Table A.2: Model RMS errors of amplitude and phase for K1, O1, M2, S2 for simulations using TPXO7 and OTIS forcing. Errors are relative to satellite altimeter data including 5-year interleaved data and 16-year primary satellite altimetry (in bracket).

	RMS error of amplitude (cm)				RMS error of phase (degree)			
	K1	O1	M2	S2	K1	O1	M2	S2
TPXO7	2.84 (3.23)	2.37 (3)	8.06 (6.84)	2.44 (2.88)	10.42 (10)	8.37 (11.43)	7.82 (10.52)	17.74 (16.34)
OTIS	2.8 (3.3)	2.51 (3.1)	7.95 (6.89)	2.36 (2.9)	10.65 (10.15)	8.79 (12)	8.1 (10.24)	17.69 (16.26)

Chapter 4: Tidal flux and resonance in the Gulf of Tonkin

In Chapter 3, we have shown that ROMS can accurately simulate tidal elevations in the Gulf of Tonkin. In this section, based on tidal energy budget and on the model estimation of resonance modes, we present calculations of the amount of tidal energy flux entering the Gulf of Tonkin, estimate energy flux dissipated inside it, and evaluate resonant amplification of the various tidal components.

4.1 Tidal energy flux

The energy budget of the barotropic tides is a highly valuable tool for investigating and understanding tidal dynamics. Based on the calculation of the tidal energy budget toolkit developed at LEGOS, France (Pairaud et al., 2008; see description in Chapter 2), ROMS simulations will be used to calculate the amount of tidal energy flux entering the Gulf of Tonkin and estimate energy flux dissipated inside it. In semi-enclosed areas like the Gulf of Tonkin, the direct effect of the tidal-generating force is small and is not considered here. Therefore, the tides in the Gulf of Tonkin are tidal waves propagating from the open boundaries. The difference between inward and outward fluxes represents the dissipation rate in the gulf.

The distribution of depth-integrated energy-flux vectors for the 4 principal constituents K1, O1, M2 and S2 over a tidal period is shown in Figure 4.1. The spatial distribution and magnitude of K1 and O1 are quite similar. The magnitude of K1 and O1 flux is 3 times higher than the M2 flux and 20 times higher than S2 flux. The tidal motion in the Gulf of Tonkin is thus maintained by energy flux from the diurnal components as expected. A large part of incoming tidal energy is seen to flow southwestward along the continental shelf before reaching the gulf's entrance. Some of this energy flows along the eastern side of Hainan Island towards the Hainan Strait. Tidal energy enters the gulf from the south with a sharp northwest bifurcation and flows along the west side of Hainan Island. A return flow of energy of weaker amplitude can be seen along the western side of the bay. This pattern of energy flux in the gulf is consistent with a Coriolis effect: incoming tidal waves tend to be deflected to the right by Coriolis forcing; they get partly dissipated and reflect against the northern enclosure of the gulf; then they propagate southward. A very noticeable feature is the tidal flux convergence in the Hainan Strait (80km long and 25km wide).

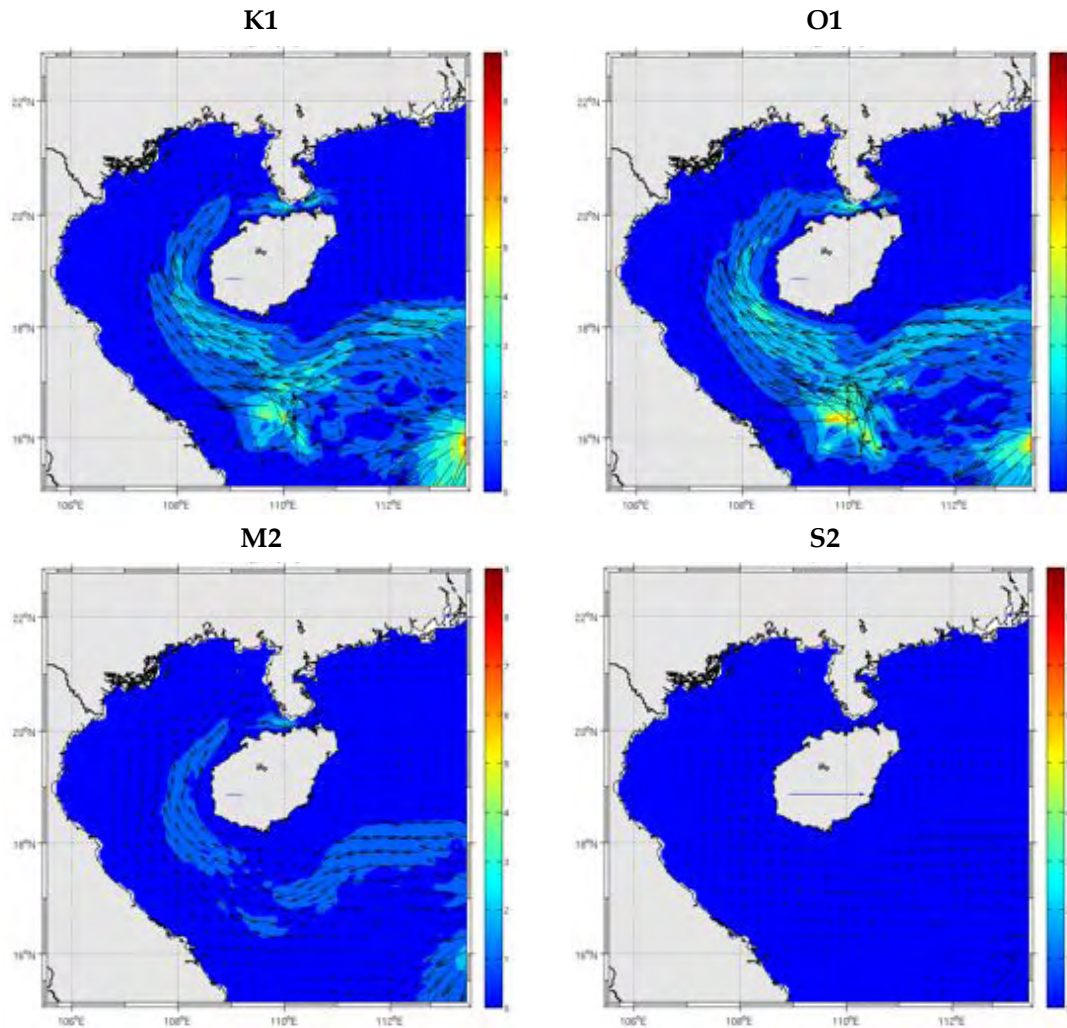


Figure 4.1: Tidal energy flux for K1, O1, M2 and S2 (left to right, above to below). Colors present the magnitude of flux [W/m]. Vector reference 10 kW/m.

The total amount of tidal energy flux entering the Gulf of Tonkin from the Vietnam East Sea/South China Sea can be estimated by integrating the energy flux across the gulf's mouth (S1) and through the Hainan Strait (at S2 and S3). The calculated energy fluxes through each section S1, S2, S3 (Figure 4.2) are listed in Table 4.1. The tides in the Gulf of Tonkin are entirely maintained by energy flux through section S1 since no energy enters through S2. Tidal energy enters the Hainan Strait through S3 but at a much lower rate than through S1 (6 times lower for K1, 9 times for O1, 17 times for M2 and 7 times for S2). This energy is totally dissipated within the strait. 20% to 30% of the energy entering through S1 reaches S2 and is also dissipated in the Hainan Strait. Overall, the energy loss in this strait is about 30% of what enters through S1 and S3, the remaining 70% is dissipated in the Gulf. In dynamical terms, the Hainan Strait can be considered closed to tidal waves, justifying the use of a semi-enclosed rectangular basin to describe the Gulf of Tonkin (next section). Beside the Hainan Strait, the major region of high energy dissipation is found off the western Hainan Island. This is where tidal currents are the largest in the gulf as a result of Coriolis effect.

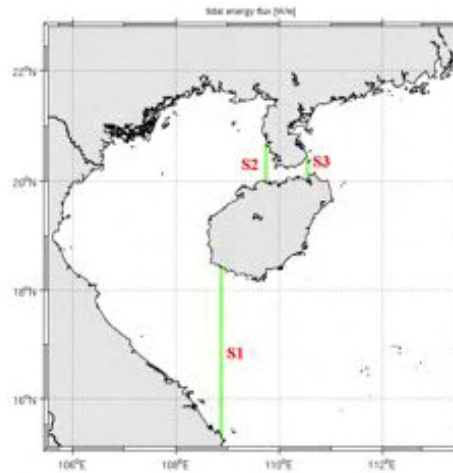
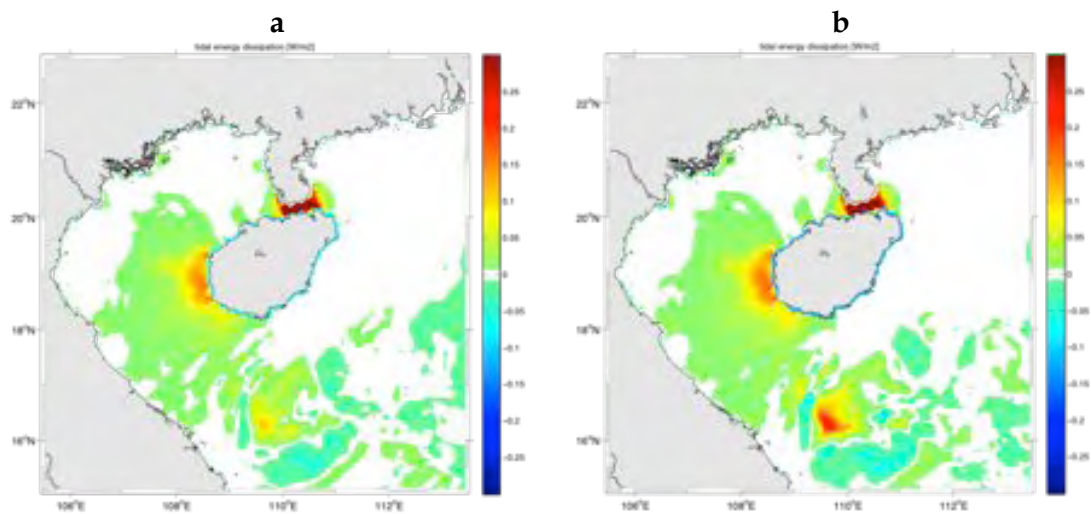


Figure 4.2: Sections S1, S2, S3 where energy fluxes are calculated in Table 4.1

Table 4.1: Tidal energy flux in the gulf of Tonkin [kW]. Positive values indicate energy entering the gulf and negative values indicate energy leaving it.

	S1	S2	S3
K1	551.6	-115.4	92.3
O1	612.6	-139.3	69.1
M2	330.4	-93.1	19.1
S2	29.9	-9.9	4.1



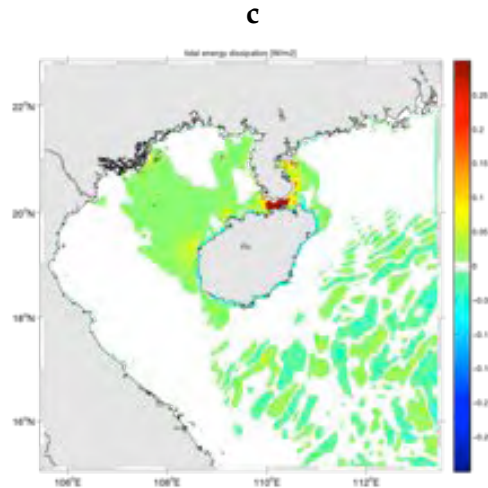


Figure 4.3: Energy dissipation of K1, O1, M2 tidal component [W/m²].

4.2 Tidal resonance

The response of the coastal seas to tidal forcing depends on the properties of offshore tides, the details of bathymetry and coastline, and the influence of friction. Tidal resonance occurs when the offshore tide excites one of the resonant modes of the ocean. Knowing how close a system is to resonance provides an indication of the sensitivity of the local tidal regime to mean sea level changes and to changes in geometry caused by human activities (Sutherland et al., 2005).

4.2.1 The rectangular bay model

A kind of resonance may be produced in a bay by an oscillatory external tide: the Helmholtz mode (Mei, 1989). This mode can be best understood as a perturbation of an enclosed basin. It is the lowest mode of such a basin and is generally the most energetic; it has a single nodal line (zero sea level) at the mouth of the bay that opens onto a much larger body of water and a single anti-node on the opposite shore. Tidal resonance can occur if the bay is about a quarter wavelength wide. In this case, an incident tidal wave can be reinforced by reflections between the coast and the shelf edge, the result producing a much higher tidal range at the coast.

More specifically, if we consider the Gulf of Tonkin as an ideal rectangular gulf of length L and constant water depth h , which communicates with a deep ocean at the open end, we can compute a solution for resonant modes (Taylor, 1922). For that, we assume that the gulf is sufficiently narrow for the Coriolis force to be neglected. In this case, the linear, non-rotating, one-dimensional shallow water equations with linear friction can be written for a complex tidal height $\xi e^{-i\omega t}$ and current $u e^{-i\omega t}$:

$$-i\omega u + g \frac{\partial \xi}{\partial x} + \frac{ru}{h} = 0 \quad (4.1)$$

$$-i\omega\xi + h\frac{\partial u}{\partial x} = 0 \quad (4.2)$$

With boundary conditions $u(L) = 0$ and $\xi(0) = A_0$ at the entrance and head of the gulf, the solutions to the shallow water equations are in the form of a standing wave, with:

$$\xi(x) = \frac{A_0 \cos k(x-L)}{\cos(kL)} \quad (4.3)$$

$$u(x) = \frac{i\omega A_0 \sin k(x-L)}{kh \cos(kL)} \quad (4.4)$$

where:

$$k \approx \frac{\omega}{c} \left(1 + i \frac{r}{2h\omega} \right) \quad (4.5)$$

A_0 is the tidal amplitude at the gulf entrance, and $c = \sqrt{gh}$ is its propagation speed. At the head of the gulf ($x=L$), the amplitude is:

$$A_L = \frac{A_0}{\cos(kL)} \quad (4.6)$$

Therefore, if $\cos(kL)=0$, resonance occurs. If bottom friction is negligible, this is verified with:

$$k = \frac{\pi}{2L}, \quad \frac{3\pi}{2L}, \quad \frac{5\pi}{2L} \quad \dots$$

These are the specific oscillation modes, i.e., the various eigen modes of the basin. The first resonance mode (the Helmholtz mode, generally the most energetic) is associated with the non-dimensional gulf length $kL = \pi/2$, i.e., with gulf length $L = \lambda/4$ the quarter wavelength, where λ is the length of incoming tidal wave (Figure 4.4). The associated resonant angular frequency and period are:

$$\omega_0 = 2\pi \frac{\sqrt{gh}}{4L} \quad \text{and} \quad T_0 = \frac{4L}{\sqrt{gh}} \quad (4.7)$$

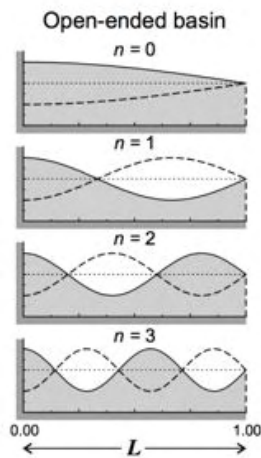


Figure 4.4: Surface profiles for the first four seiche modes in open-ended rectangular basins of uniform depth

The length of the Gulf of Tonkin is about 500 km and its average depth is 50 m. Therefore resonance would occur for a tidal forcing period of $T_0 = 25.1$ hours, which is close to the period of O1 (Fang et al., 1999).

However, neglecting the Coriolis force may not be appropriate as the width of the basin is larger than the Rossby radius of deformation (Jonsson et al., 2008). As seen in the previous section, the incoming diurnal tidal waves tend to be deflected to the right by Coriolis forcing, are partly dissipated and reflect against the northern enclosure of the gulf. The reflected waves then propagate southward. The result is a mixture of a standing wave, a northward-propagating wave in the eastern part, and a southward-propagating wave in the western part. Earth rotation would tend to favor larger tidal currents in the incoming tide (on the eastern side) rather than the reflected tide that is partly dissipated. This would explain the observed strong tidal current off the western shore of Hainan island. Coriolis forcing also produces a frequency shift of the resonant wave. Taylor (1922) and van Dantzig and Lauwerier (1960) proposed a general expression for this frequency shift, again for a rectangular basin. Jonsson et al. (2008) added a useful simplification for narrow bays (if the width is no more than half the length):

$$\omega_0 = \frac{\pi c}{2L} + \frac{16Wf^2}{\pi^4 c} \quad (4.8)$$

W is the width of the basin (270 km for the Gulf of Tonkin) and f is the Coriolis frequency ($\sim 0.5 \cdot 10^{-4} \text{ s}^{-1}$ at 20°N). The period after correction for rotation is 23.4 hours, which is shorter than the period of O1 and closer to K1, therefore not a good model for explaining observations.

Obviously, we cannot expect the crude estimate of treating the Gulf of Tonkin as a flat-bottomed rectangular gulf to yield an accurate result. This model is useful for some preliminary estimates but analytical solutions can be found for several other basins of simple geometric form and non-uniform depth. Rabinovich (2009) summarizes results that involve common basin shapes (Figure 4.5). A particularly interesting one is the rectangular basin with linear slope (see Figure 1.2 for the bathymetry of the gulf). The solutions for resonant periods are in this case:

$$T_0 = \frac{5.24 L}{\sqrt{gh}} \quad \text{for mode 0 (Helmholtz)} \quad (4.9)$$

$$T_1 = \frac{2.28 L}{\sqrt{gh}} \quad \text{for mode 1} \quad (4.10)$$

$$T_2 = \frac{1.46 L}{\sqrt{gh}} \quad \text{for mode 2} \quad (4.11)$$

Table 4.5. Modes of free oscillations in semi-closed basins of simple geometric shape (modified after Ref. 95).



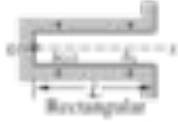

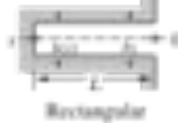

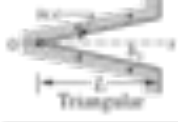

Basin type		Profile equation	Fundamental T_0	Periods of free oscillation			
Description	Dimensions			Mode ratios T_n/T_0 ($n = (a + 1)/2$)			
				$a = 0$	1	2	3
		$A(x) = h_0$	$2.000(2L/(\rho gh_0)^{1/2})$	1.000	0.333	0.200	0.143
		$A(x) = h_0 x/L$	$2.419(2L/(\rho gh_0)^{1/2})$	1.000	0.435	0.279	0.200
		$A(x) = h_0(2 - x^2/L^2)$	$2.220(2L/(\rho gh_0)^{1/2})$	1.000	0.409	0.259	0.199
		$A(x) = h_0 x/L$ $A(x) = h_0$	$2.399(2L/(\rho gh_0)^{1/2})$	1.000	0.435	0.279	0.230

Figure 4.5: Table of resonant solutions for various idealized open basins summarized by Rabinovich (2009).

With $L=500\text{km}$ and $h=60\text{m}$ at the entrance of the Gulf of Tonkin (Figure 1.2), we have $T_0=30.0\text{ h}$, $T_1=13.0\text{ h}$ and $T_2=8.4\text{ h}$. Then accounting for earth rotation we should expect smaller values, i.e., closer to 29 h and 12 h respectively for the first two modes. These values are consistent with observations if **bottom friction** is considered, as it tends to broaden the resonance peak. From Rabinovich (2009), the width of resonant peak roughly follows the relation:

$$\Delta\omega = \frac{\omega_0}{Q} \quad \text{or} \quad \Delta T \approx \frac{T_0}{Q} \quad (4.8)$$

with $Q = \frac{h\omega_0}{r} \approx \frac{L}{W}$

Q is the quality factor measuring energy damping in the system. Taking $r=1\text{ mm/s}$ and $h=50\text{ m}$ gives $Q=3$ (close to $L/W \approx 2$), the width of resonant period ΔT is about 10 hours and the amplification factor at the resonance peak is $Q^2=9$ (Rabinovitch, 2009). Both O1 and K1 are thus affected by resonance and O1 is closer to the resonance peak than K1, explaining its larger amplitude at the head. We also note that mode 1 is close to the semi-diurnal tides, which should thus also experience resonance with a wavelength 0.435 times that of the Helmholtz mode (Figure 4.5). Mode 1 has 2 anti-nodal lines (of large amplitude tides), which is what we clearly observe for M2.

4.2.2 Numerical simulations

We now use our numerical model to provide an estimate of resonant modes under the influence of complex bathymetry and coastline and of the Hainan Strait

opening in the north. The model is forced by a single tide with amplitude and phase of the O1 constituent derived from the TPXO7 global tidal model, but the forcing period is varied over a range between 4 and 56 hours. The model is run for 360 hours and the last 240 hours are selected for analysis. An index of resonance is provided by amplitude ratios between values at the head of the Gulf (20.97°N, 108.97°E) and at an offshore Vietnam East Sea/South China Sea location (the southeast corner of the domain).

Mode 0: Figure 4.6 shows the resonance diagram determined from the numerical experiments. A broad resonant peak is found around a period of about 29 hours, which is far from the simple rectangular basin value of 25.1 hours, but very close to the case with constant slope, especially if we account for the Coriolis effect. The diurnal tides are clearly influenced by the resonant process with O1 being closer to the peak. The amplification factor at resonance is about 7 and quality factor $Q=2.6$, which are close to the theoretical values of 9 and 3 respectively. The width of the resonant periods is about 10 hours again as predicted by the ideal open basin case.

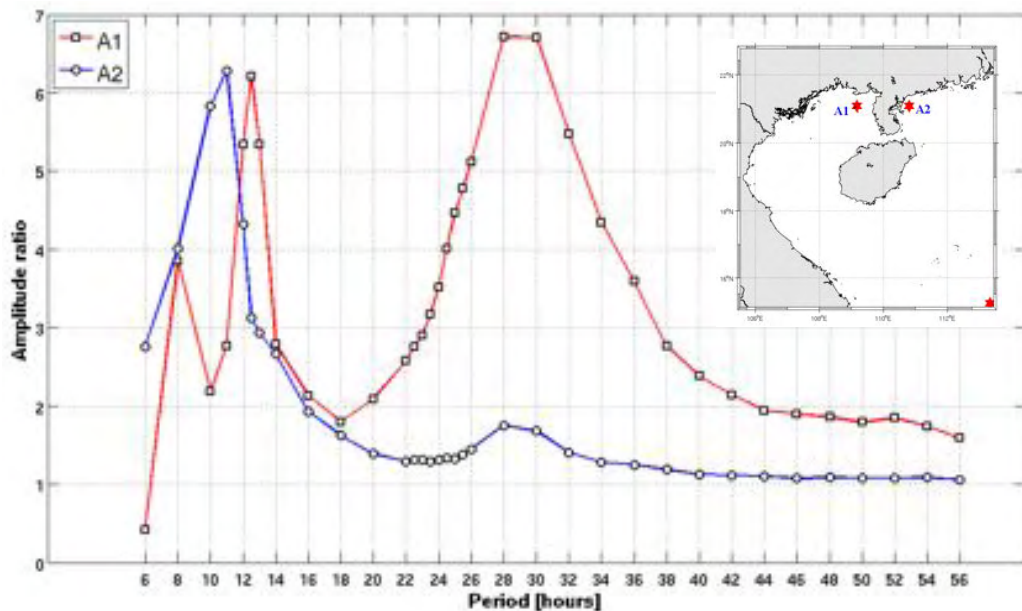


Figure 4.6: Resonance index (Amplification factor) presented as the amplitude ratio between coastal and offshore amplitudes. The offshore location is representative of the Vietnam East Sea/South China Sea and is taken in the southeast corner of the domain. The coastal locations are at the head of the Gulf (20.97°N, 108.97°E; red curve) and off eastern Leizhou peninsula (blue curve).

Mode 1: Interestingly, as in the non-uniform rectangular basin case, there is a second resonant peak in the semi-diurnal range. Its amplitude is a bit lower than the zeroth mode and narrower suggesting a lesser effect of friction (presumably because the currents are weaker and $r=C_D|u|$). It involves a wavelength 0.42 times that of the zeroth mode, very close to the factor 0.435 given by the theoretical model. It is also consistent with observations: Figure 3.7 shows for M2 two nodal lines around the middle and the entrance of the bay and two anti-nodal lines at the head and towards the entrance. In addition to these two resonant

peaks, there is a background amplification factor of about 2 that may be attributed to the process of tidal focusing rather than constructive interference.

If semi-diurnal tides were also resonant, what would explain their lower amplitudes in the gulf? To understand the hierarchy of observed tidal amplitudes, it is important to also account for amplitude differences in the Vietnam East Sea/South China Sea. At the southwest corner reference location, the amplitudes of O1, K1, M2, S2 are respectively: 27cm, 33cm, 16cm and 6cm. Therefore, the reason why O1 amplitude in the Gulf is higher than K1 is a larger resonant effect (O1 is closer to the resonant peak period of 29 hours), not a larger value in the Vietnam East Sea/South China Sea (it is actually the opposite). On the contrary, the reason why semi-diurnal tides are smaller in the gulf is that they are already smaller outside but they resonate in the gulf as much as diurnal tides. Lyard et al., (2006; Figure 1.3) and Zu et al., (2008) attribute the relatively large amplitude of diurnal tides in the Vietnam East Sea/South China Sea to Helmholtz resonance. Helmholtz resonance occurs in a basin with a small entrance, in this case Luzon Strait that is the main opening for tidal energy flux in this basin.

Mode 2: A third resonant peak around 8 h is suggested by the numerical experiments, which would coincide with mode 2 of the non-uniform rectangular bay ($T_3=8.4$ h) but our sampling strategy does not allow further investigation of these periods.

Outside of the gulf, we also note a resonant semi-diurnal shelf mode off the eastern Leizhou peninsula (blue line in Figure 4.6) that explains the high values of M2 and S2 in this region. On the contrary, diurnal amplification is small there as expected from the theory of shelf tides (Clarke and Battisti, 1981).

If numerical models are useful to estimate resonance effects, there are subject to errors due to uncertainties in the bathymetry and damping by bottom friction. As we have seen in the section on sensitivity analysis, the friction coefficient used in our model lacks spatial variability and is only tuned for best statistical properties. In addition, damping can be very different for a single tide and for combination of tides. These uncertainties may alter our resonance analysis. Nevertheless, it provides useful arguments to explain the observations and anticipate possible changes. For example, using the recorded mean sea level rise of 18 cm in the last 40 years (Hirai et al., 2008), the non-uniform rectangular bay model predicts that a 50 cm rise in sea level in a century would shift down the resonant peak by about fifteen minutes.

Chapter 5: Residual transports

Firstly, we provide a brief description of the physical processes, which dominate circulation patterns in the Gulf of Tonkin. What is the role of tides in the Gulf?

5.1 Tide-induced residual current and transport

In shallow water, the trajectory of a water parcel during a tidal period is not closed due to nonlinear effects (associated with bottom friction and momentum advection). The oscillating tidal currents thus contribute to a residual transport. The tidal residuals are important because they are persistent features, linked to local bottom topography (bumps and ridges) and coastal features (headlands, capes). Therefore, even if they are considerably weaker than storm-driven residual wind drifts which occasionally occur, they can contribute more significantly to the overall long-term distribution and transport of water properties than do the stronger, but intermittent and directionally inconsistent wind-driven flows.

The residual is defined as the time mean over period T , so that the residual a_R of a fluid parameter a would be:

$$a_R = \frac{1}{T} \int_{t_0}^{t_0+T} a \, dt \quad (5.1)$$

Eulerian and Lagrangian approaches provide two different ways to get the residual current. The time-averaged circulation can be obtained by averaging the simulated instantaneous flow at a fixed point in several periods, i.e. Eulerian residual (\bar{u}_E); or by dividing the net displacement of a water parcel in an average time period, i.e. Lagrangian mean velocity. According to Longuet-Higgins (1969), the Lagrangian flow is the sum of the Eulerian flow and the Stokes drift that is induced by the mean kinetic energy and coastal nonlinear interaction. Stokes drift is large in the coastal sea and in areas where the vorticity and/or divergence are large.

5.1.1 Eulerian residuals

Eulerian residual currents are defined as:

$$\bar{u}_E = \frac{1}{T} \int_{t_0}^{t_0+T} \bar{u}(x_0, t) \, dt \quad (5.2)$$

\bar{u}_E is the Eulerian residual current, \bar{u} is instantaneous velocity at time t and at fixed point x_0 , T is the tidal period. This definition is not directly usable for a signal composed of multiple harmonics. On the other hand, we cannot use the model solutions of individual tidal constituents because they do not linearly combine. Nonlinear interactions between tidal constituents and nonlinear bottom friction effects on the flow need to be accounted for. The only solution is to average the full tidal solution over a long period of time. One-year averaging was required properly filter out transient signals. The Eulerian residuals are presented

in Figure 5.1. The strongest residual current is found in the Hainan Strait (~ 20 cm/s). The residual flow near the southwestern and western Hainan Island is about 6-8 cm/s. Along the western coast of the gulf, the residual current reach a maximum of 2 cm/s around headlands. The residual flow also displays several small clockwise and counterclockwise eddies. These richly varied residual flow patterns, which include gyres and coastal currents, result from the nonlinear interaction of tides and residual currents with the bathymetry (Zimmerman, 1980).

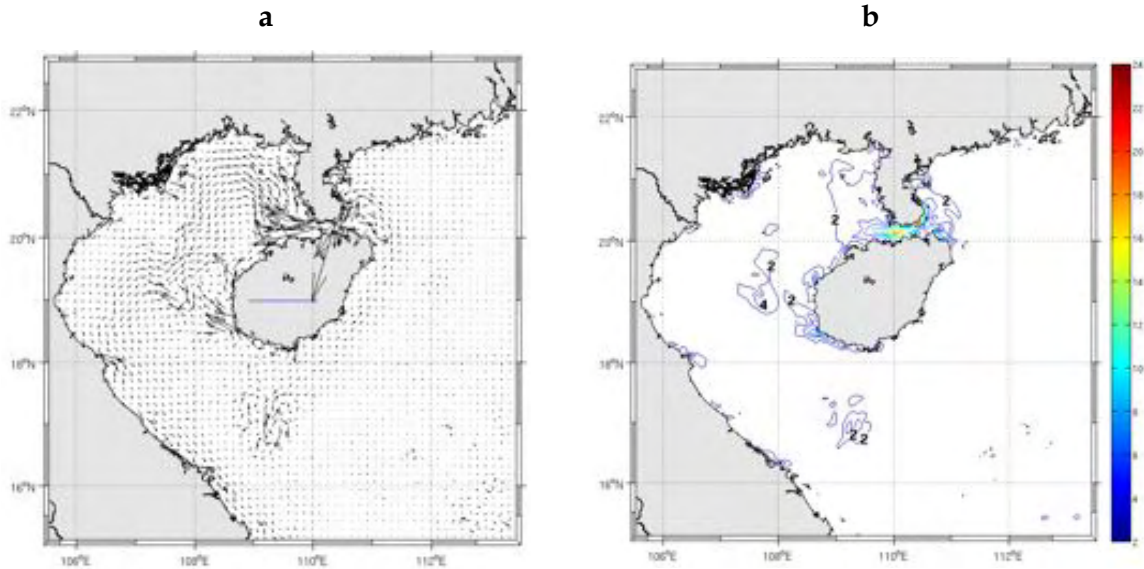


Figure 5.1: Eulerian tidal residual currents at the surface due to the eight primary tidal constituents (a: vector, b: contours). Reference vector: 20cm/s

The Eulerian residual transport is a more meaningful quantity than the Eulerian residual velocity because it includes the effect of co-variations of tidal velocity and water depth during the tidal cycle, and thus represents the net flow over a unit width for a depth-averaged model. The residual streamfunction ψ can be computed from the mean Eulerian transports:

$$\begin{aligned}
 U &= \frac{\partial \psi}{\partial y} \\
 V &= -\frac{\partial \psi}{\partial x} \\
 [U, V] &= \frac{1}{T} \int_{t_0}^{t_0+T} [u, v](h + \zeta) dt
 \end{aligned} \tag{5.3}$$

$[u, v]$ is the depth-averaged tidal residual current in the x and y directions; h is basin depth below the mean tide; ζ is elevation of the water surface referenced to mean tide; t_0 is an initial time and T is the period of a tidal cycle. Figure 5.2 shows the residual streamfunction that reveals a coherent anticlockwise circulation around Hainan with a transport located in the center of the gulf. Small isolated eddy structures also appear along the coast.

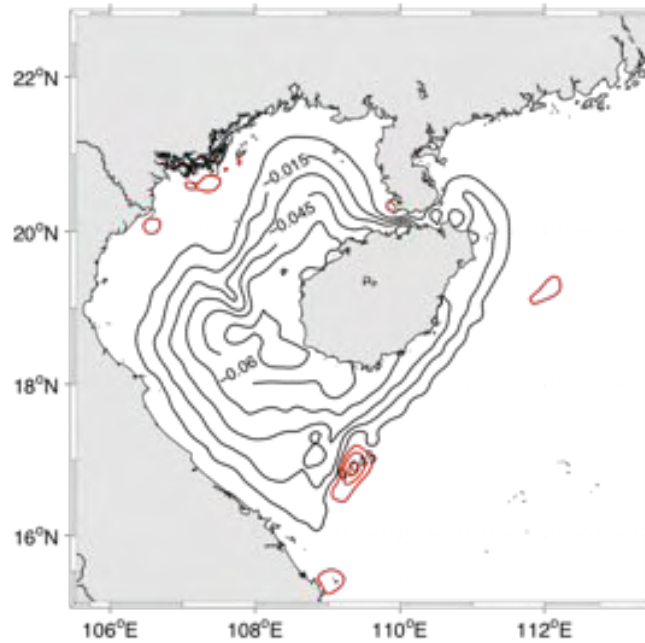


Figure 5.2: Depth-integrated tidal transport streamlines from Eulerian residual transports. It shows an anticlockwise circulation around Hainan Island. Units are in Sv; contour interval=0.015 Sv.

5.1.2 Tide-induced Lagrangian residual current

The Lagrangian mean velocity is formulated as:

$$\bar{\vec{u}}_L = \frac{1}{nT} \int_{t_0}^{t_0+nT} \vec{u}[\vec{x}(\vec{x}_0, t), t] dt \quad (5.4)$$

$\bar{\vec{u}}_L$ is the Lagrangian mean velocity, \vec{u} the tidal current, T the tidal period, \vec{x}_0 is the starting point of one particle and \vec{x} is the position of that particle at time t . Lagrangian residual currents are the average velocities of marked water parcels tracked over one or more (n) tidal cycles (Feng, 1987). The Lagrangian mean velocity is also described as the net displacement of a marked particle over one or more tidal cycles divided by the displacement time.

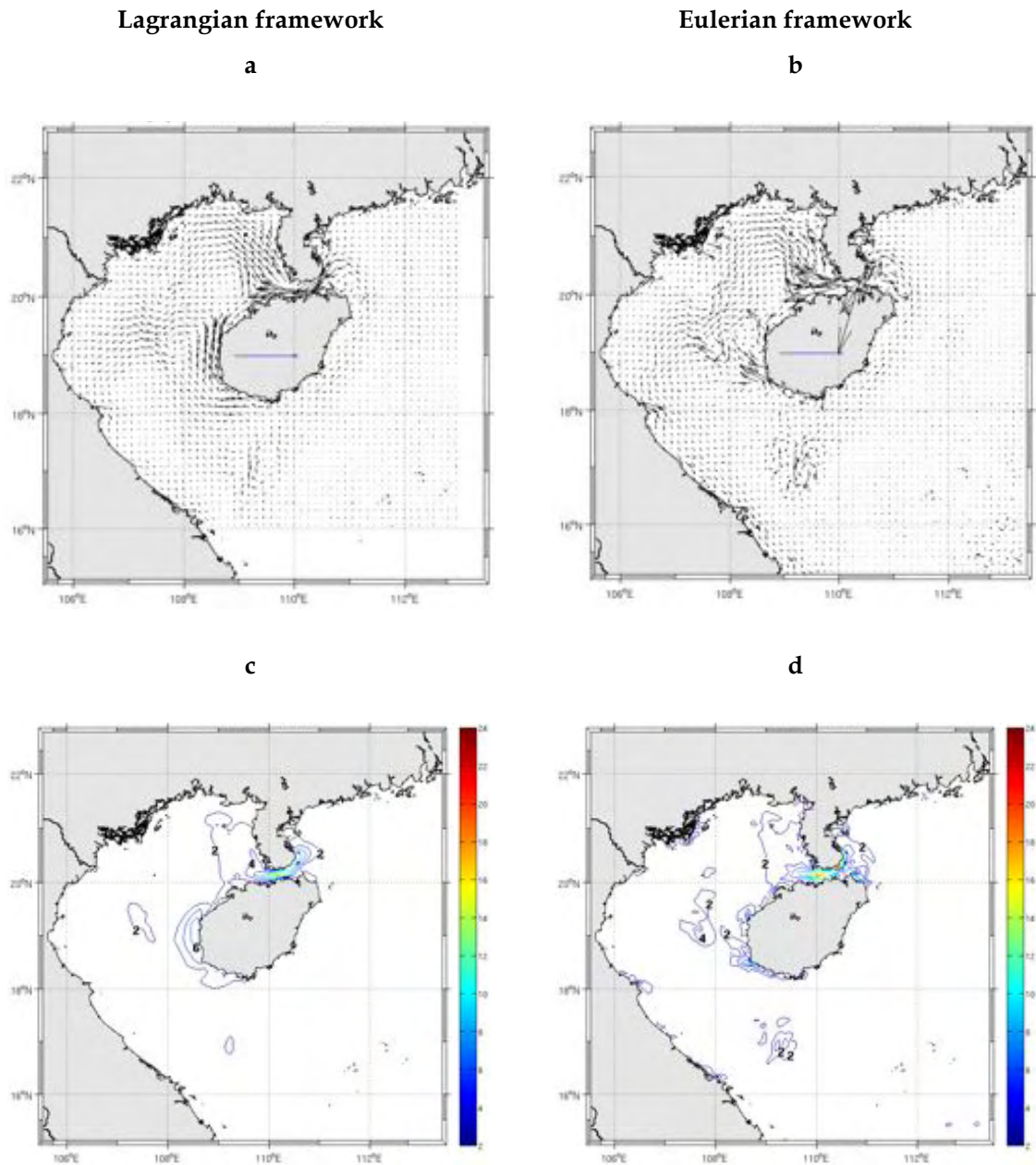


Figure 5.3: The Lagrangian (a: vector, c: contours) and Eulerian (b: vector, d: contours) tidal residual currents at the surface. Reference vector: 20 cm/s

We used the offline Lagrangian float model ARIANE (Blanke et al., 1997) to compute the trajectory of particles released at every surface grid cell and advected by 3D hourly velocity fields from ROMS simulations. The particles are released at time t_0 and tracked for 3 months. Their displacement from the release points indicates a net drift that accounts for the Lagrangian velocity. Figure 5.3 compares the Lagrangian and Eulerian velocities. The Lagrangian flow appears qualitatively close the Eulerian flow but weaker. The differences of tidal residual circulation in Lagrangian and Eulerian frameworks may be understood through a vorticity

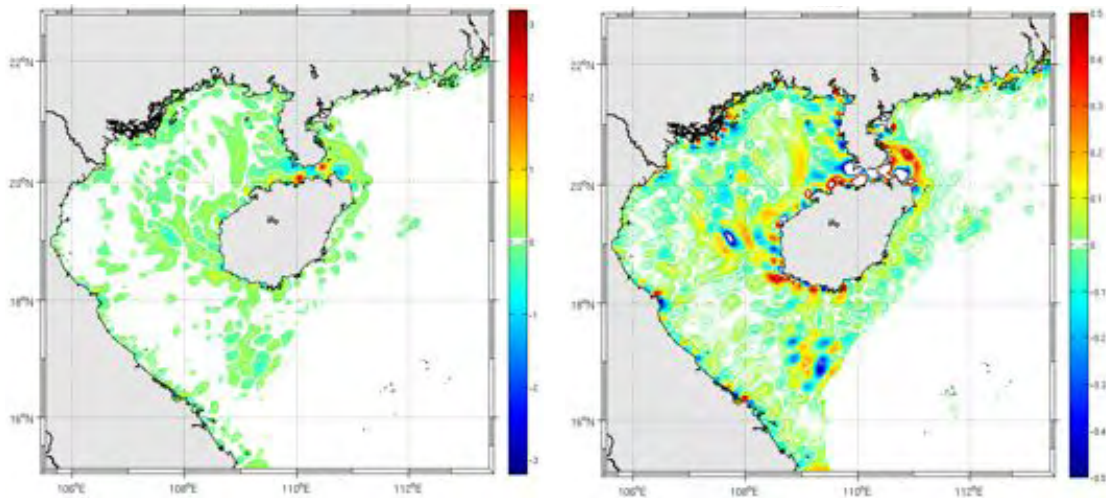
description (Garrett , 1993). The vertical component of the fluid's relative vorticity is:

$$\xi = \frac{\partial v}{\partial x} - \frac{\partial u}{\partial y} \quad (5.5)$$

ξ is positive for counterclockwise flow, and negative for clockwise flow. With water depth $h(x)$ and the Coriolis parameter f , The potential vorticity of the fluid is conserved following the flow:

$$\frac{D}{Dt} \left(\frac{\xi + f}{h + \zeta} \right) = 0 \quad (5.6)$$

If a parcel moves into shallower water during a given tidal phase, the relative vorticity has to decrease in order for potential vorticity to be conserved (negative relative vorticity corresponding to clockwise rotation). Fluid that is moving in the opposite direction in the following tidal phase takes on a positive relative vorticity, corresponding to counterclockwise rotation. So the tide leaves a residual vorticity, negative near the top of the slope and positive near the bottom. This happens at every point along a shelf profile, and leaves the residual Eulerian current flowing parallel to the isobaths. For a clockwise-rotating tidal current (the general tendency in the Gulf of Tonkin; see Zu et al., 2008), the corresponding Stokes drift will oppose it, which means that the net Lagrangian current is weaker than the Eulerian current.



Figures 5.4: Annual mean depth-integral relative vorticity contours (The right plot presents more clearly pair of positive and negative relative vorticity along the coast), divided by 10^{-5}

5.2 Subtidal residual flow

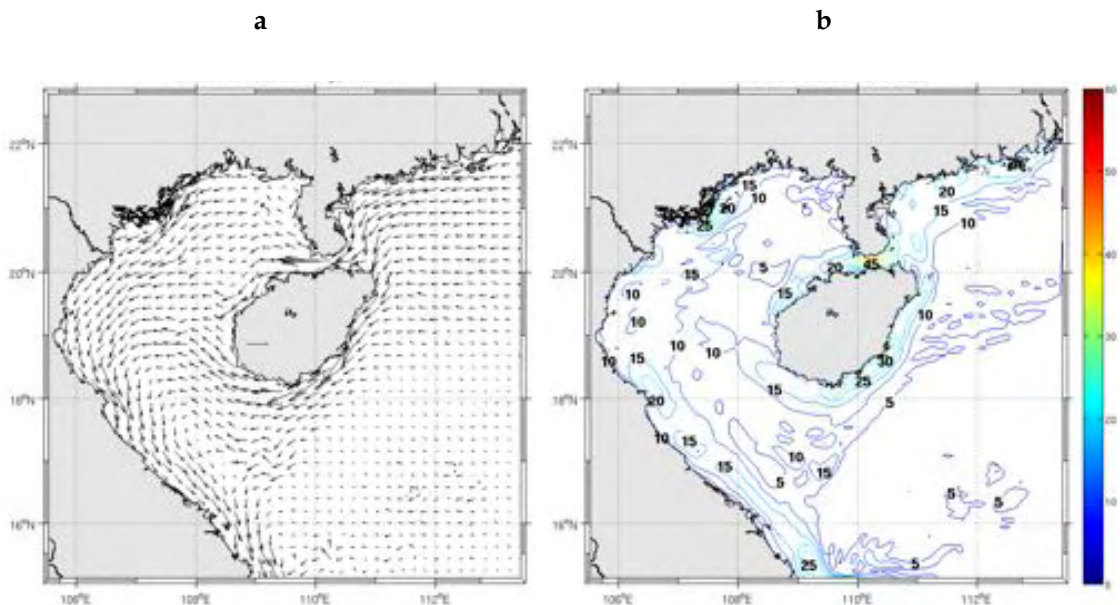
Subtidal residual currents can be driven by wind forcing or lateral density gradients due to non-uniform salinity or temperature distributions. In this section, we will sequentially consider the residual circulation resulting from wind alone

and density-driven circulation. Here, we will not give a complete picture of subtidal circulation in the Gulf of Tonkin but simply provide elements of comparison between tidal and subtidal residual currents. In particular, a strong seasonality in surface forcing, related to winter and summer monsoon, is shown to affect the interplay between tidal and subtidal flow.

5.2.1 Wind-driven circulation

In this case, density is assumed constant and there is no tidal forcing. The model is only forced by climatological QuikSCAT wind stress. The monthly wind-driven surface circulation in winter (February) and summer (July) are shown in Figure 5.5. The wind-driven currents in the Gulf of Tonkin are in the same general direction as the wind. In winter, the northeast monsoon is strong and drives a southward coastal flow entering the gulf through Hainan Strait and flowing along the Vietnam coast. A branch circulates around Hainan Island, enters the gulf from the south, then re-circulates southward along the Vietnam coast. In July, the summer monsoon winds drive almost a negative picture of winter circulation (a weaker one) with coastal flow directed northward along the Vietnam coast and Hainan Island, then leaving the gulf through the Hainan Strait. The magnitude of surface currents is about 10-20 cm/s in winter and about 5 cm/s in summer.

February



July

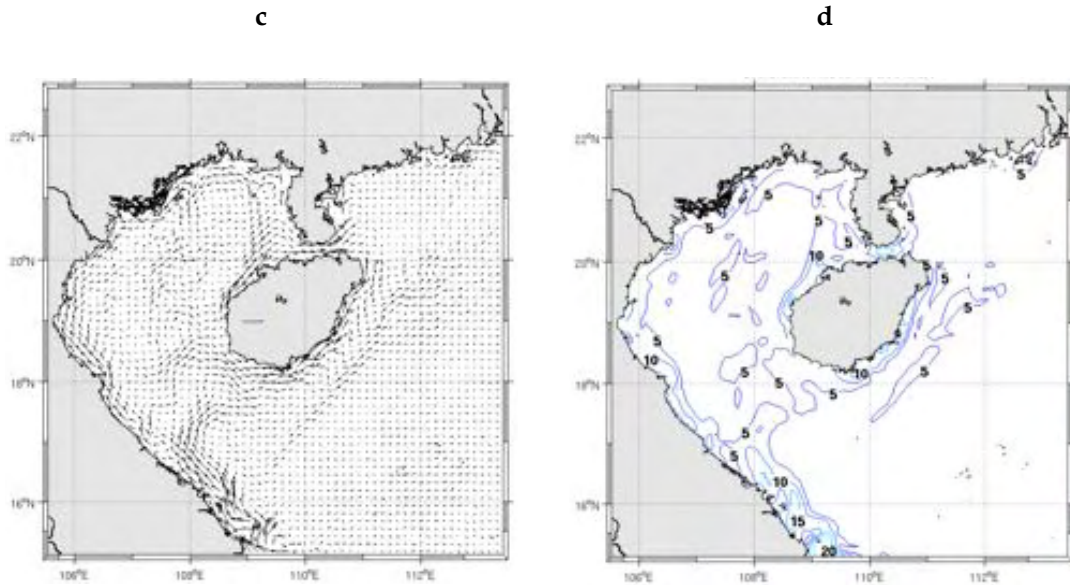


Figure 5.5: Wind-driven flow in the Gulf of Tonkin during winter (February; a: vector, c: contours) and summer (July; b: vector, d: contours).

5.2.2 Density circulation

To understand the impact of density-driven currents, a simulation without wind and tidal forcing is presented. Figure 5.6 shows the monthly mean density-driven surface currents in February and August. The density-driven flow in the Gulf of Tonkin is relatively weak, but the deep-water region is dominated all year long by strong mesoscale eddies generated by instabilities of the geostrophic currents. Observations of the Vietnam East Sea/South China Sea are very limited, especially for the velocity field, but Gan et al. (2006) presented a description of the Vietnam East Sea/South China Sea circulation using satellite remote sensing. They also noted the presence of mesoscale eddies in offshore waters. These eddies are likely to influence the waters of the gulf, but presumably lightly so as the continental slope forms a natural barrier to the geostrophic vorticity generated offshore (topographic stretching of the water column tends to constrain the flow along f/h contours).

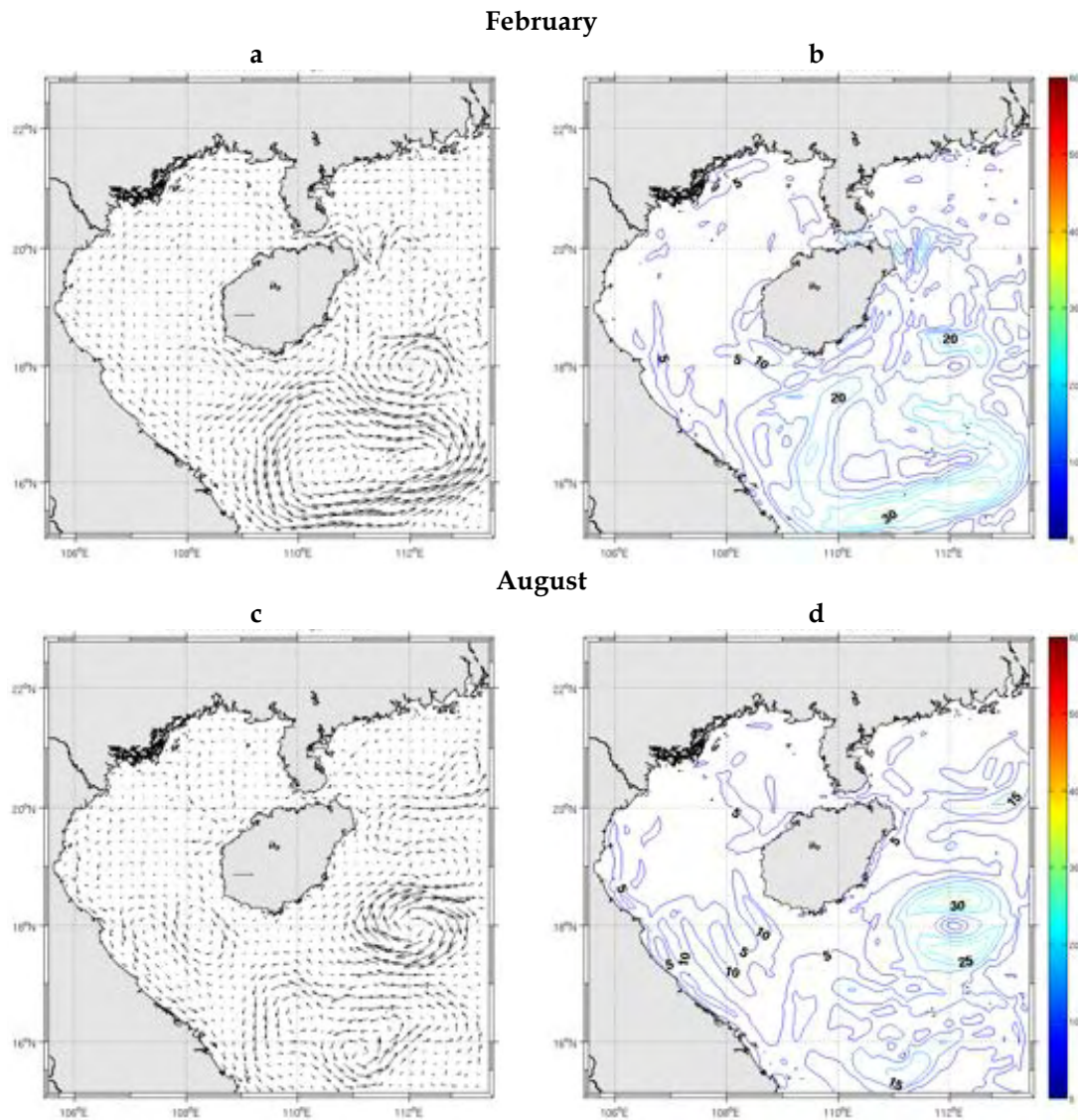


Figure 5.6: Density current in the Gulf of Tonkin during winter (February; a: vector, c: contours) and summer (August; b: vector, d: contours).

5.3 Connectivity to Ha-Long bay

The Lagrangian description of transport is useful for characterizing the dispersion of suspended sediments, fish larvae, chemical pollution, oil spills and other environmental issues. The preservation of Ha-Long Bay is of particular importance to Vietnam. As a first approach to environmental impact assessment of this area, we estimated the origin of mass transport to Ha-Long Bay. We applied a Lagrangian calculation for a domain bounded by 5 vertical sections (Figure 5.7): Ha-Long bay area (section 1), Hainan Strait (section 2) and the southern entrance of the Gulf of Tonkin divided into 3 parts by the 60-m isobath (section 3, 4 and 5). Section 2, 3, 4 & 5 will be referred to as the “departure sections” and section 1 as the “arrival section”. To find the origin of water mass transport across Ha-Long

Bay section, the backward quantitative mode of ARIANE will be applied. It computes the mass transport from the “departure sections” to “arrival section”. The input velocity field is taken from hourly output of 5-year ROMS simulation (see model setting in section 3.2). Long-term calculations ensure that each particle finds its origin at departure sections, that mass conservation is respected and transport is 2D non-divergent. Particles were released in Ha-Long Bay at every grid points and hourly frequency during the whole the 5th year of simulation and their trajectories were integrated backward during the previous 4 years. A total of 2.6 million floats were counted. 85 % were discarded as they travelled back to Section 1. The 15 % particles left is still numerous enough to provide a reliable estimate of transport.

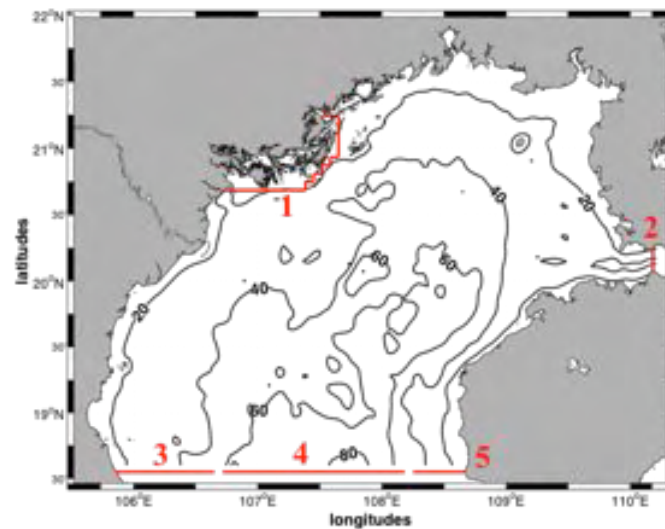
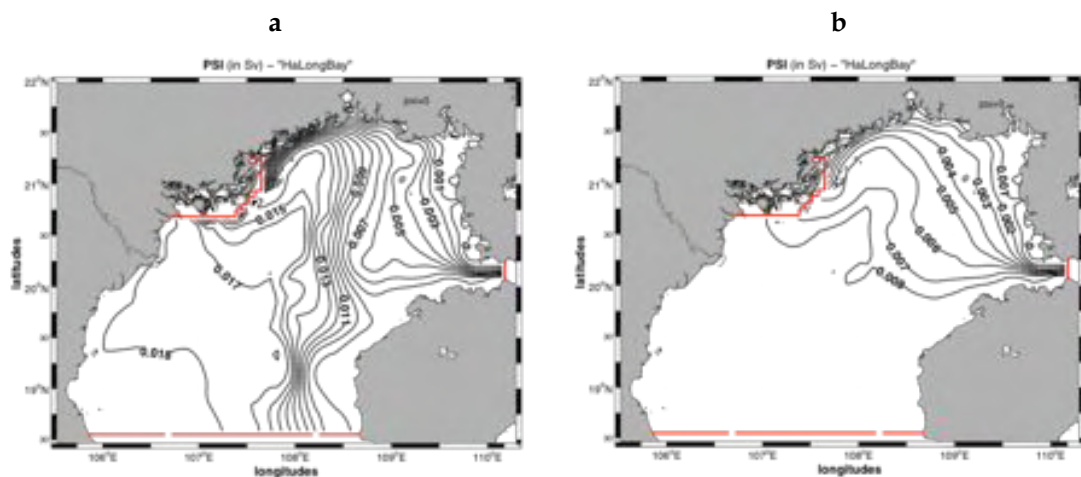


Figure 5.7: Domain used for Lagrangian diagnostic bounded by 5 sections (red lines). The back line represents the isobaths: 20m, 40m, 60m and 80m.



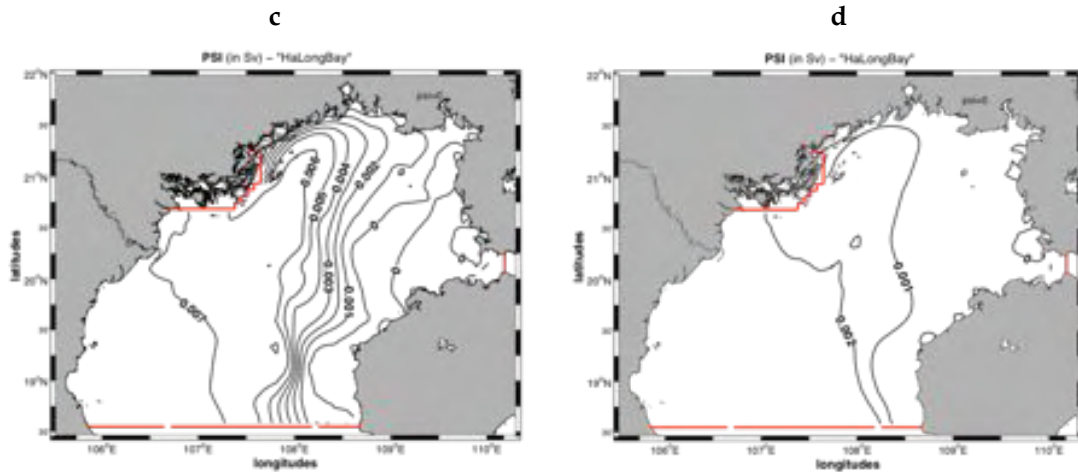


Figure 5.8: Vertically integrated transport [Sv] connecting Ha-Long Bay to (a) the combination of Hainan Strait and southern open boundaries; and their individual contribution: Hainan Strait (b), south-central section 4 (c), south-eastern section 5 (d).

Figure 5.8 shows the contribution of water mass transport from all departure sections and from each of them to Ha-Long bay. Due to the southward direction of transport along the western coast, we find no transport originating from Section 3 in the southwest coastal region. Nearly all particles reach Ha-Long bay by the northeast with dense streamlines concentrating along the coastal isobaths in this region. Most particles originate either from Hainan Strait (46 %) or the south-central Section 4 (42 %) with only 12 % from Section 5 along Hainan Island. Figure 5.9 shows that particles travel faster from Hainan Strait than from the southern sections. 3-4 months of travel are needed to connect the two northern sections, 5-6 months for the meridional connection. We have seen that both tidal and wind-driven residual currents are strong around Hainan Island. The tides provide an anticlockwise path along the northern coast towards Ha-Long Bay (Figure 5.3). However in winter, the winds are not favorable for northward transport, which is confirmed by Figure 5.10. Particles released in winter have almost no chance to reach Ha-Long Bay. The situation is different in summer and fall when wind-driven currents are more favorable and help tidal residuals to transport water properties to the north. We note that Eulerian residuals are much less relevant than Lagrangian residuals to describe tidal property transports in the southern gulf since coherent northward flow is only weak in the Eulerian field. The zonal connectivity between Hainan Strait and Ha-Long Bay is more favorable all year long except during the two summer-monsoon months of June-July (Figure 5.10) that produce eastward currents in the Hainan Strait (Figure 5.5).

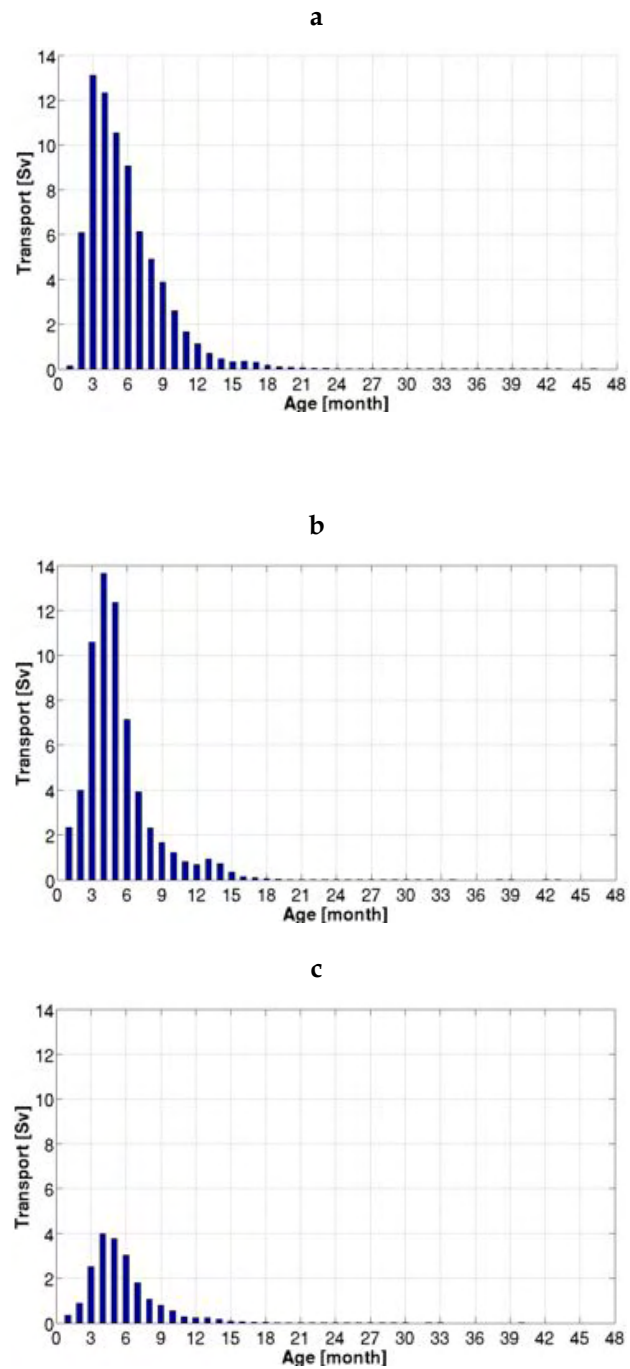


Figure 5.9: Relation of transport to age (duration of time travel) of particles reaching Ha-Long bay from Hainan Strait (a), from section 4 (b) and from section 5 (c).

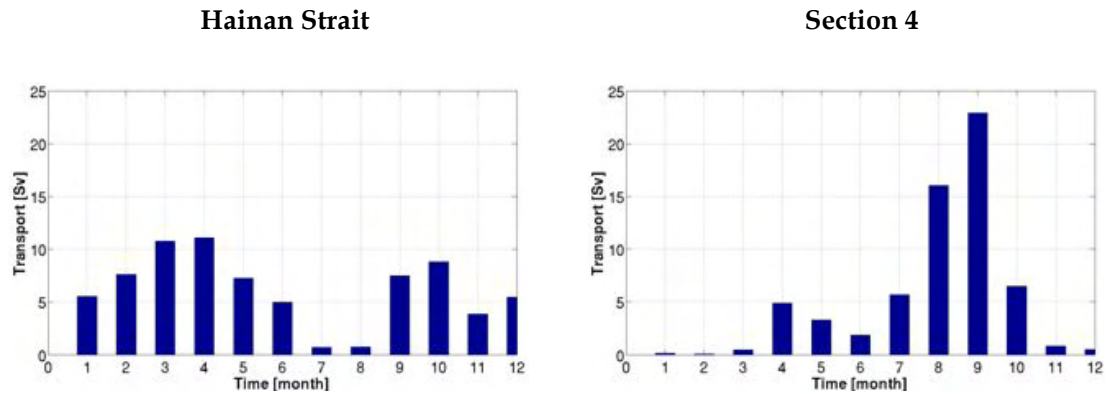


Figure 5.10: Relation of Transport to release time of particles reaching Ha-Long bay from Hainan Strait (a) and from section 4 (b).

5.4 Conclusion

Our estimation of tidal and subtidal residuals confirms that tides are a major forcing of water properties in the Gulf of Tonkin. However, wind forcing is also a strong player in winter when surface currents appear to be controlled by strong northeastern winds. The summer southerly monsoon is weaker and therefore has a weaker (though not negligible) impact on the circulation. Hainan Strait plays an important role all year long (except in June-July) in providing water properties to key regions of the gulf like Ha-Long Bay. This seems in contrast with the convergence of tidal fluxes in this strait but residual circulation is a nonlinear process. Lagrangian tidal residuals are better suited for the interpretation of property transports than Eulerian residuals. This is particularly true for the southern gulf that also provides water properties to the north. On the other end, all forcing leads to a southern transport along the western coast of the gulf, except again in June-July.

Chapter 6: Heat budget

We investigate here the effect of tidal and subtidal circulation on the heat budget of the Gulf of Tonkin. This allows us to revisit previous findings and complement them.

6.1 Coastal cooling in winter

Four numerical experiments are performed to investigate the dynamical factors in the formation of a cool coastal tongue observed during winter in and around the Gulf of Tonkin. In all cases, the model is started from rest with initial temperature and salinity from monthly COADS climatology and is integrated for 2 years. Experiment EXP1 only considers the role of surface heat and freshwater fluxes (no wind or tidal forcing). EXP2 considers the effect of tidal forcing in addition to surface buoyancy fluxes. The eight main tidal components (K1, O1, M2, S2, P1, Q1, N2, K2) are used. Wind forcing is added to surface buoyancy forcing in experiment EXP3. All forcing are finally incorporated in experiment EXP4 (model settings described in section 3.2).

In Figure 6.1, the mean February sea surface temperature (SST) map from EXP4 is compared to the equivalent AVHRR February climatology. The satellite data is derived from harmonic fit analysis of 5-day averaged 4-km AVHRR Pathfinder Version 5.0/5.1 SST data for 1982-2008 (Casey et al., 1999). The model with full forcing (EXP4) reproduces the main SST features in the Gulf of Tonkin in winter but has a cold bias of about 1 degree. This bias can be attributed to many things including interannual variability and model surface forcing biases. Nevertheless, the simulations are suitable for analyzing the formation of coastal cold water. The latter has a maximum intensity over the gulf in February. It extends north and south of the gulf and through the Hainan strait. EXP1 (Figure 6.2a) reveals the important role that surface heat fluxes play in winter coastal SST. During winter, the absorbed short-wave solar radiation decreases while heat loss from the ocean to the atmosphere through evaporation (latent heat) increases. The net heat flux is negative in most of the gulf (Figure 3.2a) and cools the ocean. Shallow waters are more intensely cooled than deep waters because deep waters have a larger reservoir of subsurface waters to mix with. SST differences between simulations with and without wind forcing (EXP3 & EXP1); with and without tidal forcing (EXP2 & EXP1) are represented in Figure 6.3. The wind stress appears as a most important agent in transporting cold water southwards along the western side of the Gulf (Figure 6.2b and 6.3a). However, the wind and tides both have a warming effect on the eastern side of Qiongzhou peninsula and Hainan Island by advecting warmer water from the north. Tidal forcing also has a warming effect in the western sides of Leizhou peninsula and Hainan Island through northward advection.

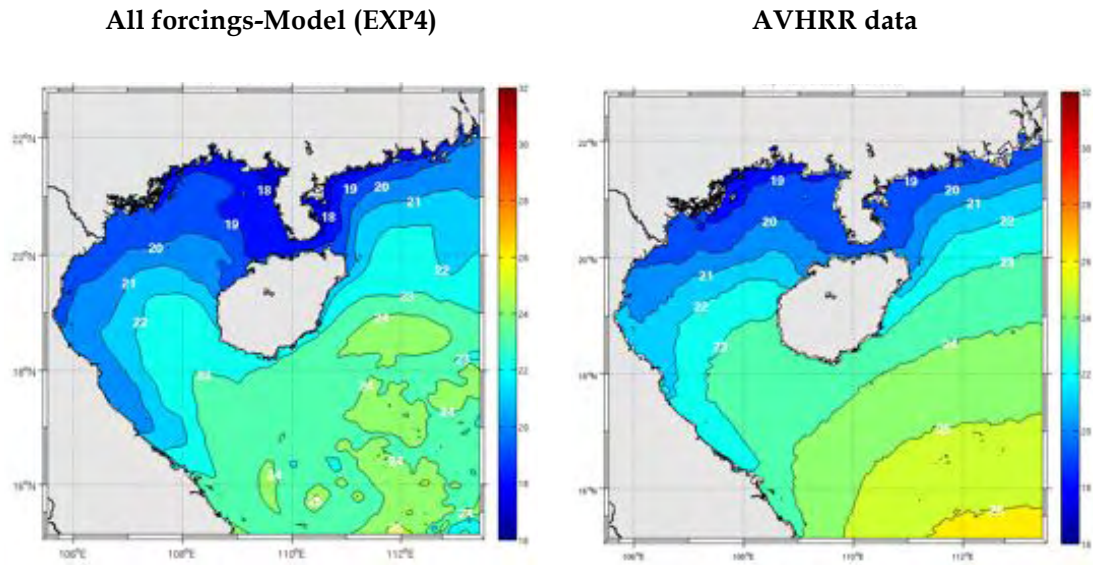


Figure 6.1: February SST [°C] in experiment EXP4 (left) and AVHRR Pathfinder (right).

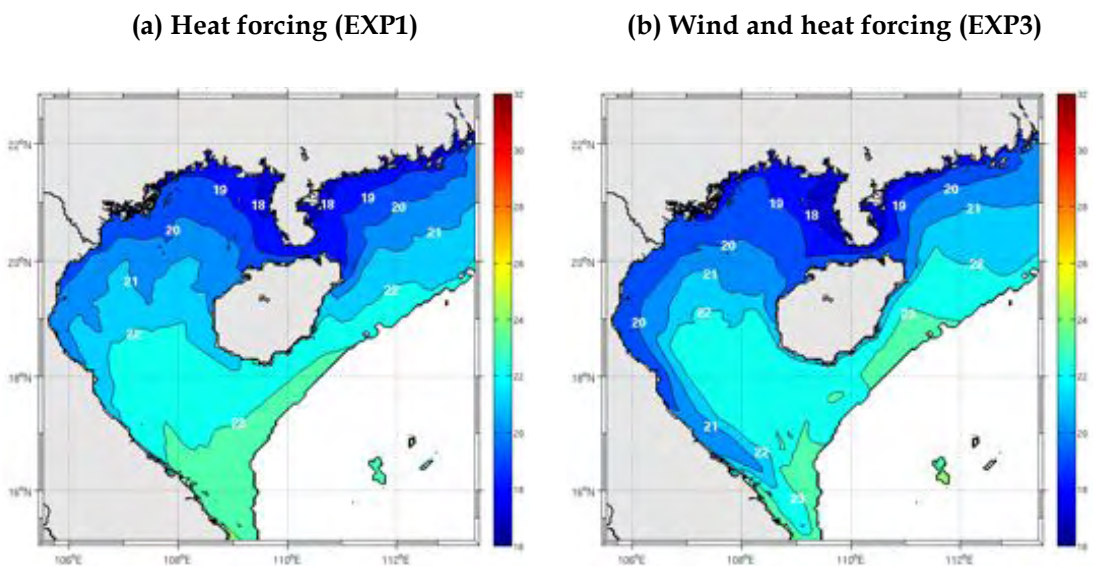


Figure 6.2: February SST [°C] in experiments EXP1, EXP3. The oceanic zone deeper than 200 m is not shown.

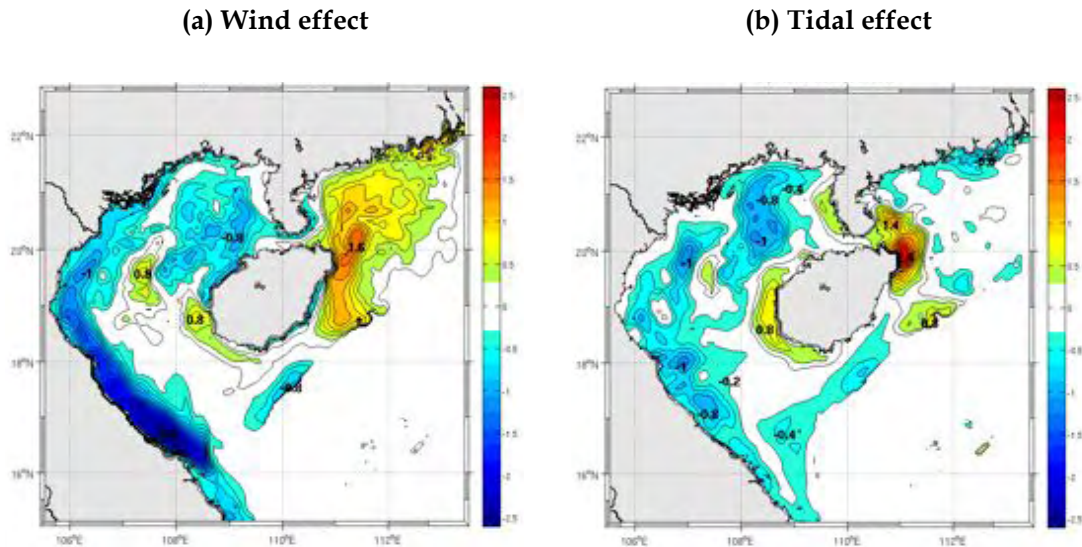


Figure 6.3: (a) February SST difference [$^{\circ}\text{C}$] between EXP3 and EXP1 (with and without wind forcing); (b) between EXP2 and EXP1 (with and without tides forcing); contour interval 0.2 degree. The oceanic zone deeper than 200 m is not shown.

6.2 Frontogenesis in spring-summer

Studies on the chlorophyll-a (Chl-a) distributions in the Gulf of Tonkin using SeaWiFS-derived Chl-a data indicate that high Chl-a zones exist along the coast, in the Hainan Strait and near the southwestern coast of the Hainan Island (Tang et al., 2003; Suhung et al., 2008). Surface Chl-a fronts are formed narrowly adjacent to these high Chl-a zones. Chlorophyll-a concentrations are an indicator of phytoplankton abundance and biomass in coastal and estuarine waters. Figure 6.4 presents April and August Chl-a concentrations based on a 12-year SeaWiFS climatology. As already noticed by Suhung et al. (2008), this figure shows the occurrence of spring and summer phytoplankton blooms along the coast of northern Vietnam and southern China, including the Gulf of Tonkin. Hu et al. (2003) used the three-dimensional numerical model POM to explore the physical mechanisms involved in the formation of fronts around the Hainan Island that could explain the Chlorophyll observations. Turbulent mixing is recognized as a critical factor for the growth and persistence of natural populations of phytoplankton in lakes and oceans (George and Heaney, 1978; Reynolds, 1984; Thomas and Gibson, 1990a,b). Tidal mixing in particular provides one of the most important processes for nutrient availability in the euphotic zone (where primary production occurs) through nutrient regeneration. Hu et al. (2003) used the h/u^3 criterion proposed by Simpson and Hunter (1974) to indicate frontal positions (h is depth and u is the depth-mean tidal current amplitude). In the Gulf of Tonkin, the location of contour lines $\log(h/u^3)=2.9\sim 3.0$ is at some locations almost coincidental with the Chl-a front detected by SeaWiFS and was thus considered by Hu et al. (2003) as the tidal frontal position separating productive coastal waters from poor offshore waters. However, we remark that in some instances the coincidence of tidal fronts predicted by the $\log(h/u^3)$ criterion with Chl-a concentrations is not as

good. In the middle of the gulf where tidal currents are weaker, high Chl-a concentrations can still be observed, especially in spring.

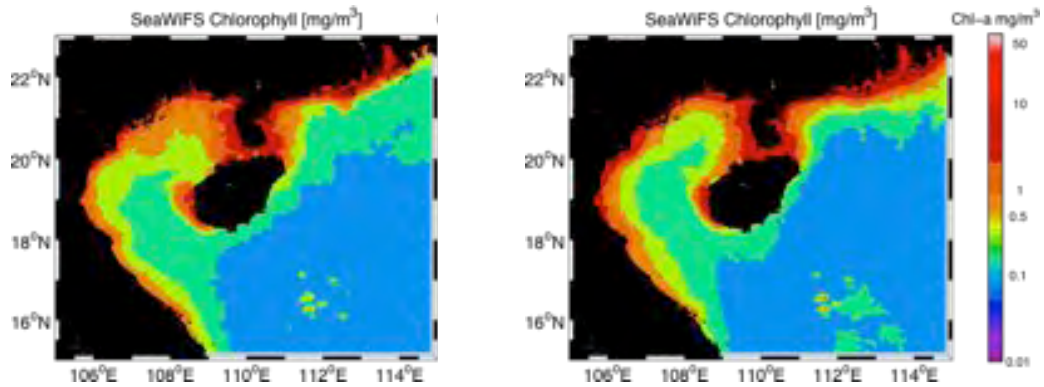


Figure 6.4: SeaWiFS monthly climatology of Chl-a concentrations from 1998 to 2010. (a) April, (b) August. The unit of Chl-a concentration is in mg/m^3

In this section, we will complement our understanding of the physical processes explaining high Chl-a concentrations in the Gulf of Tonkin and around the Hainan Island throughout the year, particularly during spring and summer months. During the winter months, the coastal ocean cools down rapidly in the shallow Gulf of Tonkin (mainly resulting from reduced incoming solar radiation). As the ocean surface cools below the temperature of subsurface water, it becomes denser and mixes by convective instability. On the contrary, the gulf becomes density stratified during summer with warm water at the surface and cooler water beneath. Considerable mixing energy is then needed to overcome the stable stratification. This energy may come from wind or tides and it is doubtful that only the tides are strong enough to generate well-mixed coastal areas in the Vietnam East Sea/South China Sea. We will concentrate here on the mixing process occurring in and around the Gulf of Tonkin during spring and summer and compare it to Chl-a concentration.

Mixing areas are investigated by an assessment of temperature changes through vertical mixing in the temperature budget equation, which was computed online in ROMS. The equation integrated over the time-varying mixed layer depth (MLD) and monthly-averaged is:

$$\underbrace{\frac{\partial \langle T \rangle}{\partial t}}_{\text{Tendency}} = \underbrace{\left\langle -u \frac{\partial T}{\partial x} - v \frac{\partial T}{\partial y} - w \frac{\partial T}{\partial z} \right\rangle}_{\text{Advection}} + \underbrace{\langle Dh_T \rangle}_{\text{Horizontal_Mix}} + \underbrace{\left\langle \frac{\partial}{\partial z} \left[K_v \frac{\partial T}{\partial z} \right] \right\rangle}_{\text{Vertical_Mix}} + \underbrace{Q_o - Q_s(z = \text{MLD})}_{\text{Forcing}} - E \quad (6.1)$$

T is the temperature, (u,v,w) are the zonal, meridional and vertical velocity component, K_v is the vertical mixing coefficient and Dh is the lateral diffusion term. MLD is taken as the planetary boundary layer depth in KPP (K-profile parameterization) scheme. Q_o is the total atmospheric forcing at the surface and Q_s is the solar radiation component that reaches the mixed layer depth. E is the entrainment-detrainment term.

The averaged vertical mixing term in the budget equation was calculated in EXP2, EXP3 and EXP4. The results for April and August are presented in Figure 6.5. The tides cause strong mixing through the Hainan Strait, the western Hainan Island and along the eastern and western coasts of the Leizhou Peninsula. The tidal currents are strong in these areas and are able to stir up water from the lower layers. However, these high mixing areas remain confined within a few kilometers from the coast in shallow water, consistent with the h/u^3 criterion study of Hu et al. (2003). From the simulation with wind forcing, the mixed area is found further offshore along the Chinese and Vietnamese coasts where tidal currents are not strong enough to stir up the whole water column. Wind mixing appears thus as an important additional mechanism to explain the observations. In spring when the wind is still strong, high Chl-a concentrations extend over waters of about 50 m as wind works in combination with tides. In August, when the wind is at a minimum, there is a better fit between the area of tidal mixing and high Chl-a concentration. Even then, wind mixing can still be an active player.

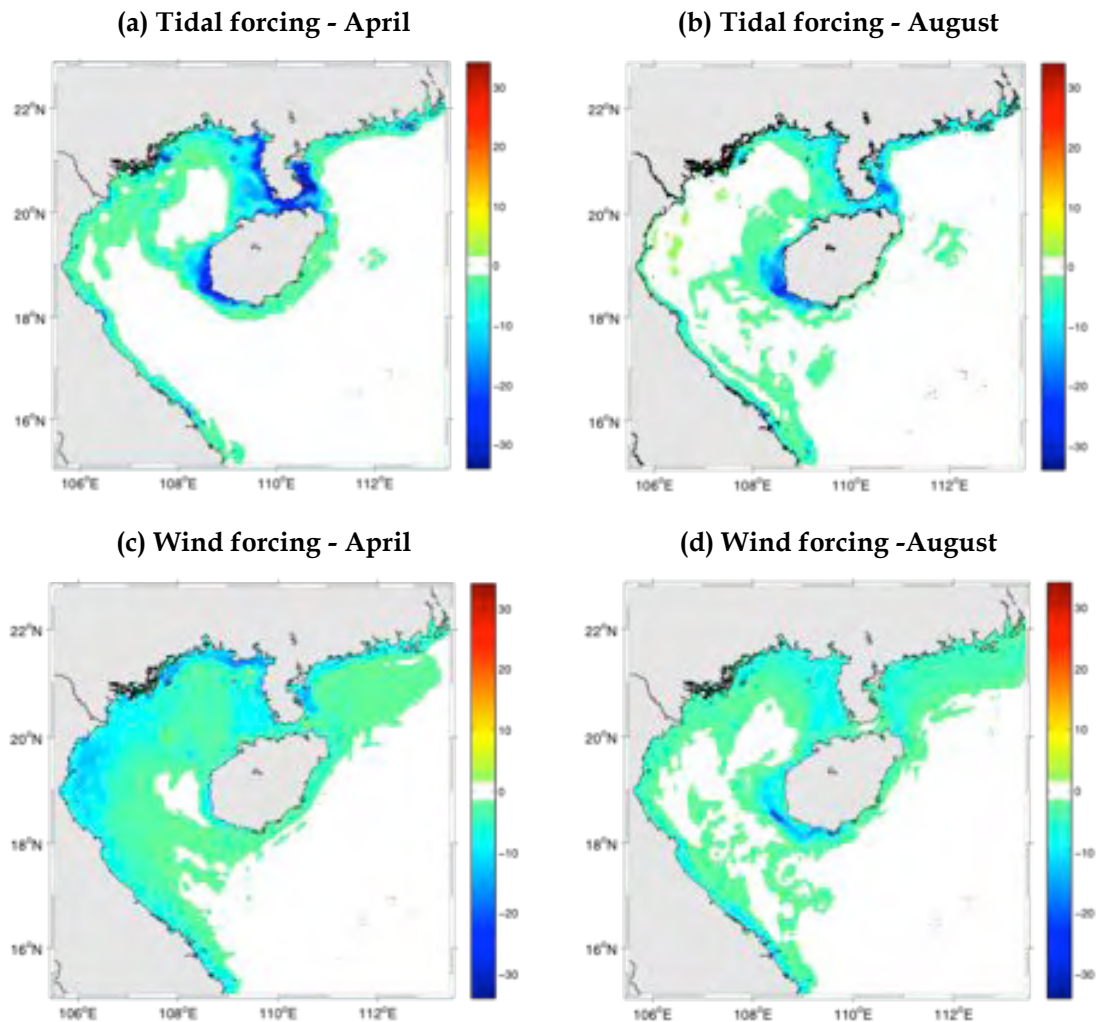


Figure 6.5: Vertical mixing in April and August in the mixed layer heat budget for EXP2 (a&b), and EXP3 (c&d). Negative values represent cooling.

Conclusion

ROMS is found to reproduce the tides of the Gulf of Tonkin with improved accuracy over the existing state of the art. The model errors are estimated by a compilation of all available tide gauge measurements along the coast and from ten satellite-altimeter ground-tracks data specifically reprocessed for coastal oceanography. Another specificity of our satellite data set is that it contains 6 ground tracks of 5-year TOPEX-Jason-1 interleaved data that increases the number of measurement locations and brings significant sample improvement in key areas like the Hainan Strait. On the other hand, it reduces the reliability of semidiurnal tides (particularly M2 amplitude and S2 phase) due to its limited time series. Nevertheless, the combination of 16-year primary data and 5-year interleaved data provide the best data set available to date for the Gulf of Tonkin, which is dominated by diurnal tides.

The model-data comparison shows good results near the open boundaries of the computational domain implying that the TPXO tidal product provides adequate forcing for our model. Model-data differences increase significantly near shallow coastal regions. There are two possible reasons for this. First, model errors may increase near the coast due to bathymetric and bottom roughness uncertainties that have a larger impact in shallow water. The lowest RMS errors were obtained with a choice of low values for drag coefficients and bottom roughness, which is consistent with the fact that the bottom of the gulf is made of fine sediments (Ma et al., 2010). In addition, the choice of a logarithmic drag profile appears crucial in 3D simulations to reproduce bed shear stress distribution and magnitude as it accounts for the increased vertical resolution in shallow water. In future studies, spatial variability of the bottom roughness length could be calculated using data assimilation techniques. The second source of discrepancy between model and data is the loss of quality of satellite altimetry measurements near the coastline due to land contamination and inaccurate geophysical corrections. A comparison between satellite and tide gauge data provides an observational error estimate, which appear to fall within model-data differences.

The validation of our model allows us to review the analysis of tidal characteristics in the Gulf of Tonkin. We used the model to explore for the first time the resonance spectrum of the gulf. Uncertainties in the damping process may alter our resonance analysis, but it provides consistent results with theoretical models and observations. It shows the three modes of resonance consistent with those expected from the idealized rectangular bay model with constant slope, with resonance peak at periods: 29 h, 12.5 h and 8 h. The rectangular bay model with constant depth used previously by several authors for the Gulf of Tonkin is thus disqualified. The latter model wrongly places O1 at the peak period of mode 0 and predicts no semi-diurnal resonance. Our results suggest that semi-diurnal tides are resonant at mode 1 but they are small in the Gulf because that they are already small in the Vietnam East Sea/South China Sea. On the contrary, diurnal tides are large in the Vietnam East Sea/South China Sea because of Helmholtz resonance (Zu et al., 2008) involving Luzon Strait as the main opening for tidal energy flux in this basin. Then, it appears that O1 amplitude is larger in the gulf than K1 because

of a larger resonant effect (O1 is closer to the resonant peak period of 29 hours), even though its amplitude in the Vietnam East Sea/South China Sea is smaller than K1.

Next, we explored the residual tidal flow. The strongest residual currents are found in the Hainan Strait (~ 20 cm/s flowing inside the gulf) and western Hainan Island (~ 8 cm/s). We show that the Hainan strait is a convergence zone for tidal energy flux that leaves little energy entering or escaping the Gulf. Nevertheless, it is there that residual currents are largest with consequences for the transport of water properties inside the gulf. The Hainan Strait is also a region of strongest energy dissipation with consequences for tidal mixing. Along the western coast of the gulf, residual currents are much weaker and only reach a maximum of 2 cm/s around headlands. These may be underestimated by the low resolution of local coastal morphology. A residual streamfunction was computed that reveals a coherent anticlockwise transport pattern around Hainan Island with maximum in the middle of the gulf. The Lagrangian flow appears qualitatively close to the Eulerian flow but weaker, as a result of the clockwise rotation of tidal ellipses in the gulf.

The tidal residuals can be locally strong but weaker in average than wind-driven currents, especially during the winter monsoon season. This has potential implications for transport properties too. In addition, the wind stress has a larger impact than expected from previous studies on vertical mixing. We showed in the last part of this study that it is the combination of winds and tides that can explain the location of seasonal fronts in the Gulf of Tonkin. It suggests that the study of primary production in this region should include a realistic set of forcing. The present model appears adequate for such applications in the fields of biogeochemistry and sediment transport. However, further investigation should be made at smaller scales where erosion and transport properties can be properly addressed. Our understanding is that an effort should then be made to achieve high resolution bathymetry and better acknowledge the diversity of bottom sediment type and its impact on the bottom boundary layer dynamics.

References

- Arbic B.K. and R.B. Scott, 2007: On quadratic bottom drag, geostrophic turbulence and oceanic mesoscale eddies. *Journal of physical oceanography*, 38, 84-102.
- ARGOSS, 2001: Clams: An online offshore climate assessment tool. Argoss, Vollenhove, the Netherlands.
- Barnier B., L. Siefridt and P. Marchesiello, 1995: Surface thermal boundary condition for a global ocean circulation model from a three-year climatology of ECMWF Analyses, *Journal Marine Systems*, 363-380.
- Beckmann, A., and D. B., Haidvogel, 1993: Numerical simulation of flow around a tall isolated seamount. Part I: Problem formulation and model accuracy. *J. Phys. Oceanogr.*, 23, 1736-1753.
- Blanke, B., and S., Raynaud, 1997: Kinematics of the Pacific Equatorial Undercurrent: a Eulerian and Lagrangian approach from GCM results. *J. Phys. Oceanogr.*, 27, 1038-1053.
- Blanke, B., M., Arhan, S., Speich, and G., Madec, 1999: Warm water paths in the equatorial Atlantic as diagnosed with a general circulation model. *J. Phys. Oceanogr.*, 29, 2753-2768.
- Blayo, E. and L., Debreu, 1999: Adaptive mesh refinement for ocean modeling: first experiments. *J. Physical Oceanography*, vol. 29, 1239-1250.
- Cai S., X. Long, H. Liu and S. Wang, 2005: Tide model evaluation under different conditions, *Continental Shelf Research* 26, pp. 104-112.
- Campbell, J.W., J.M. Blaisdell and M. Darzi. 1995: Level-3 SeaWiFS data products: spatial and temporal binning algorithms. *SeaWiFS Technical Report Series, NASA Technical Memorandum 104566, Vol. 32. Goddard Space Flight Center, Greenbelt, Maryland.*
- Casey K.S. and P. Cornillon, 1999: A comparison of satellite and in-situ based sea surface temperature climatologies. *J. Clim.*, 12, 1848-1863.
- Chen C., P. Li, M. Shi, J. Xuo, M. Chen, H. Sun, 2009: Numerical study of the tides and residual currents in the Qiongzhou Strait. *Chinese. Journal of Oceanology and Limnology*, 27 (4), 931-942.
- Clark A.J., Battisti D.S., 1981: The effect of continental shelves on tides, *Deep Sea Res.*, 28A, 665-682.
- Conkright M.E., Locarnini R. A., Garcia H.E., O'Brien T.D., Boyer T.P., Stephens C., Antonov J.I., 2002: *World Ocean Atlas 2001: objective analyses, data statistics, and figures*, CD-ROM documentation. Technical report. National Oceanographic Data Center, Silver Spring, MD.

- Da Silva, A.M., Young C.C. , Levitus S., 1994: Atlas of surface marine data 1994, volume 1, algorithms and procedures, 74 pp., NOAA Atlas NESDIS 6. U. S. Department of Commerce, NOAA, NESDIS, USA.
- Debreu, L., P. Marchesiello, P. Penven, and G. Cambon, 2012: Two-way nesting in split-explicit ocean models: algorithms, implementation and validation. *Ocean Modelling*, 49-50, 1-21.
- Denman, K. L. and Gargett, A. E., 1983: Time and space scales of vertical mixing and advection of phytoplankton in the upper ocean. *Limnol. Oceanogr*, 28:801-815.
- Đinh Văn Ưu, 2008: Thủy văn và động lực biển Đông, Đại học Quốc Gia Hà Nội.
- Do Minh Duc, Mai Trong Nhuan, Chu Van Ngoi, Tran Nghi, Dao Manh Tien, Tj.C.E. van Weering, G.D. van den Bergh, 2007: Sediment distribution and transport at the nearshore zone of the Red River delta, Northern Vietnam, *J. Asian Earth Sciences*, 29, 558-565.
- Doodson, A. T., and H. D., Warburg, 1941: Admiralty manual of tides, Hydrographic Department, Admiralty, Her Majesty's stationary office, London.
- Egbert G.D., Erofeeva S.Y., 2002: Efficient inverse modeling of barotropic ocean tides. *J. Atmos. Ocean. Technol.*, 19, 183-204.
- Fairall, C. W., Bradley, E. F., Hare, J. E., Grachev, A. A., Edson, J. B., 2003: Bulk parameterization of air-sea fluxes: updates and verification for the COARE algorithm. *Journal of climate*, 16, 571-591.
- Fang G., Kwok Y. K., Yu K. & Zhu Y., 1999: Numerical simulation of principal tidal constituents in the South China Sea, Gulf of Tonkin and Gulf of Thailand. *Continental Shelf Research* 19, pp. 845-869.
- Flather, R. A., 1976: A tidal model of the northwest European continental shelf. "Memories de la Societe Royale de Sciences de Liege", 6, 141-164.
- Feng, S., 1987: A three dimensional weakly nonlinear model of tide-induced Lagrangian residual current and mass transport, with an application to the BoHai sea. Three-dimensional models of marine and estuarine dynamics, In: Nihoul, J. C. J., and Jamart, B. M. eds, Elsevier Oceanography Series 45: Elsevier, p. 471-488.
- Foreman, M. G. G., R. F. Henry, 1993: A Finite Element Model for Tides and Resonance Along the North Coast of British Columbia. *J. Geophys. Res.*, 98 (C2), 2509-2531.
- Gan, J. P., Li, H., Curchitser, E. N., Haidvogel, D. B., 2006: Modeling South China Sea circulation: response to seasonal forcing regimes. *J. Geophys. Res.* 111, C06034. Doi: 10.1029/2005JC003298.

Garrett, C., 2004: Program of Study: Tides, Lecture 9. Technical report, Woods Hole Oceanographic Institution, MA.

George, D. G., Heaney, S. I., 1978: Factors influencing the spatial distribution of phytoplankton in a small productive lake. *J. Ecol.* 66: 133-155.

Gondin, G., 1972. *The Analysis of Tides*. Liverpool University Press.

Haney, R. L., 1991: On the pressure gradient force over steep topography in sigma coordinate ocean models. *J. Phys. Oceanogr.*, 21, 610-619.

Hirai, Y., Nguyen, V.L., Ta, T.K.O, 2008: Assessment of impacts of sea level rise on Tam Giang-Cau Hai Lagoon area based on geomorphological survey map. Regional views, *Chiikigaku kenkyu*. Institute for applied geography, Komazawa University, no 21, p. 1-8.

Hu, J.Y., Kawamura, H., Tang, D. L., 2003: Tidal front around the Hainan Island, northwest of the South China Sea. *Journal of Geophysical Research*. Vol. 108, No. C11.

Jonsson, B., K. Doos, J. Nycander, and P. Lundberg, 2008: Standing waves in the Gulf of Finland and their relationship to the basin-wide Baltic seiches, *J. Geophys. Res.*, 113, C03004.

Large, W.G., MacWilliams J.C. Doney S.C., 1994: Oceanic vertical mixing a review and a model with a nonlocal boundary layer parameterization, *Rev. Geophys.*, 32, 363-403.

Lefebvre J.P., Ouillon S., Vu Duy Vinh, Arfi R., Panche J.Y., Mari X., Chu Van Thuoc, Torretton J.P., 2012: Seasonal variability of cohesive sediment aggregation in the Bach Dang-Cam Estuary, Haiphong (Vietnam), *Geo-Marine Letters*, 32 (2), 103-121.

Le T.P.Q., J. Garnier, B. Gilles, T. Sylvain, Chu V.M, 2007: The changing flow regime and sediment load of the Red River, Vietnam. *Journal of Hydrology*. Vol. 334, 199-214.

Lemarié F., L. Debreu, A. Shchepetkin, J.C. McWilliams, 2012: On the Stability and Accuracy of the harmonic and biharmonic isoneutral mixing operators in oceanmodels. *Ocean Modelling*. 52-53, 9-35.

Levitus, S., *Climatological Atlas of the World Ocean*, 1982: Professional Paper 13, 173 pp., NOAA, USA.

Longuet-Higgins M.S., 1969: On the transport of mass by time-varying ocean currents. *Deep sea Res.*, 16431-447.

Lyard, F., Lefevre, F., Letellier, T., Francis, O., 2006: Modelling the global ocean tides: modern insights from FES2004. *Ocean Dynamics*, 56, 394-415.

- Ma, F., Wang, Y., Li, Y., Ye, C., Xu, Z., Zhang, F., 2010: The application of geostatistics in grain size trend analysis: A case study of eastern Beibu Gulf. *J. Geogr. Sci.*, 77-90.
- Manh D.V., Yanagi T., 2000: A study of residual flow in the Gulf of Tongking. *J. Oceanography*, 56, 59-68.
- Marchesiello, P., J. C. McWilliams, and A. Shchepetkin, 2001: Open boundary condition for long-term integration of regional oceanic models. *Ocean Modelling* 3, 1-20.
- Marchesiello, P., L. Debreu, and X. Couverlard, 2009: Spurious diapycnal mixing in terrain-following coordinate models: the problem and a solution. *Ocean Model.* 26: 156-169. Doi:10.1016/j.ocemod.2008.09.004
- Mei, C. C., 1989: *The Applied dynamics of ocean surface waves*. World Scientific.
- Munk, W., D. E., Cartwright, 1966: Tidal spectroscopy and prediction. *Phil Trans R. Soc. London. A* 259: 533-581.
- Navarro P., Amouroux D., Duong Thanh Nghi, Rochelle-Newall E., Ouillon S., Arfi R., Chu Van Thuoc, Mari X., Torrèton J.P., 2012: Butyltin and mercury compounds fate and tidal transport in waters of the tropical Bach Dang estuary (Haiphong, Vietnam), *Marine Pollution Bulletin*, 64, 1789-1798.
- Nguyễn Ngọc Thụy, 1984: *Thủy triều vùng biển Việt Nam*. Nxb KHKT, Hà Nội.
- Pairaud, I. L., Lyard, F., Auclair, F., Tetellier, T., Marsaleix, P., 2008: Dynamics of the semi-diurnal and quarter-diurnal internal tides in the Bay of Biscay. Part 1: Barotropic tides. *Continental shelf research*. Vol. 28., pp. 1294-1315.
- Penven, P., Marchesiello, P., Debreu, L., Lefevre, J. 2008: Software tools for pre- and post-processing of oceanic regional simulations. *Environmental Modeling & Software*, 23, 660-662.
- Rabinovich, A.B., 2009: Seiches and harbour oscillations. In: *Handbook of Coastal and Ocean Engineering* (ed. Y.C. Kim) (World Scientific, Singapore), 193-236.
- Reynolds, C. S. 1984: *The Ecology of Freshwater Phytoplankton*. Cambridge University Press, Cambridge, 436 pp.
- Roblou L., F. Lyard, M. Le Hénaff, C. Maraldi, 2007: X-TRACK, A new processing tool for altimetry in coastal oceans, *Proc. ENVISAT Symposium*, Montreux, Switzerland.
- Roblou L., J. Lamouroux, J. Bouffard, F. Lyard, M. Le Hénaff, A. Lombard, P. Marsaleix, P. De Mey and F. Birol, 2011: Post-processing altimeter data toward coastal applications and integration into coastal models. Chapter 9 in S. Vignudelli, A.G. Kostianoy, P. Cipollini, J. Benveniste (eds.), *Coastal Altimetry*, Springer Berlin Heidelberg.

- Schureman, P., 1971: Manual of harmonic analysis and prediction of tides, U. S. Coast and Geodetic Survey.
- Schwiderski, E. W., 1980: On charting global ocean tides. *Rev. Geophys. Space Phys.*, 18, pp. 243-268.
- Shchepetkin, A. F. and J. C. McWilliams, 1998: Quasi-monotone advection schemes based on explicit locally adaptive dissipation, *Monthly Weather Rev.*, 126, pp. 1541-1580
- Shchepetkin, A.F. and J.C. McWilliams, 2003: A method for computing horizontal pressuregradient force in an oceanic model with a nonaligned vertical grid. *J. Geophys. Res.*, 108, (C3), doi:10.1029/2001/JC001047.
- Shchepetkin, A.F. and J.C. McWilliams, 2005: The regional oceanic modeling system (ROMS): a split explicit, free-surface, topography-following-coordinate oceanic model. *Ocean Modeling*, 9, 347-404.
- Simpson, J. H., and Hunter, J. R. 1974: Fronts in the Irish Sea. *Nature*. Vol. 250, 404-406.
- Smith, W.H. F., and D. T. Sandwell, 1997: Global seafloor topography from satellite altimetry and ship depth soundings, *Science*, 277, 1957-1962.
- Song, Y. and D. B. Haidvogel, 1994: A semi-implicit ocean circulation model using a generalized topography-following coordinate system. *J. Comp. Phys.*, 115, 228-244.
- Suhung, S., Gregory G. L., James G. A., Zuojun, Y. and Steven J. K. 2008: Seasonal Variations of Chlorophyll a Concentration in the Northern South China Sea. *IEEE geoscience and remote sensing letters*, 5 (2), pp. 315-319.
- Sutherland, G., C. Garrett and M. Foreman, 2005: Tidal resonance in Juan de Fuca Strait and the Strait of Georgia. *J. Phys. Oceanogr.*, 35, 1279-1286.
- Tang, D. L., Ni, I. H., Muller-Karger, F. E. and Liu, Z. J., 1998: Analysis of annual and spatial patterns of CZCS-derived pigment concentrations on the continental shelf of China, *Cont. Shelf Res.*, 18, 1493-1515.
- Taylor, G. I., 1922: Tidal oscillations in gulfs and rectangular basins. *Proc Lond Math Soc* 20(1):148-181.
- Thanh T.D., Saito Y., Huy D.V., Nguyen V.L., Ta T.K.O., Tateishi M., 2004: Regimes of human and climate impacts on coastal changes in Vietnam, *Reg. Envir. Change*, 4, 49-62.
- Thomas, W. H., and C. H., Gibson, 1990a: Effects of small-scale turbulence on microalgae. *J. Appl. Phycol.* 2: 71-77.

- Thomas, W. H., and C. H., Gibson, 1990b: Quantified small-scale turbulence inhibits a red tide dinoflagellate *Gonyaulax polyedra* Stein. *Deep-Sea Res.* 37: 1583-1593.
- Van Dantzig, D., and H. A. Lauwerier, 1960: The North Sea problem. iv. Free oscillations of a rotating rectangular sea, *Proc. K. Ned. Acad. Wet., Ser. A. Math Sci.*, 64, 339-354.
- Van Maren, D. S., Hoekstra, P., and Hoitink, A. J. F., 2004: Tidal flow asymmetry in the diurnal regime: bed-load transport and morphologic changes around the Red River Delta. 54, 424-434.
- Wyrtki K., 1961: Scientific Results of marine Investigations of the South China Sea and the Gulf of Thailand 1959-1961. NAGA report - Volume 2.
- Yang Haijun, Liu Qinyu and Jia Xujing, 1999: On the Upper Oceanic heat Budget in the South China Sea: Annual Cycle, *Advances in Atmospheric Sciences*, Vol. 16 No. 4
- Zimmerman, J.T.F., 1980: Vorticity transfer by tidal currents over an irregular topography. *J. Mar. Syst.*, 38:601-630.
- Zu T. J. Gan, S.Y. and Erofeeva, 2008: Numerical study of the tide and tidal dynamics in the South China Sea, *Deep-Sea Research I* 55, pp. 137 - 154.

RESUMÉ

Caractéristiques des marées dans le Golfe du Tonkin

Le Golfe du Tonkin, située dans la mer de l'Est/la mer de Chine du Sud, est une zone de fort intérêt écologique, touristique et économique. Améliorer notre connaissance de ses processus hydro-sédimentaires (transport de particules en suspension) est d'une grande importance pour le développement durable de cette région. L'objectif scientifique de cette étude est de revoir les processus physiques dominants qui caractérisent la dynamique des marées dans le Golfe du Tonkin en utilisant un modèle à haute résolution et la combinaison de toutes les données disponibles. Une attention particulière est donc accordée à un examen croisé du modèle, des marégraphes et de l'altimétrie côtière, ainsi qu'à l'étalonnage du modèle dérivé d'un ensemble d'expériences de sensibilité aux paramètres. Sur cette base, le bilan d'énergie de la marée du golfe est analysé et ses propriétés de résonance sont évaluées et comparées avec les modèles idéalisés et observations. Ensuite, la circulation résiduelle eulérienne et la dérive Lagrangienne de marée sont évaluées et son effet sur le mélange est illustré.

Le modèle de marée utilisé dans cette étude est ROMS (*Regional Oceanic Modeling System*). On montre tout d'abord qu'il reproduit les marées du Golfe du Tonkin avec une précision supérieure à l'état actuel de l'art. Les erreurs du modèle sont estimées par la compilation des toutes les mesures disponibles à partir des marégraphes disposés le long de la côte Vietnamiennne et Chinoise et d'une dizaine de traces au sol de données altimétriques satellitaires spécifiquement retraitées pour l'océanographie côtière (par le CTOH/LEGOS). En plus de ce traitement spéciale, l'autre spécificité de notre base de données satellitaires est qu'elle contient 6 traces au sol correspondant à 5 ans de données entrelacées TOPEX-Jason-1, apportant une amélioration très significative de l'échantillonnage spatiale de zones clés comme le détroit de Hainan. En revanche, l'ajout de ces données tend à réduire la précision de la mesure des marées semi-diurnes (en particulier l'amplitude de M2 et la phase de S2) en raison de la durée limitée d'échantillonnage. Néanmoins, pour le Golfe de Tonkin dominé par les marées diurnes, la combinaison de 16 ans de données primaires et de 5 ans de données entrelacées fournit la meilleure base de données disponible à ce jour.

Le processus de validation du modèle s'accompagne de multiples tests de sensibilité sur la friction de fond, bathymétrie, forçage tidal aux frontières, résolution, bi- ou tri-dimensionnalité. Tout d'abord, la comparaison entre modèle et observations montre de bons résultats à proximité des frontières ouvertes du domaine de calcul impliquant que le produit global de marée TPXO fournit un forçage adéquat pour notre modèle. Les erreurs augmentent de manière significative près de régions côtières peu profondes. Il y a deux raisons possibles à cela, les erreurs du modèle et celles des mesures. L'erreur du modèle

tend à augmenter en eau peu profonde où les incertitudes sur la bathymétrie et la rugosité du fond (lié entre autre au substrat benthique) ont un impact plus important car les courants et phénomènes nonlinéaires y sont plus forts. On montre qu'il est possible de réduire cette erreur par un choix de valeurs faibles pour les coefficients de frottement, ce qui semble cohérent avec le fait que le Golfe du Tonkin est assez largement composé de sédiments fins. En outre, le choix d'un profil logarithmique du coefficient de frottement paraît crucial dans les simulations tridimensionnelles car il permet la prise en compte de la résolution verticale variable du modèle entre zones profondes et peu profondes. Sans la formulation logarithmique, le modèle bidimensionnel donne des prévisions de marée plus précise que le modèle tridimensionnelle, offrant un exemple où l'ajout de complexité ne va pas forcément dans le sens de l'amélioration des résultats.

La deuxième source de divergence entre modèle et observations est la perte de la qualité des mesures satellitaires altimétriques près de la côte en raison de la contamination faite par la surface terrestre et de corrections géophysiques inexactes (corrections de marées et des phénomènes atmosphériques de haute fréquence particulièrement intenses en zone côtière). Même avec l'amélioration de la définition du masque de terre faite par le traitement côtier du CTOH, les données situées à moins de 10 km des côtes restent en principe peu valides. Une comparaison entre les données des satellites et des marégraphes aux points les plus proches permettent une appréciation de l'erreur de mesure. Les erreurs sur les marées semi-diurnes (M2 et S2) sont les plus fortes et du même ordre que les différences entre modèle et observations. Il est donc difficile ici de faire la part des erreurs dues aux différentes sources d'information.

La validation de notre modèle fournit le degré de confiance nécessaire pour procéder à l'analyse des caractéristiques de marées dans le Golfe du Tonkin. En premier lieu, nous avons utilisé le modèle pour explorer pour la première fois le spectre de résonance du golfe. Les incertitudes dans le processus d'amortissement peuvent altérer les résultats de notre analyse, ils sont néanmoins cohérents avec les modèles théoriques et les observations. Ils montrent trois modes de résonance compatibles avec le modèle idéalisé de la baie rectangulaire à pente constante, avec un pic de résonance à des périodes de 29 h, 12,5 h et 8 h. Le modèle de baie rectangulaire à profondeur constante utilisée précédemment dans plusieurs études du golfe est donc faux. Il place la période de O1 au pic de résonance du mode 0 et ne prédit aucune résonance semi-diurne. Nos résultats suggèrent au contraire que les marées semi-diurnes sont résonantes en mode 1, mais ces marées sont peu amples en mer de Chine et restent donc modérée dans le Golfe du Tonkin malgré leur résonance. Au contraire, les marées diurnes sont amples dans la mer de l'Est/la mer de Chine du Sud en raison d'un phénomène de résonance d'Helmholtz impliquant le Détroit de Luzon. Par ailleurs, l'amplitude de O1 est plus grande dans le golfe que celle de K1 à cause d'un plus grand effet de résonance (O1 est plus proche de la période du pic de résonance de 29 heures), même si son amplitude dans la mer de Chine est inférieure à K1.

L'étape suivante dans la caractérisation du phénomène de marée concerne les courants résiduels de marée. Le modèle indique que les forts courants résiduels sont localisés dans le détroit de Hainan (~ 20 cm/s circulant vers l'intérieur du golfe) et à l'ouest de l'île de Hainan (~ 8 cm/s). Le détroit de Hainan est une zone de convergence des flux d'énergie de marée qui laisse peu d'énergie entrer ou sortir du golfe. Néanmoins, c'est là que les courants résiduels sont les plus importants, avec des conséquences pour le transport des propriétés marines à l'intérieur du golfe. Le détroit de Hainan est aussi une région de forte dissipation de l'énergie, corolaire d'un fort effet de mélange des marées. Le long de la côte occidentale du golfe, les courants résiduels sont beaucoup plus faibles atteignant seulement 2 cm/s autour des promontoires. Ces courants sont peut être sous-estimés par la faible résolution de la morphologie littorale. Une fonction de courant résiduelle est aussi calculé qui révèle un mode de transport anticyclonique cohérent autour de l'île de Hainan avec un maximum au milieu du golfe. La dérive Lagrangienne de marée apparaît quant à elle qualitativement proche de la circulation eulérienne mais plus faible. Ce dernier point est expliqué par l'opposition du résiduel eulérien et de la dérive de Stokes, du à la rotation des ellipses de marée du Golfe du Tonkin dans le sens des aiguilles d'une montre.

Les marées résiduelles peuvent être localement fortes et agissent continuellement mais restent plus faibles en moyenne que les courants du vent, en particulier pendant la saison d'hiver (mousson d'hivers). Cela a des implications potentielles pour les propriétés de transport. En outre, le stress du vent a un impact plus important que prévu par les études précédentes sur le mélange vertical durant la saison chaude. Nous avons montré dans la dernière partie de cette étude que c'est la combinaison des vents et des marées qui peuvent expliquer la localisation des fronts saisonniers dans le golfe du Tonkin. Notre bilan de chaleur suggère que l'étude de l'écosystème de cette région doit donc inclure un ensemble réaliste de forçage. Le modèle que nous avons développé paraît adéquat pour de telles applications en biogéochimie et dynamique sédimentaire. Cependant, une suite à notre étude requière un raffinement de la résolution dans la zone littorale où les phénomènes de dépôt (par les rivières notamment), d'érosion et de transport peuvent prendre une importance considérable. En parallèle, des efforts doivent aussi être déployés pour une meilleure connaissance de la bathymétrie locale et de la diversité des types de sédiments benthiques, ainsi que de leur impact sur la dynamique de la couche limite de fond.

TÓM TẮT

Thủy triều vùng vịnh Bắc Bộ

Vịnh Bắc Bộ, nằm trong khu vực biển Đông Việt Nam là một khu vực có ý nghĩa lớn về sinh thái, kinh tế và du lịch. Hiểu rõ hơn về quá trình vận chuyển trầm tích có ý nghĩa quan trọng cho sự phát triển bền vững của khu vực này. Mục tiêu nghiên cứu của luận án là xem xét các quá trình vật lý đặc trưng chi phối chế độ động lực của thủy triều ở Vịnh Bắc Bộ thông qua việc sử dụng mô hình số có độ phân giải cao, kết hợp với các số liệu sẵn có. Đặc biệt chú trọng kiểm tra chéo giữa mô hình, số liệu từ các trạm đo ven bờ và số liệu đo đạc vệ tinh, hiệu chuẩn mô hình được thiết lập từ một tập hợp các thí nghiệm với các thông số của mô hình. Cân bằng năng lượng triều trong vịnh được tính toán và phân tích; Đặc điểm của quá trình cộng hưởng được đánh giá, so sánh với kết quả của mô hình lý tưởng. Dòng triều dư tiếp cận theo phương pháp Euler và Lagrange được tính toán và ảnh hưởng của nó tới quá trình xáo trộn được làm rõ.

ABSTRACT

The Gulf of Tonkin, situated in the Vietnam East Sea/South China Sea, is a zone of strong ecological, touristic and economic interest. Improving our knowledge of its hydro-sedimentary processes (transport of suspended particles) is of great importance. The scientific objective of this study is to revisit the dominant physical processes that characterize tidal dynamics in the Gulf of Tonkin using a high-resolution model and the combination of all available data. Particular attention is thus given to model-data cross-examination using tidal gauges and coastal satellite altimetry data and to model calibration derived from a set of sensitivity experiments to model parameters. The tidal energy budget of the gulf (energy flux and dissipation) is then analyzed and its resonance properties are evaluated and compared with idealized models and observations. Then, the tidal residual flow in both Eulerian and Lagrangian frameworks is evaluated. Finally, the problem of tidal frontogenesis is addressed showing that tidal mixing alone does not explain the observed summer frontal structures in chlorophyll concentrations.